Real data calibration and floating potential model in the context of electroporation

Sergio Corridore

université de BORDEAUX

THESIS PRESENTED
TO OBTAIN THE QUALIFICATION OF

DOCTOR OF

THE UNIVERSITY OF BORDEAUX

Doctoral school of Mathematics and Computer Science
Specialization : Applied mathematics and scientific calculation

Sergio Corridore

Real data calibration and floating potential model in the context of electroporation

Under the supervision of Annabelle Collin and Clair Poignard
Defended on 21 September 2020

Members of the examination panel

M. Laurent Boudin	Maître de conférences HDR, Sorbonne Université	Rapporteur
Mme. Marie Robin	Maître de conférences HDR, Université Lyon 1	Rapporteuse
M. Lluis M. Mir	Directeur de recherche, CNRS	Président du jury
M. Olivier Saut	Directeur de recherche, CNRS	Examinateur
Mme. Annabelle Collin	Maître de conférences, Bordeaux INP	Directrice de thèse
M. Clair Poignard	Directeur de recherche, Inria	Directeur de thèse
M. Damien Voyer	Enseignant Chercheur, EIGSI La Rochelle	Invité

Abstract

Electroporation is a complex phenomenon that occurs when biological tissues are subjected to short electric pulses of high intensity. It makes it possible to either kill directly the cells in the target region (as for example a tumor) or to introduce molecules into living cells. Even though the phenomenon has been discovered for several decades, it is still incompletely understood. Several bioelectrical engineering strategies have been developed to improve the knowledge of the membrane response to electric stimulation by bioimpedance measurements. Bioimpedance measurements are a powerful tool from electrical engineering to track the electrical properties changes in biological tissues and cells. However the quantification of such impedance changes in terms of dielectric and conductive properties of the biological is far from trivial. This is due the addition of complex bioelectrical phenomena such as the electrode polarization, system calibration, and in addition the lack of accurate electrical model of biological samples. The aim of this thesis consists in proposing a modeling of the bioimpedance measures in a 4-electrode system, in the context of electroporation. On the one hand, the work consists in deriving an effective electrical circuit of the biological and to fit its parameters thanks to the 4-electrode system. The fitting is far from trivial since the "measured data" have been already pre-filtered using 3 reference measures, but due to the complexity of the experimental set-up and the complexity of biological electrical properties the calibration leads to large error. To overcome this issue, a new calibration is proposed to minimize the error on the filtered data. Then, advanced calibration procedure is proposed to investigate the impact of electroporation on the effective conductance and capacitance of cell membranes. On the other, we investigate the asymptotic analysis problem of floating potential. Indeed, it is well-known in quasi-electrostatics that highly conductive materials behave like an equipotential and a nonlocal boundary condition is imposed, so-called floating potential. This floating potential problem consists in solving Poisson equation with a constant Dirichlet boundary condition, which is implicitly fixed by the constraint that the total current on the boundary vanishes, yielding a non local constraint. Thanks to an asymptotic analysis, the accuracy of such floating potential is derived, and an improvement is proposed to account for the geometry of the needles. This is particularly crucial in electroporation, when high amplitude electric fields are applied. Finally, we validate this model by comparing the bioimpedances obtained with the PDE simulations with the measured bioimpedances.

Keywords: Asymptotic Analysis ; Elliptic problem ; Numerical Calibration Strategy ; Bioimpedance ; Electroporation

Résumé

L'électroporation est un phénomène complexe qui se produit lorsque des tissus biologiques sont soumis à de courtes impulsions électriques de grande intensité. L'électroporation permet de tuer les cellules d'une tumeur ou d'introduire des molécules dans les cellules en augmentant la perméabilité de leurs membranes. Même si le phénomène a été découvert il y a plusieurs décennies, de nombreuses questions persistent. Plusieurs stratégies d'ingénierie bioélectrique ont été développées pour améliorer la connaissance de la réponse membranaire à la stimulation électrique par des mesures de bioimpédance. Les mesures de bioimpédance sont un outil puissant pour suivre les changements des propriétés électriques dans les tissus et dans les cellules biologiques. Cependant, la quantification de ces changements d'impédance en termes de propriétés diélectriques et conductrices est loin d'être triviale. En effet les phénomènes bioélectriques complexes tels que la polarisation des électrodes, l'étalonnage du système ainsi que l'absence de modèle électrique précis compliquent la procédure. L'objectif de cette thèse est de proposer une modélisation des mesures de bioimpédance dans un système à 4 électrodes, dans le cadre de l'électroporation. Dans une première partie, le travail consiste à dériver un circuit électrique modélisant l'impédance du système et à adapter ses paramètres grâce aux données d'impédance issues des mesures. L'ajustement est loin d'être facile puisque les " données mesurées " ont déjà été pré-traitées par une étape d'étalonnage qui en raison de la complexité de la configuration expérimentale et des propriétés électriques biologiques, conduit à une erreur importante. Pour surmonter ce problème, une nouvelle stratégie d'étalonnage est proposée permettant de minimiser l'erreur sur les données calibrées. Ensuite, une procédure d'estimation paramétrique du circuit électrique est proposée afin d'étudier l'impact de l'électroporation sur la conductance et la capacité effectives des membranes cellulaires. Dans une deuxième partie, nous proposons une analyse asymptotique du potentiel flottant. En effet, il est bien connu en électro-quasi statique que les matériaux hautement conducteurs se comportent comme une équipotentielle et qu'une condition aux limites non locale – appelée potentiel flottant – est imposée. Ce problème de potentiel flottant consiste à résoudre l'équation de Poisson avec une condition aux limites de Dirichlet constante. Cette condition de Dirichlet qui est une inconnue du système va être fixée par la contrainte que le courant total sur la frontière s'annule c'est-à-dire qu'aucun courant ne sort du domaine. Grâce à une analyse asymptotique, un potentiel flottant est obtenue, et nous proposons une amélioration permettant de prendre en compte la géométrie des électrodes. C'est une étape cruciale pour l'application en électroporation puisque des champs électriques de grande intensité sont appliqués. Ce modèle est finalement validé par une comparaison entre les bioimpédances obtenues avec les simulations du potentiel flottant et les bioimpédances calibrées issues des mesures.

Mots-clés : Analyse asymptotique ; problèmes elliptiques ; stratégie de calibration numérique ; Bioimpédance ; Électroporation

Résumé long (en français)

fL'électroporation est un phénomène complexe qui se produit lorsque les tissus biologiques sont soumis à de courtes impulsions électriques de grande intensité. Elle permet soit de tuer directement les cellules de la région cible (comme par exemple une tumeur), soit d'introduire des molécules dans des cellules vivantes. Même si le phénomène d'électroporation a été découvert il y a plusieurs décennies, il n'est pas encore complètement compris. Cette thèse contribue à l'amélioration de la connaissance de ce phénomène dans le domaine des mathématiques appliquées en proposant la modélisation d'un montage expérimental bioélectrique permettant de le quantifier.

Même si l'électroporation est de plus en plus utilisée, plusieurs aspects du phénomène restent inexpliqués, comme par exemple les modifications structurelles effectives de la membrane. D'autres nécessitent des études complémentaires, comme la corrélation entre la configuration du traitement d'électroporation (intensité du champ électrique, durée et nombre d'impulsions, durée entre les pulses etc ...) et ses effets (taux de perméabilisation, extension de perméabilisation, quantité de cellules survivantes, seuil entre électroporation réversible et irréversible). L'électroporation est un sujet de recherche actif en raison de la pertinence de ses applications. Cette communauté comprend des biologistes, des médecins, des ingénieurs électriciens, des médecins et des mathématiciens.

Le rôle du mathématicien est de développer des modèles mathématiques capables de décrire le processus d'électroporation avec simplicité et efficacité. Les simulations - nécessitant un temps et un coût financier relativement bas - obtenues grâce aux connaissances mathématiques, biologiques et physiques sont un support solide pour les expériences *in-vivo* ou *in-vitro*. Dans [19] par exemple, les auteurs modélisent la diffusion du champ électrique pendant l'ablation par électroporation irréversible, dans [48], les auteurs ont travaillé sur la dynamique moléculaire et dans [29] sur les capacités conductrices de la membrane.

Les mesures expérimentales obtenues avec la nouvelle configuration à 4 électrodes proposée par Garcia-Sanchez *et al.* [20] pour étudier la réponse électrique de la membrane cellulaire à une stimulation électrique élevée sont le fil conducteur de la thèse.

Relier ces mesures d'impédance à un circuit électrique équivalent de type $R|C$ (résistance / capacitance) est loin d'être simple car l'appareil de mesure a besoin d'être étalonné, pour prendre en compte la distorsion des données due à la configuration. La première partie de la thèse consiste donc à proposer une nouvelle stratégie d'étalonnage des données d'impédance puis à proposer un circuit électrique bien conçu modélisant l'expérience à 4 électrodes. L'estimation des pa-

ramètres de ce circuit à l'aide des mesures d'impédance permet de comprendre l'impact de l'électroporation sur la mono-couche cellulaire.

La particularité de la configuration à 4 électrodes est d'utiliser 2 électrodes dites actives pour imposer le courant et 2 électrodes dites passives pour mesurer la réponse électrique du système. Cela complexifie considérablement le modèle mathématique, car au lieu de l'utilisation standard d'opérateurs "Dirichlet-to-Neumann" comme en tomographie (où la tension est imposée à l'électrode et le courant est mesuré sur la même électrode), il faut prendre en compte l'impact des électrodes passives sur le courant appliqué ce qui conduit à un problème de potentiel dit flottant. De plus, l'épaisseur de l'eau interfaciale - qui a des propriétés électriques particulières - est directement liée à la tension des électrodes. L'épaisseur des électrodes est donc beaucoup plus petite que dans la configuration standard à 2 électrodes ce qui permet au dispositif à 4 électrodes de limiter l'influence de l'eau liée au voisinage des mesures d'électrodes. La deuxième partie de la thèse est donc consacrée à l'analyse d'une équation aux dérivées partielles elliptique décrivant l'approximation électro-quasi statique du potentiel électrique dans la configuration à 4 électrodes. La principale difficulté - qui est un problème courant avec les mesures d'impédance - est due à la présence de ces électrodes inactives très conductrices et minces. La manière classique de modéliser ces électrodes inactives consiste à utiliser une approche de pénalisation mais cela conduit à des instabilités numériques. Nous proposons dans cette thèse une analyse asymptotique pour réduire le modèle, ce qui conduit également à une stratégie plus précise et plus robuste appelée potentiel flottant. Enfin, nous utilisons l'approche potentiel flottant pour approximer le potentiel électrique avec la configuration à 4 électrodes pour l'électroporation d'une mono-couche cellulaire. Nous comparons les impédances simulées avec les impédances mesurées et nous obtenons des résultats très satisfaisants.

Les principales contributions de cette thèse sont résumées dans les points suivants.

• Une nouvelle stratégie d'étalonnage pour le dispositif à 4 électrodes de [20] a été proposée.

• Un circuit électrique bien pensé a été conçu et ses paramètres ont été estimés à l'aide des données d'impédance calibrées pour l'électroporation d'une mono-couche cellulaire.

• Une analyse asymptotique du problème de conductivité avec des électrodes passives minces à haute conductivité a été faite.

• Une validation du modèle elliptique avec potentiel flottant pour la configuration à 4 électrodes a été mise en place.

Nous proposons à présent un résumé des apports de cette thèse par chapitre.

Chapitre 1 Ce chapitre se concentre sur la reproduction et l'interprétation de l'ensemble des données dérivant d'une expérience d'électroporation. Les observations sont les mesures de l'impédance de l'électroporation d'une mono-couche cellulaire effectuées avec une configuration arrangée à 4 électrodes. Le but est l'analyse du comportement électrique de la cellule avant et après une impulsion électrique visant à l'électroporation. Ce travail a représenté une tâche difficile du début - à

savoir l'organisation des données - à la fin - à savoir formaliser le modèle et estimer ses paramètres ainsi qu'interpréter leurs évolutions. Pour bien comprendre les données, il a été fondamental de comprendre le processus d'extraction de ces dernières et le contexte des expériences. Pour cette raison, le chapitre commence par l'introduction de l'approximation électro-quasi statique et la définition de la notion de circuit équivalent illustrées sur un système électrique simple. L'idée est de fournir toutes les notions nécessaires à la compréhension du sujet abordé. Il a été nécessaire de comprendre en profondeur le système de mesure à 4 électrodes et la méthode d'étalonnage à trois références, utilisées respectivement pour mesurer l'impédance cellulaire et pour éliminer la distorsion du système de mesure. Grâce aux connaissances acquises, nous avons mis en avant la faiblesse de la stratégie d'étalonnage utilisée et nous avons proposé une nouvelle stratégie plus robuste qui se base sur l'utilisation de plus de mesures de référence que l'étalonnage habituel à 3 références. L'efficacité de la nouvelle stratégie est prouvée par la comparaison avec le comportement théorique attendu pour les observations, donnée par :

$$Z^{(c)}_{FC,\,t}(\omega) = \frac{k}{\sigma_{(c)} + i\omega\epsilon_{(c)}}$$

Un modèle de type circuit électrique a ensuite été proposé dans le but de l'ajuster au jeu de données étalonnées. Le choix de ce circuit découle de notre compréhension du système d'expérience. Une fois les deux éléments composant le système (cellules et tampon) identifiés, l'analyse de leurs propriétés physiques conduit à définir le modèle, représenté sur la figure R-1 et donné par les équations (R-1) et (R-2). La

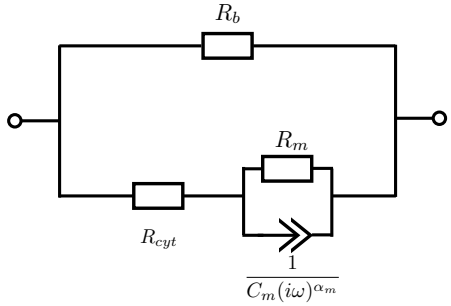

$$Z_{eq}(\omega,\theta) = \frac{R_b\, Z_{cells}(\omega,\theta)}{R_b + Z_{cells}(\omega,\theta)}, \qquad \text{(R-1)}$$

$$Z_{cells}(\omega,\theta) = R_{cyt} + \frac{R_m}{1 + R_m C_m (i\omega)^{\alpha_m}}. \qquad \text{(R-2)}$$

Figure R-1 – Circuit électrique pour le système cellules-tampon

dernière difficulté recontrée dans ce chapitre concerne la non-identifiabilité du circuit électrique modélisant le système. Nous avons résolu ce problème en supposant que le comportement électrique de la membrane cellulaire n'est pas affecté par la conductivité du tampon. Ainsi, une définition fiable des intervalles des paramètres a permis leur estimation de manière robuste. Les estimations ont été faite avec un estimateur de moindres carrés disponible sous Matlab. Le code mis en place est suffisamment général pour permettre de paramétrer d'autres circuits électriques sur d'autres données d'impédance. L'estimation des paramètres avant et après le pulse électroporant donne des résultats très intéressants car ils permettent de comprendre l'impact du phénomène d'électroporation. En particulier, les paramètres représentant la résistance du tampon R_b et la résistance membranaire R_m diminuent dans

les minutes qui suivent l'impulsion. Ces évolutions suggèrent une augmentation inhabituelle des échanges de cellules avec le tampon. Cette observation signifie que l'impulsion appliquée entraîne l'électroporation de la mono-couche cellulaire.

Chapitre 2 Ce chapitre concerne la modélisation de la présence d'électrodes passives fines et fortement conductrices dans l'expérience présentée au chapitre précédent. En considérant un domaine plus simple représentant la zone de contact entre l'électrode et le tampon, nous avons modélisé ce système grâce à un problème de potentiel flottant (FP). L'idée est de considérer l'électrode comme une surface équipotentielle et son potentiel comme une inconnue du problème. Nous avons prouvé l'existence et l'unicité de la solution du problème du potentiel flottant. Cette méthode a été comparée à une approche de pénalisation classique, qui s'est avérée générer de nombreuses instabilités. Nous proposons aussi une analyse asymptotique qui permet à la fois de donner une estimation de l'erreur d'approximation entre pénalisation et FP et de proposer une amélioration de la condition de potential flottant. Nous avons observé que l'approche par pénalisation nécessite un maillage

Problème avec pénalisation	**Potentiel flottant**	**Convergence**
$\begin{cases} -\nabla\cdot(\sigma^\varepsilon\nabla u_\varepsilon) = f \quad \text{in} \quad \Omega_i\cup\Omega_e, \\ u_{\varepsilon\vert\Gamma_0{}^I} = u_{\varepsilon\vert\Gamma_0{}^e}, \\ \sigma_i\,\partial_n u_{\varepsilon\vert\Gamma_0{}^I} = \varepsilon^{-k}\sigma_e\,\partial_n u_{\varepsilon\vert\Gamma_0{}^e}, \\ \partial_n u_{\varepsilon\vert\Gamma_{ext}} = 0, \\ u_{\varepsilon\vert\Gamma_{int}} = \gamma, \end{cases}$	$\begin{cases} -\nabla\cdot(\sigma_i\nabla u_0) = f \quad \text{in } \Omega_i, \\ u_{0\vert\Gamma_0} = \alpha_0, \\ \int_{\Gamma_0}\sigma_i\partial_n u_0\,ds = 0, \\ u_{0\vert\Gamma_{int}} = \gamma. \end{cases}$	$\|u_\varepsilon - u_0\|_{H^1(\Omega_i)} \le c\,\varepsilon$

excessivement raffiné ce qui conduit à un coût de calcul élevé. De plus, le fait de devoir utiliser des très petits pas en espace provoque des instabilités numériques lors de la résolution. Une faiblesse de l'approche potentiel flottant est la résolution d'un nombre plus élevé de problèmes. Néanmoins, tous ces problèmes sont des problèmes de Dirichlet avec la même matrice apparaissant dans le système linéaire, il est alors possible de la factoriser (si on utilise un solveur linéaire) une seule fois et de résoudre les systèmes en parallèle. De plus, le problème du potentiel flottant ne contient pas de domaine mince et peut être résolu sur un maillage plus grossier. Ce qui implique que la méthode basée sur le potentiel flottant est peu coûteuse en temps de calcul et plus stable. La figure R-2 compare la robustesse des deux approches. Les deux approches (pénalisation et FP) ont été résolus numériquement grâce à l'implémentation d'une librairie de différences finies en C++ (environ 3200 lignes) sur une grille cartésienne 2D.

Chapitre 3 Le dernier chapitre établit une connexion entre les résultats du chapitre 1 et ceux du chapitre 2. L'approche du potentiel flottant développée au chapitre 2 a été appliquée pour obtenir une représentation d'une coupe 2D du système à 4 électrodes présentée dans le chapitre 1. Le défi est de formaliser le problème du potentiel flottant avec six électrodes (4 passives et 2 actives). Une condition de

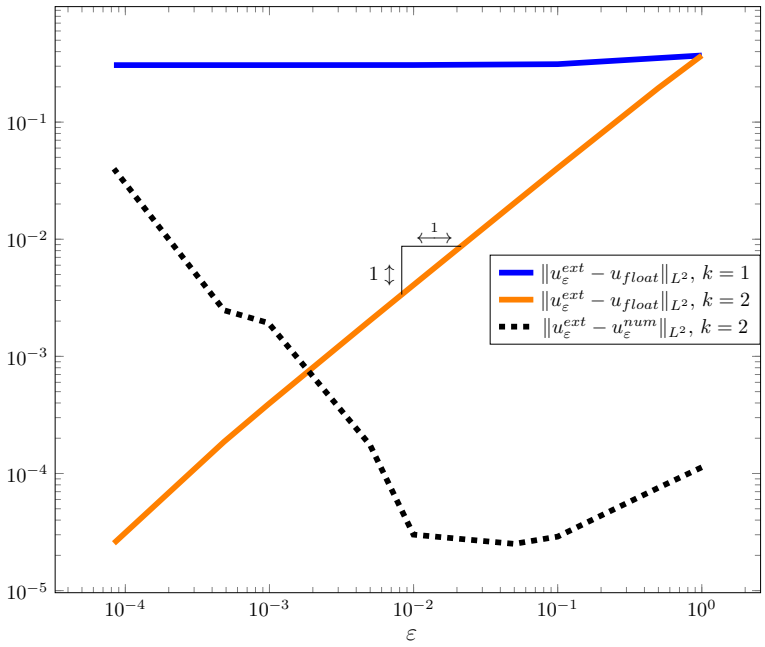

FIGURE R-2 – $k = 1$: lorsque ε tend vers zéro, la solution exacte ne converge pas vers la solution approchée par le *potentiel flottant*. $k = 2$: lorsque ε tend vers zéro, la solution exacte converge vers la solution approchée par le *potentiel flottant*. En raison d'un *conditionnement* élevé de la matrice, la différence entre la solution approchée par la méthode de pénalisation et la solution exacte ne converge pas vers 0 pour des valeurs petites de ε.

Gauge doit être imposée pour avoir l'unicité de la solution. Nous supposons donc que $\int_{E_1} u\,dx = 0$ (ce qui est revient à imposer : $u_{|_{E_1}} = \alpha_1 = 0$). Le problème s'écrit alors : trouver $(u, \alpha_2, \alpha_3, \alpha_4) \in H^1(\Omega) \times \mathbb{R}^3$ vérifiant

$$\begin{cases} \nabla \cdot (\sigma \nabla u) = 0, \quad \text{in } \Omega, \\ \sigma \partial_{n\varepsilon_1} u_{|\varepsilon_1} = g, \qquad \sigma \partial_{n\varepsilon_2} u_{|\varepsilon_2} = -g, \qquad u_{|_{E_1}} = 0, \\ u_{|_{E_j}} = \alpha_j, \quad j = 2, 3, 4, \; u_{|_{E_1}} = 0 \\ \displaystyle\int_{E_j} \sigma \partial_{n_{E_j}} u\, ds = 0, \quad j = 2, 3, 4, \\ u_{|_{L_1}} = u_{|_{L_2}}, \\ \sigma \partial_n u = 0 \quad \text{ailleurs.} \end{cases} \tag{R-3}$$

L'existence et l'unicité de la solution de ce problème ont été prouvées. La résolution numérique – présentant tous les avantages de l'approche par potentiel flottant – donne une solution numérique réaliste du potentiel dans le domaine. Comme dans le chapitre 2, le problème a été résolu numériquement grâce à une librairie de différences finies en C++ (environ 3200 lignes) sur une grille cartésienne 2D. À partir de la solution numérique, nous avons calculé l'impédance mesurée numérique Z_m^{num} comme le rapport entre le courant imposé par les électrodes actives et la tension mesurée par les électrodes passives :

$$Z_m^{num} = \frac{\alpha_2 - \alpha_1}{C_a},$$

σ (S·m^{-1})	Z_s^{num} (ohm)	$\lvert Z_{FC,cal}(\omega_1)\rvert$ (ohm)	Err (%)
0.098	610	593	2.8
0.265	204	219	7.3
0.57	114	102	10.5
0.965	62	60	3.2
1.432	40	41	2.5

Table R-1 – Comparaison entre les impédances Z_s^{num} obtenues avec les simulations et les impédances mesurées avec l'expérience à 4 électrodes $|Z_{FC,s}(\omega_1)|$ pour plusieurs conductivités.

et l'impédance numérique Z_s^{num} par

$$Z_s^{num} = \frac{\dfrac{1}{|S_2|}\displaystyle\int_{S_2} u dS - \dfrac{1}{|S_1|}\int_{S_1} u dS}{\displaystyle\int_{S_1} \sigma \partial_n u dS},$$

où les surfaces S_1 et S_2 sont parallèles aux côtés verticaux de Ω et placées entre les électrodes passives. La comparaison avec les données d'impédance issues de l'expérience 4 électrodes – voir par exemple le Tableau R-1 pour les impédances calibrées – nous permet de valider :

- le modèle de potentiel flottant pour le système de mesure à 4 électrodes sans cellules,
- l'estimation des conductivités et de la longueur des électrodes,
- la stratégie d'étalonnage des impédances mesurées obtenues par le système de mesure à 4 électrodes.

Ces résultats sont très encourageants et mettent en avant l'apport des mathématiques appliquées dans la compréhension du phénomène d'électroporation.

A Marta e Zaira,
il più determinato e amorevole sostegno.
A loro tutti i successi della mia carriera universitaria.

Acknowledgements

"Dimmi chi ringrazi e ti dirò chi sei." [Detto sconosciuto].

Le travail qui sera présenté dans ce manuscrit n'est pas l'œuvre d'une seule personne, et beaucoup de crédits reviennent à tous ceux qui m'ont entouré professionnellement et personnellement.

En premier, je veux remercier mes directeurs de thèse Annabelle et Clair. Merci à Annabelle pour m'avoir accueilli dans l'équipe lors de mon stage de Master 2. La haute qualité du travail que nous avons accompli ensemble, dans un milieu très agréable, m'a motivé pour me lancer dans le parcours de la thèse qui m'a permis de connaître Clair professionnellement. Merci à vous de m'avoir accompagné pendant les travaux de thèse et de votre soutien également pendant des moments difficiles comme celui du confinement. J'admire la qualité de votre recherche et vos compétences comme scientifiques qui m'ont permis d'apprendre énormément.

Merci à Laurent Boudin et Marie Robin pour avoir accepté de lire mon manuscrit de thèse et pour les rapports encourageants qui ont suivis : vos remarques et vos réflexions m'ont donné la juste motivation pour la soutenance.

Merci à Lluis Mir pour avoir accepté de participer à mon jury de thèse et de le présider ainsi que pour la collaboration pendant les années du doctorat. Chaque réunion c'était un plaisant moment de fructueuse découverte. Pour la même raison je tiens à remercier le personnel de l'Institut de cancérologie Gustave Roussy avec qui j'ai collaboré, en particulier à Tomás García-Sánchez. Ton travail a été fondamental pour le développement de mon sujet de thèse et j'aurai toujours un bon souvenir des nos rencontres.

Également, je tiens à remercier Olivier Saut, pas seulement pour avoir accepté de faire partie de mon jury de thèse, mais aussi pour son rôle de chef d'équipe et de co-encadrant de mon stage lors de mon arrivée dans l'équipe. Je le remercie aussi pour m'avoir saisi comme voisin de bureau et pour ne pas m'avoir confiné dans une salle perdue et silencieuse de l'IMB.

Je souhaite à présent remercier Damien Voyer pour avoir participé à la soutenance mais aussi pour sa collaboration et ses contributions fondamentales pour mon travail.

Merci aussi à Magali Ribot et Marie-Pierre Rols, membres de mon comité de suivi, pour leur suivi et pour leurs conseils qui m'ont accompagné pendant les quatre ans de thèse.

Je tiens exprimer ma reconnaissance aussi à notre assistante d'équipe Sylvie Embolla, au personnel administratif de l'IMB ainsi que celui de la cellule informatique car l'efficacité de leur travail a constitué un important soutien mais c'est aussi leur gentillesse qui a rendu tout plus facile.

Maintenant je vais passer aux remerciements pour tous ceux-celles qui n'ont pas contribué directement à la thèse mais que grâce à leur présence ils-elles ont fait de ces dernières années un parcours inoubliable.

Merci à Mon-Phis (MONC MEMPHIS). J'ai vu passer une centaine de personne par ces deux équipes et je n'ai pas la place pour les remercier tous individuellement. Je laisse mon rôle de "ancien" du groupe à Cedricco et Antoine, deux anciens pour de vrai. Je tiens à souligner combien j'étais heureux de tomber dans cette famille avec qui j'ai partagé plein de bons moments, tous les repas, les pauses café et aussi pas mal de soirées. C'est une famille dans laquelle tu peux toujours trouver quelqu'un/e avec qui te confronter, te conseiller et rigoler. Je remercie le Mon-Phis pour tous les amis qui m'a donné. En particulier je veux remercier les deux personnes avec qui j'ai partagé plus de temps : mes co-bureau Cynthia et Olivier Gallinato. Merci Cynthia pour tous les sourires, l'aide et les bons moments passés ensemble. Merci également à Olivier pour tous les conseils que tu m'a donné pendant le doctorat et pour avoir été un peu mon "tutor" mais aussi pour tous les moments d'amitié hors du boulot.

Je remercie également la communauté des doctorants de l'IMB ansi que l'association LAMBDA. J'ai eu un exemple de comment la recherche doit fonctionner : partager des intérêts scientifiques ainsi que des moments de sincère amitié.

Je tiens remercier Adrien, Cristina, Hali, Robin et Silvia copains et copines essentiel(e)s, toujours prêt(e)s à donner un conseil devant une bière ou une clope.

In questa lista bisogna inserire anche i miei colleghi e friends dell'UniCT, Altea, Antonio, Eugenia, Giorgio e Valentina. È bello avervi vicino dopo tutti questi anni. Ringrazio in particolare Antonio e Giorgio perché "È con gli amici che si può essere autenticamente scemi al 100%".

Je tiens remercier mes premiers colocs Julien et Gabriele parce que grâce à eux, pour la premier fois, je me suis senti chez moi dans un endroit si loin de ma Sicile. Merci à Julien pour m'avoir offert son gentil sourire et pour m'avoir fait découvrir qu'aussi un physicien peut être drôle. Grazie a Biri, amico e fratello maggiore, che mi ha rivelato tante verità in cucina come nella vita di tutti i giorni.
Merci également aux colocs de la rue du Scandale, Cécile et Clément. C'est melange des mecs du Sud et da la fille du (Nord)Est a été parfait. Merci à vous pour être des amis sincères et authentiques qui ont cette folie synonyme de bonheur.

Grazie Vas, mio amico fratello, compagno di viaggio e di avventura. Grazie per questi anni di dottorato insieme. Spero tu sappia quanto mi senta in sintonia con te, colgo questa occasione per ricordarlo.

Un altro amico di avventura che devo ringraziare è Pippo. Grazie per tutte le risate che ci siamo fatti insieme, grazie per i momenti di sincera e schietta amicizia. Ma sopratutto grazie per ogni serata al Circle !

Voglio ringraziare Athina, che è stata fin dal primo momento un'amica e molto di più dopo. Anche in seguito con la distanza, ha rappresentato un importante stostegno nei momenti grigi e mi ha sempre spinto a dare il meglio. La voglio ringraziare per la calma e la serinità che mi trasmette ma anche per il suo sorriso, che mi ricorda ciò che c'è di più bello nella vita di tutti i giorni.

Naturalmente un grande ringraziamento va alla mia famiglia. A Bruno che mi ha trasmesso la passione per la matematica e per le altre scienze. A mia madre che mi ha sempre spronato a dare il meglio nei miei studi. A mia sorella Roberta perché è la persone su cui posso contare di più, da sempre.

Voglio concludere questi ringraziamenti con un testo che viene da un libro che ho letto non molto tempo fa :

[...]*Alla fine entrò in una piccola porta della rue Sainte Catherine. Salì tre piani e trovo una casa molto carina, senza soffitto, senza cucina. Dentro c'era un variegato gruppo di gente strana. C'era una coppia di ragazzi del sud, di una piccola città della Sicilia. Gli offrirono una palla di riso fritta. Lui non capì bene il nome di quella specialità ma li ringraziò perché loro rappresentavano per lui una famiglia con cui condividere pranzi, cene e tanti momenti spensierati. C'era una ragazza di Bergamo, un po' una sorella maggiore, che gli disse che "la vita l'è bela, l'è bela!". Lui le fu grato perché lei gliel'ho ricordò sempre, anche quando non sembrava esserlo. C'era una ragazza di Lione. Lei gli insegnò a suonare una musica felice anche quando fuori era buio. La ringraziò per la forza donata da quella musica che gli ricordava un abbraccio caldo. La proprietaria di casa era una ragazza di Parigi. Lei gli offri quella casa che, nonostante le apparenze, l'aveva resa la più calda e accogliente della città. Le fu grato perché, fra mille, fu lei a trovare lui. Era presente un tipo di Milano. Lui cantò una canzone. Era semplice e vera. Gli fece osservare che la vita può essere un po' come quella canzone, semplice e vera, se sai guardarla dalla giusta prospettiva. E infine un ragazzo di Roma. Lui era quello fra tutti che non faceva mai niente. Gli diede solo un'amicizia e gli disse che era suo fratello. Lo ringraziò per questo.*

Contents

List of Figures

List of Tables

Abbreviations

CPA constant phase angle
EC equivalent circuit
ECT electrochemotherapy
EIS Electrical Impedance Spectroscopy
EP electrode polarization
FDM Finite Difference Method
FEM Finite Element Method
FP floating potential
IRE irreversible electroporation
LCE low-conductivity electroporation
RE reversible electroporation

Introduction

Electroporation is a complex phenomenon that occurs when biological tissues are subjected to short electric pulses of high intensity. It makes it possible to either kill directly the cells in the target region (as for example a tumor) or to introduce molecules into living cells. Even though the phenomenon has been discovered for several decades, it is still incompletely understood. Several bioelectrical engineering strategies have been developed to improve the knowledge of the membrane response to electric stimulation by bioimpedance measurements. This thesis brings a few applied mathematics contributions to the modeling of a recent bioelectrical experimental setup in the context of electroporation.

Context of the PhD: Cell membrane and pulsed electric field

In this section, we present the main steps in the electroporation phenomenon, which is a phenomenon that occurs at the cell membrane level.

The structure of a cell membrane: a brief overview

The cell (from Latin *cella*, small room) is the basic biological unit of all known living organisms. The cell contains a complex machinery of biomolecules, such as proteins, dissolved in the cytoplasm, nucleic acids, and several inorganic molecules dissolved in the cytoplasm, which is enclosed within the cell membrane. The cell membrane is composed of phospholipids, protein, and several lipids (such as cholesterol), and it is ~ 5 nm thick. The phospholipids are structurally the essential elements that compose the membrane, being the amphiphilic elements of the membrane. Those molecules are provided with a hydrophilic head and a lipophilic tail that allow the typical disposition tail-tail of the phospholipids in the cell membrane, as shown in Figure I-1.
The cell membrane is not a static structure. It has been now well established that the cell membrane behaves as a fluid mosaic [46], meaning that all the phospholipids shift alongside the same layer, as Figure I-2a depicts. The trans-bilayer motion of a phospholipid which passes from one layer through the membrane and accommodates on the opposite layer is named flip-flop movement [14] and is represented in Figure I-2b.
The lipidic structure of a cell membrane is variegated, and three main lipidic molecules are involved in the structuration of the cell membrane: glycerophospholipids, sphingolipids, and sterols [23]. The membrane proteins can be mainly

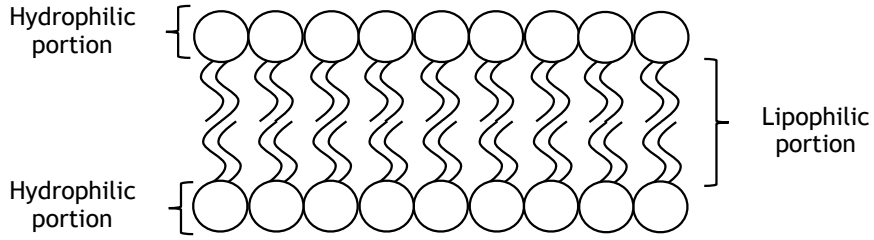

Figure I-1 – Phospholipid organization in a bilayer: the lipophilic tails are organized in the center of the membrane, and through weak bonds stick together, while the hydrophilic heads are in contact with the cytoplasm and the extracellular fluids respectively.

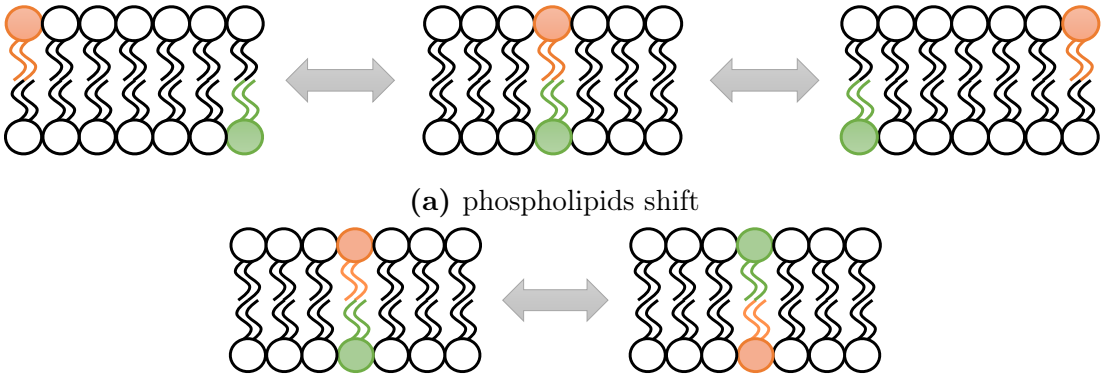

(a) phospholipids shift

(b) *flip-flop*

Figure I-2 – Phospholipids movement can occur by shifting (Figure I-2a) or by exchange of two phospholipids of two different layers, the so-called *flip-flop* ((Figure I-2b).

classified in intrinsic and extrinsic. The intrinsic or transmembrane proteins are structures that cross the whole bilayer, while the extrinsic proteins allow the passage between the cytoplasm and the extracellular domain. Extrinsic proteins, that are located in the inner or outer surface of the membrane, are proteins that enable the recognition of the cell (e.g. antigens) in the outer face, or that allow metabolic processes (e.g. adenylyl cyclase) in the inner face of the bilayer [9].

Cell transports

Despite the essential role of the extrinsic and intrinsic proteins, several mechanisms have to be considered essential for the transportation of ions, the passage of small molecules, macromolecules, and proteins from the extracellular matrix to the cytoplasm and vice-versa, the nutrition and the general functional activity of the cell. The membrane is semipermeable, that means it allows the passage of only certain types of ions. So far, it has been discovered that the most common physiologic system of communication with the external environment can be passive or active.
The passive transport occurs without the energy expenditure but it ruled by the

presence of a concentration gradient. Following this concentration gradient, the molecules or the ions cross the membrane. The passive transport can occur directly through the phospholipidic bilayer, in the case for example of the simple diffusion, or through transmembrane proteins, such as the so-called aquaporis that enable the osmosis, or the so-called ion channels that lead the facilitate diffusion. In particular, ion channels lead the transportation of specific inorganic ions from the extracellular fluids to the cytoplasm and vice-versa (mainly Na^+, K^+, Ca^{2+}, and Cl^-) with any energy expenditure [2]. As consequence, a difference of potential is generated into the two sides of the membrane.

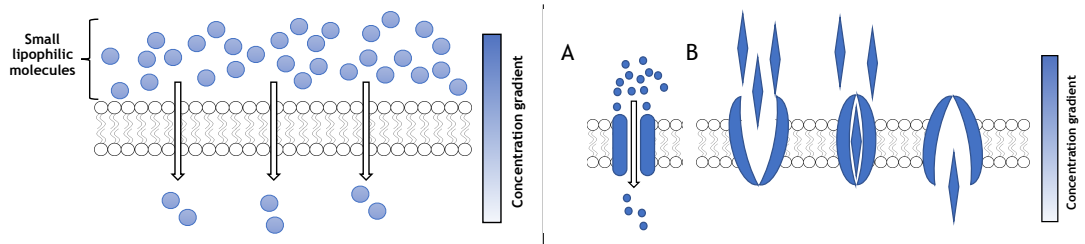

(a) Simple diffusion **(b)** Facilitated transport

Figure I-3 – Example of passive transport trough the cell membrane. Figure I-3a shows the simple diffusion. Figure I-3b depicts the facilitate transport: it allows the movement of molecules from the most to the least concentrated compartment through A) non saturable channels or B) saturable carriers.

Differently from the passive transport, in which the movement is in the direction of the concentration gradient, active transport uses cellular energy (such as ATP hydrolysis) to move molecules against the concentration gradient through specific transmembrane proteins [45].

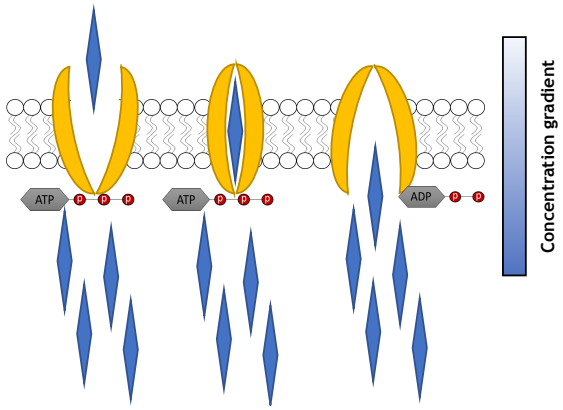

Figure I-4 – Active transport: a carrier, with the use of ATP hydrolysis, allows the movement of a molecule from the least concentrated compartment to the most concentrated one.

Membrane potential and the electric properties of the cell membrane

The membrane potential is the difference of electric potential between the cytoplasm and the extracellular matrix of a cell. A typical membrane potential of

a cell is calculated in mV and lays in the range of -40 to -80 mV, meaning that outside the cell, the fluids present a slightly higher concentration of positive ions, in comparison to the cytoplasm. The membrane itself can be considered as an insulator, allowing the passage of ions, thanks to the ion transporters and channels. Ion transporters force the passage of ions against the gradient, while the ion channels, as already said, allow the passage of the ions following the gradient of concentration. Membrane potential fulfills two main functions: firstly, it provides the power to perform several molecular functions (such as the ATP production within the mitochondrion), and secondly, a variation of the membrane potential allows the activation of several excitable cells, such as the neurons [2, 10, 39]. The polarization of a cell is made possible thanks to the contribution of several transporters and channels, such as the Na^+/K^+-pump, that actively bring within the cell two K^+ and transport outside the cell three Na^+ through an ATP activity [50], and the K^+ Leak Channel, that allows the entrance of K^+ in the cell. This latter is one of the most relevant components that maintain the membrane potential in live cells. When the Na^+/K^+-pump forces inside the cell the K^+ ions, a gradient of concentration is formed, and K^+ may diffuse again through the cell thanks to the K^+ Leak Channels. Furthermore, since the cytoplasm is more negative than the extracellular matrix, an electrical gradient takes place, a phenomenon that attracts back K^+ in the cell. When the equilibrium between the electrical and chemical gradients is reached, the resting potential of the cell is observable ($\sim -40/-80$ mV) [3, 31].

Electroporation

Electropermabilization or Electroporation is a biological response of the cell to the effect of an electric field that increases the membrane permeability, allowing the passage across the membrane to cells that would be blocked in standard conditions. This process lies in the cell membrane characteristics. The cell membrane, as aforementioned, is composed by a bilayer, whose has the main goal of forming a physical and electrical barrier towards the external fluids, maintaining an electric potential of $\sim -40/-80$ mV. When cell transmembrane potential reaches a threshold value (normally observed at 1 V), an electric breakdown of the cell membrane is generated. The lipids inside the membrane re-orient to form small openings, forming a pore, and allowing the water to pass, as depicted in Figure I-5 [44]. Moreover, it has been observed that the application of such a potential difference in the cell membrane increases its permeability sensibly [11, 24, 31].

Dependently from several factors, such as the intensity of the voltage, the exposure time or the number of applications, we may talk about reversible electroporation (RE) or irreversible electroporation (IRE). When the electroporation is reversible, the cell returns to its normal states after several minutes. On the other hand, the IRE occurs when the membrane is altered enough that it loses its role of a physical barrier. Then, the cytoplasm is reversed in the extracellular matrix leading the cell death.

The first publication regarding the subject of the membrane *break-down* was written in 1958 [47], but the study of this phenomenon had a important growth

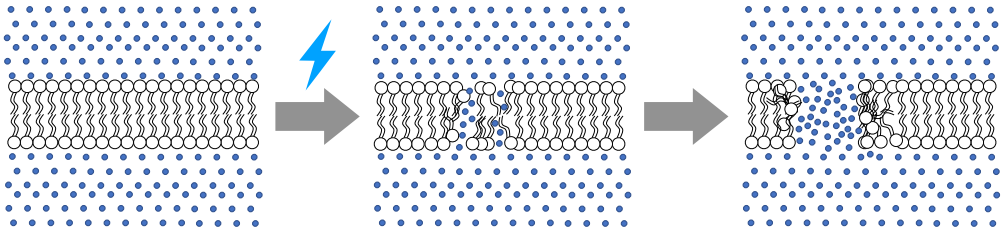

Figure I-5 – The application of an electric pulse on a cell, that increases the transmembrane voltage to a value greater than 1 V, produces a structural change of the membrane and to the formation of pores.

during the 70's [1, 8, 15, 36]. Dating from this period is also the first experiment on living cells trying to extract components from the cytoplasm. The development of the gene therapy during the 80's has boosted the studies of the application of the electroporation to the gene transfer [37]. Today, the main applications of the electroporation concern clinical uses.

The electrochemotherapy (ECT), which found clinical validation in 1991 [34], consists of the local or systemic injection of a non permeant cytotoxic molecule in a tumoral tissue and then the application of a RE pulse. The effect is a considerable augmentation of the absorption of the molecule by the electroporated cells. The advantage of this treatment is, since its local application, the reduction of the side effects of classical chemotherapy. On the other hand, the ECT found difficulties in its application, due to the use of electrodes. In fact, the ECT is suitable for accessible tumors (cutaneous, subcutaneous tumors or tumors attainable after surgery) but it is more difficult to be used percutaneously for deep-seated tumors.

Also the IRE is used in tumor treatment, in particular for the tumor ablation [16, 33]. Compared with the most common radiofrequency ablation, the ablation technique by IRE is less damaging for the extracellular matrix and the nearby tissues.

The electroporation also finds remarkable applications in the food industry, for instance in the preservation and sterilization of food [22, 49].

Objectives of the thesis

Even if the electroporation is widely used, several aspects of the phenomenon are still unexplained, as the effective structural changes of the membrane. Others required further studies, as the correlation between the electroporation treatment setup (intensity of the electric field, duration and number of the pulses, interpulse duration etc...) and its effects (permeabilization rate, permeabilization extension, survival cells quantity, RE-IRE threshold). In fact, the electroporation is an active research subject, and its community counts more than 500 members and is still increasing, due to the relevance of its applications. This community involves biologists, medics, electrical engineers, physicians and mathematicians.

The role of the mathematician is to develop mathematical models capable of describing the electroporation process with simplicity and efficacy. The simulations deriving from mathematical, biological and physical knowledge is a solid support for the *in-vivo* or *in-vitro* experiments, requiring a relatively low time and financial cost. In [19] for example, the authors model the electrical field diffusion during IRE ablation, in [48], the authors worked on molecular dynamics and in [29] on conducting state of the membrane.

This thesis proposes innovative methods for the analysis and the understanding of the phenomenon. The common thread of the thesis is the experimental measures obtained with the new 4-electrode setup proposed by Garcia-Sanchez *et al.* [20] to investigate the cell membrane electrical response to high electrical stimulation.

Linking the measures to an equivalent $R|C$ circuit is far from trivial since the device needs calibration, to account for all the distortion due to the set-up. The first part of the thesis consists in calibrating and estimating the parameters of a well-designed equivalent circuit (EC) to model the 4-electrode experiment in the context of cell monolayer electroporation.

The particularity of 4-electrode setup is to used 2 electrodes to impose the current and 2 other passive electrodes to measure the electrical response of the sample. This complexifies dramatically the mathematical model, because instead of the standard use of Dirichlet-to-Neumann maps as in tomography (the voltage is imposed on the electrode and the current is measured on the same electrode), the 4-electrode setup makes appear the impact of passive electrodes on the applied current, leading to a so-called floating potential problem. In parallel, the 4-electrode device has the huge advantage to limit the influence of bound water in the vicinity of the electrode measurements. Indeed, the thickness of the interfacial water, with specific electrical properties is directly linked to the voltage of the electrodes. For passive electrodes, the thickness is thus much smaller than in the standard 2-electrode set-up. The second part of the thesis is dedicated to analyze an elliptic PDE describing the electroquasistatic approximation of the electric potential in the 4-electrode setup. The main difficulty - which is a common problem with impedance measurement techniques - is due to the presence of these inactive electrodes which are highly conductive and thin. The classical way to model these inactive electrodes consists in using a penalization approach but this leads to numerical instabilities. We propose in this thesis an asymptotic analysis to reduce the model, which also leads to a more accurate and a more robust strategy called floating potential (FP) approach. Finally, we use this FP approach to approximate the electrical potential with the 4-electrode setup for cell monolayer electroporation. We compare the simulated impedances with the measured and calibrated impedances and we obtain very satisfactory results. In this context, the main contributions of this thesis can be summarized in the following points.

- A new calibration strategy for the 4-electrode device of [20] has been proposed.
- We designed an electrical circuit and estimated its parameters using calibrated impedance data for cell monolayer electroporation.
- Asymptotic analysis of the conductivity problem with high conductive thin passive electrodes.
- Validation of the floating potential PDE model for the 4-electrode setup.

Outline of the PhD thesis

The topics covered by this PhD thesis are developed in three chapters.

Chapter 1 - Calibration strategy of electrical circuit with an arranged 4-electrode setup for electroporation

This chapter concerns the data processing related to the electroporation of a cell monolayer. The data are the result of an Electrical Impedance Spectroscopy (EIS). In the beginning, we present the electroquasistatic approximation and we introduce a simple electric system. The goal is to give all the notions necessary to the reading of this chapter. For the same reason, we present the 4-electrode measurement system and the three-reference calibration strategy, both used in the electroporation experiment. Once we have introduced the experimental context, we formalize a new strategy to calibrate the measured impedance data. Finally, we develop a EC model and we use the calibrated observations to estimate the model parameters. The parameter estimation shows the effects of the RE pulse on the cell monolayer.

Chapter 2 - Asymptotic analysis of the conductivity problem with high conductive thin passive electrodes

The focus of this chapter is to model the presence of a thin inactive electrode inside an electric field. This problem arises from the 4-electrode measurement system, in which two electrodes are used to measure the voltage of a sample. We consider a domain Ω of conductivity σ_0 with a hole. We denote by Γ_{int} the interface between the hole and Ω, and Γ the other part of the boundary of Ω. To avoid singularity, we assume that the thin highly conductive electrode $\mathcal{O}^\varepsilon$ surrounds Ω. Γ^ε denotes the boundary of $\Omega \cup \mathcal{O}^\varepsilon \cup \Gamma$. The conductivity σ^ε of the assembly $\Omega \cup \mathcal{O}^\varepsilon \cup \Gamma$ reads

$$\sigma^\varepsilon(x) = \begin{cases} \sigma_0 \\ \frac{1}{\varepsilon^k}\sigma_1, \end{cases}$$

where σ_1 is of the same magnitude order as σ_0. The electrostatic potential u^ε satisfies

$$\begin{aligned} &\nabla \cdot (\sigma^\varepsilon \nabla u^\varepsilon) = 0, \qquad \text{in} \quad \Omega \cup \mathcal{O}^\varepsilon \\ &u^\varepsilon|_{\Gamma_{int}} = \gamma, \qquad \partial_n u^\varepsilon|_{\Gamma^\varepsilon} = 0. \end{aligned}$$

Thanks to an asymptotic analysis, we show that for $k \geq 2$, u^ε can be approximated in Ω by the solution $(u^0, \alpha^0) \in H^1(\Omega) \times \mathcal{R}$ to the floating potential problem:

$$\begin{aligned} &\nabla \cdot (\sigma_0 \nabla u^\varepsilon) = 0, \qquad \text{in} \quad \Omega \\ &u^0_{\Gamma_{int}} = \gamma, \qquad u^0|_\Gamma = \alpha_0, \text{where } \alpha_0 \text{ is such that} \quad \int_\Gamma \sigma_0 \partial_n u^0 ds = 0. \end{aligned}$$

We also show that the penalization method, which consists in solving the problem satisfied by u^ε generates numerical instabilities. The so-called floating potential

problem is standard in electrical engineering, however its numerical implementation generally requires to modify the numerical method by using a specific boundary element method [4]. In this chapter we propose a trick based on Dirichlet-to-Neumann maps to replace the floating potential by a Dirichlet condition. The price to pay is to solve 2 similar elliptic problems, but this can be computed in parallel, and it has the huge advantage to be used on standard finite element/difference softwares, without any modification.

Chapter 3 - Validation of the floating potential model for an arranged 4-electrode setup

The last chapter links the topics treated in the first two chapters. We develop a model to reproduce the electroporation experiment, representing the measurement electrodes with a FP. We extend the FP strategy presented in Chapter 2 for one passive electrode to n passive electrodes. The result is a numerical simulation of the experiment that we use to validate all the innovative elements presented during the thesis.

Chapter 1

Calibration strategy of electrical circuit with an arranged 4-electrode setup for electroporation

1.1 Introduction

The cell establishes with its external environment an equilibrium consisting of an opposition between electric potential and concentration gradient [31]. Surrounded by its membrane, the cell uses it to handle the exchanges with the external environment. The cell membrane has the double role of insulator and diffusion barrier for the movements of ions. The membrane is semipermeable, that means it enables the passage of certain types of ions. Depending on an electric transmembrane voltage, the proteins present on the cell membrane, called ion pump proteins, push these ions to pass through the membrane producing a concentration gradient across the membrane. The ion channels then enables the passage of these elements under the influence of this concentration gradient. The result of this opposition between ion flows is that the transmembrane potential is held at a relatively stable value, called the resting transmembrane voltage. This resting could be perturbed when the cell is subjected to an electric field and produce consistent changes of the membrane permeability [11]. The application of an electric pulse, to increase the transmembrane voltage over a certain threshold (normally 0.2-1 V), has as effect a rearrangement of the molecular structure of the membrane and the formation of pores on it. Due to the presence of these pores, the membrane permeability increases, leading an increased transport of ions, molecules and even macromolecules. This phenomenon is called electroporation.
But how is it possible to know if the applied pulse is strong enough that the electroporation occurs? How long the permeability variation persists? A way to answer these questions could be by measuring the electrical properties of the membrane, such as permeability and conductivity, that during the electroporation are totally different from the standard values. To this end, a valid and widely used tool is the Electrical Impedance Spectroscopy (EIS). The impedance of an electric circuit is a complex number expressing its ability to resist to the passage of current under the effect of an external voltage at some AC frequency. Measuring the variation

of the impedance of an electric circuit as function of the frequencies produces an electrical impedance spectroscopy. The EIS describes the response of the electric circuit at an external perturbation, and it is useful to study its physical and chemical internal structure.
The cell is nothing more than a (really complex) electrical circuit and García-Sánchez et al. [20], have used the EIS to analyse the effect of an electroporation pulse on a cell monolayer. The first part of this chapter consists of providing the theoretical knowledge of electromagnetism behind this experiment and in describing its execution and the resulting data. In particular, an important part focuses on the technique used to perform the EIS: the 4-electrode measurement method. Leaving the details for the next, the 4-electrode measurement method uses a couple of electrodes to apply a pulse on the system under study and another couple of electrodes to measure the effects of the pulse. This technique is widely used to perform the EIS, and it is preferred to the 2-electrode technique, which instead uses the source electrodes to deliver the pulse and to measure the system response, producing some distortion in the measurement [25,43]. As all the chemical-physical measurement techniques, also the 4-electrode method needs a calibration strategy to make its measurement exact and accurate. The standard calibration strategy is the three-reference method, that uses three measurements as references to define a range of impedance module in which the calibration can be performed [5]. In this work, we show why this strategy of three reference measures is not enough robust and we propose a new calibration strategy which is more robust and gives better results.
Once the measurement system is calibrated, the EIS data show exactly the response of the analysed system to an external electrical perturbation. In our case, this system is composed of the cells and the external media where they are immersed. At this point, an analysis of the observation is necessary to investigate the cell-media exchanges and to deduce if the electroporation occurs. To this end, in this chapter, we figure out an appropriate representation by considering each component composing the system in purely electrical terms and we investigate in order to find an electric circuit composed only of pure electrical terms (capacitance, resistance, inductor...) which produces the same impedance of the system. This circuit is called equivalent circuit (EC). Different electrical circuits can produce the same shape of impedances. That is why an intuitive understanding of the electrochemical system has to be done in order to choose the best EC, which has a physical meaning. With an EC, it is possible to deduce an explicit formula of the impedance. Thanks to the latter, one can have a better interpretation of the impedance measurement: it is possible to observe separately the response of the terms composing the under analysis system to external voltage perturbation and thus to extract information on the capacitive and resistive characteristics of each element.
In Section 1.2, we present the electro-quasistatic formulation. In Section 1.3 we use an illustrative example to introduce the concepts of EIS of an electric system and of EC. Moreover, in this section we present the 2-electrode and 4-electrode measurement methods and the three-reference calibration for the latter. Section 1.4 exposes the experiments performed by our collaborator, describing the experiment conditions and the resulting data. In Section 1.5, we talk about the limit of the

three-reference calibration and we propose an new calibration strategy. In the end, in Section 1.6, we propose an EC model and we estimate and interpret its parameters. Conclusion and perspectives are given in Section 1.7.

1.2 Definitions and Electro-quasistatic approximation

Suppose to be known the concept of electric charge, we recall that a moving or standing charge produces two fields of electrical forces: the electric field $\mathbf{E}$ and the magnetic field $\mathbf{B}$. The flow of one or more charges under the effect of electrical forces produces an electric current.

Definition 1. *The amount of charge passing per unit time and unit area through a surface placed perpendicular at the flow is called the current density and is defined by a vector denoted by* $\mathbf{j}$. *Let be* S *a surface and* $\mathbf{n}_S$ *the unit vector normal to* S, *the amount of current* I_S *passing through* S *per unit time is given by*

$$I_S = \int_S \mathbf{j} \cdot \mathbf{n}_S \, dS. \tag{1.1}$$

In a material, the current evolution depends on its physical and chemical characteristics. Then we can define different electrical characteristics depending on the material.

Definition 2. *The ability of a given material to conduct the passage of the current is the so-called conductivity, denoted by* σ. *The SI unit of electrical conductivity is Siemens per meter* ($S{\cdot}m^{-1}$). *The inverse of the conductivity is the resistivity, denoted by* $\rho = \frac{1}{\sigma}$, *and representing the ability of the material to resist the passage of charges. The SI unit of electrical resistivity is in Ohm per meter* ($\Omega{\cdot}m$) *[30].*

Definition 3. *The permeability of a material is its property describing how dense a magnetic field would be if the same amount of current was passed through it. The SI unit of electrical permeability is henries per meter* ($H{\cdot}m^{-1}$) *and its symbol is* μ.

Definition 4. *The ability of a material to store electric charges is called permittivity and it is denoted by* ϵ. *The permittivity is measured in farad per meter* ($F{\cdot}m^{-1}$) *[30].*

Let a material of domain Ω with permittivity ϵ, conductivity σ and permeability μ. The flow of electric particles produces the diffusion of an electric field $\mathbf{E}(\mathbf{x}, t)$ and a magnetic field $\mathbf{H}(\mathbf{x}, t)$, depending on the position $\mathbf{x}$ and the time t. Maxwell-Faraday and Maxwell-Ampere equations read in Ω as:

$$\nabla \times \mathbf{E} = \mu \partial_t \mathbf{H}, \tag{1.2}$$

$$\nabla \times \mathbf{H} = \epsilon \partial_t \mathbf{E} + \sigma \mathbf{E} + \mathbf{j}. \tag{1.3}$$

For biological applications, it is well known that $\mathbf{E}$ can be assumed to be an electro-quasistatic field *i.e.* $\mu \partial_t H \ll 1$. Therefore, Maxwell-Faraday equation (1.2) becomes

$$\nabla \times \mathbf{E} = 0, \quad \text{in } \Omega.$$

It is commonly known that a such field of forces is conservative, then one can define a scalar function u such that

$$\mathbf{E} = -\nabla u \quad \text{in } \Omega. \tag{1.4}$$

where u corresponds to the *electric potential*. It represents the work done against the electric field $\mathbf{E}$ to move one unit of charge from a reference point $\mathbf{x}_0$ to the point $\mathbf{x}$:

$$u(\mathbf{x}, t) = -\int_{\mathbf{x}_0}^{\mathbf{x}} \mathbf{E}(\mathbf{y}, t) \cdot d\mathbf{y}.$$

u is defined at least of an additive constant and its definition depends on the choice of the point $\mathbf{x}_0$ [18]. On the other hand, the definition of the electric field $\mathbf{E}$ does not depend on this constant.
Using the relation between $\mathbf{E}$ and the electrical potential u given in Equation (1.4), Maxwell-Ampere equation (1.3) becomes

$$\nabla \times \mathbf{H} = \epsilon \partial_t(-\nabla u) - \sigma \nabla u + \mathbf{j}. \quad \text{in } \Omega. \tag{1.5}$$

Considering the divergence of previously equation, we obtain

$$\nabla \cdot (\epsilon \partial_t(-\nabla u) - \sigma \nabla u) = 0, \quad \text{in } \Omega. \tag{1.6}$$

This system has to be completed with boundary conditions depending on the considered experiments. They can be, for instance, Dirichlet, Neumann or Robin type boundary conditions.
In case of an alternative current (AC) in time-harmonic regime, the current density as the form

$$\mathbf{j}(\mathbf{x}, t) = \hat{\mathbf{j}}(\mathbf{x})\, e^{i\omega t},$$

where the *peak* $\hat{\mathbf{j}}(\mathbf{x}) \in \mathbb{R}^3$ depends on the position $\mathbf{x} \in \Omega$. ω is called angular frequency, measured in radians per second ($\text{rad} \cdot s^{-1}$). The angular frequency can be write as $\omega = 2\pi f$ where f is the current frequency, measured in Hertz (Hz). For the linearity of Equation (1.5), the potential u assumes a sinusoidal form as follows:

$$u(\mathbf{x}, t) = \hat{u}(\mathbf{x}) e^{i\omega t}, \quad \text{in } \Omega, \tag{1.7}$$

where $\hat{u}$ is the peak of the potential u.
In time-harmonic regime, Equation (1.6) becomes:

$$\nabla \cdot ((\sigma + i\omega\epsilon)\nabla \hat{u}) = 0 \quad \text{in } \Omega.$$

This equation has to completed with boundary conditions.
We want to conclude this section by the definition of the electric impedance.

Definition 5. *The **electric impedance** is a measure of how a given system blocks the current flow when a voltage is applied. More precisely, suppose that some charge pass from a surface to another surface. The current flow between these two surfaces implies a difference of potential. We define the **impedance** given at one surface – considered as the measurement surface – as the ratio of the potential difference and the current flowing across this surface.*

Considering the flow of charges which crosses over two surfaces S_1 and S_2 and Neumann boundary conditions, the impedance becomes

$$Z = \frac{\frac{1}{|S_2|}\int_{S_2} u\, dS - \frac{1}{|S_1|}\int_{S_1} u\, dS}{\int_{S_1} \mathbf{j}\cdot\mathbf{n}_{S_1}, dS}. \tag{1.8}$$

1.3 Illustrative example of electrical characterization of a sample by impedance measurement

Electrical Impedance Spectroscopy

As evidenced in the previous section, in order to totally determine the whole electromagnetic phenomena of a given system, the electric field (or the potential), the magnetic field and the electric properties such as the permittivity, the conductivity, and the permeability have to be known. Often, in a biological system, it is not possible to compute these physical quantities directly, then a indirect strategy has to be employed. As already said, the EIS is widely used to have an overview of its effective electrical characteristics, as the permittivity ϵ and the conductivity σ. The EIS is used in Section 1.4 to investigate the structural changes of a cell-culture after the application of an AC pulse, through the analysis of the cells conductivity variations. The interpretation of the resulting data consists one of the main purpose of this work. Goal of this section is to provide the theoretical principles which facilitate the understanding of the future discussions.

A simple electrical system

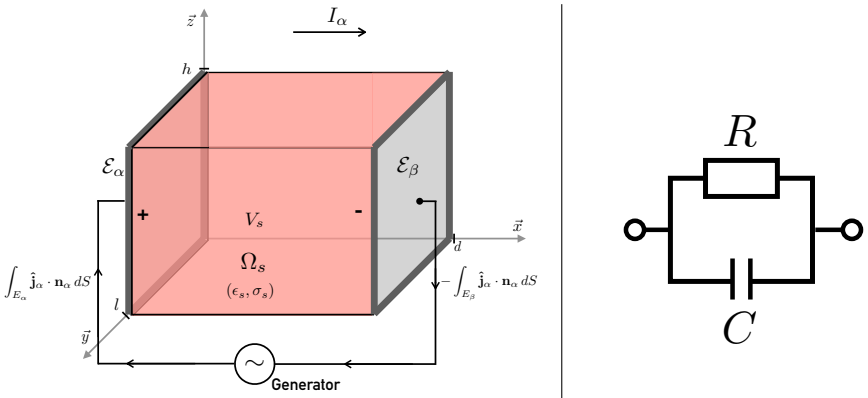

(a) Circuit electrodes-sample. **(b)** $R|C$ circuit schema.

Figure 1.1 – Left: Fundamental electrical system, composed of two plate electrodes surrounding a material sample. Right: the equivalent circuit.

We introduce the simplest electrical system, represented in Figure 1.1a. In a space-time coordinate system $(\mathbf{x}, t)$, with $\mathbf{x} = (x, y, z) \in \mathbb{R}^3$ and $t \in T \subseteq \mathbb{R}$, a

rectangular parallelepiped domain Ω_s, with section $A = l \times h$ and width d, is filled by a homogeneous sample material of which we want to determine the permittivity ϵ_s and the conductivity σ_s. To this end, two plate and parallel electrodes, with surface A, are placed respectively in two parallel sides of Ω_s, indicated with $\mathcal{E}_\alpha$ and $\mathcal{E}_\beta$. Through the electrodes, one can impose the passage of an AC signal on the material in time-harmonic regime, that means that we neglect the temporal dependence. In this example the current density $\hat{\mathbf{j}}$ is supposed to be known and to be uniform on the electrode surfaces:

$$\hat{\mathbf{j}}(\mathbf{x})_{|\mathbf{x}\in\mathcal{E}_k} := \hat{\mathbf{j}}_k, \quad k \in \{\alpha, \beta\}.$$

with $\hat{\mathbf{j}}_k = \left(j_x^{(k)}, j_y^{(k)}, j_z^{(k)}\right) \in \mathbb{R}^3$, $k \in \{\alpha, \beta\}$, constant vectors. We assume that there is no current dissipation in the sample neither current exchanges with the exterior environment. Let $\mathbf{n}_k$ be the normal vectors to the surfaces $\mathcal{E}_k$, $k \in \{\alpha, \beta\}$ directed towards the dielectric. Using the *principle of charge conservation* we obtain that

$$\hat{\mathbf{j}}_\beta \cdot \mathbf{n}_\beta = -\hat{\mathbf{j}}_\alpha \cdot \mathbf{n}_\alpha.$$

Thus, there is no current flow across the other boundaries. In this hypothesis, the spatial evolution of the electric potential $\hat{u}(\mathbf{x})$ is given by the solution of a Laplacian problem, with non homogeneous Neumann conditions on the electrode-dielectric interfaces and homogeneous Neumann conditions otherwise:

$$\begin{cases} -\nabla \cdot ((\sigma_s + i\omega\epsilon_s)\nabla\hat{u}) = 0 & \text{in } \Omega_s \\ (\sigma_s + i\omega\epsilon_s)\partial_{\mathbf{n}_\alpha}\hat{u} = \hat{\mathbf{j}}_\alpha \cdot \mathbf{n}_\alpha & \text{in } \mathcal{E}_\alpha, \\ (\sigma_s + i\omega\epsilon_s)\partial_{\mathbf{n}_\beta}\hat{u} = -\hat{\mathbf{j}}_\alpha \cdot \mathbf{n}_\alpha & \text{in } \mathcal{E}_\beta, \\ \partial_{\mathbf{n}}\hat{u} = 0 & \text{in } \partial\Omega_s \setminus \{\mathcal{E}_\alpha \cup \mathcal{E}_\beta\}, \end{cases} \tag{1.9}$$

where $\mathbf{n}$ is the unit normal vector to $\partial\Omega_s$ inwardly directed. In order to uniquely determine $\hat{u}$, a *Gauge* condition is imposed for instance $\int_{\partial\Omega_s} \hat{u} = 0$. This consists in adding a constraint which removes the redundant degrees of freedom in field variables, for more details see [27].

Simple Calculation to link RC circuit to the PDE

In this section we show that, if we know the solution $\hat{u}$ of System (1.9) we can reach a formula of the sample impedance Z_s, deriving from Equation (1.8) and depending on ϵ_s and σ_s. Moreover we prove that the same formula corresponds to the impedance of a circuit $R|C$, stating that the latter represents a equivalent circuit of the presented system.
Let $\hat{u}$ be the solution of System (1.9). Using Equation (1.1) and recalling the assumption of the material homogeneity, the current through the surface $\mathcal{E}_k$, $k \in \{\alpha, \beta\}$ is given by:

$$\begin{aligned} \hat{I}_k &= \int_{\mathcal{E}_k} \hat{\mathbf{j}}_k \cdot \mathbf{n}_k \, dS \\ &= (\sigma_s + i\omega\epsilon_s) \int_{\mathcal{E}_k} \partial_{\mathbf{n}_k}\hat{u} \, dS, \quad k \in \{\alpha, \beta\}. \end{aligned} \tag{1.10}$$

We recall that the symbol $\wedge$ indicates the *peak* of the current. In fact, it is easy to get that also the current has harmonic behaviour (but shifted of $\phi_{\sigma_s\epsilon_s} = \arg(\sigma_s + i\omega\epsilon_s)$ respect to the potential). That is why, as done for the potential, we neglect its time dependence.
We consider the Cartesian coordinate system as depicted in Figure 1.1a. The surface $\mathcal{E}_\alpha$ and $\mathcal{E}_\beta$ are parallel to the yz plane and they correspond respectively to the coordinate x_α and x_β and on the x axis, with $x_\beta - x_\alpha = d$. Since the charge distribution on the electrodes is uniform, any surface of Ω_s parallel to plan yz is equipotential and the potential varies only along the x direction. The sample is homogeneous and System (1.9) is linear, hence the solution $\hat{u}$ in the form

$$\hat{u}(x) = C_s x + D_s,$$

with $C_s = \frac{j_x}{\sigma_s + i\omega\epsilon_s}$ and D_s determined by the Gauge condition.
Using the same coordinate system, the current can be rewritten as

$$\begin{aligned} I_k &= (\sigma_s + i\omega\epsilon_s) \int_{\mathcal{E}_k} (-1)^{\delta_k} \frac{d}{dx}(C_s x + D_s) dS \\ &= (-1)^{\delta_k}(\sigma_s + i\omega\epsilon_s) C_s A, \qquad\qquad k \in \{\alpha, \beta\}, \end{aligned}$$

with

$$\delta_k = \begin{cases} 0 \text{ if } k = \alpha \\ 1 \text{ if } k = \beta \end{cases}.$$

The voltage $V_{(\alpha,\beta)}$ between the two electrodes is given by

$$\begin{aligned} V_{(\alpha,\beta)} &= \frac{1}{|\mathcal{E}_\beta|} \int_{\mathcal{E}_\beta} \hat{u}\, dS - \frac{1}{|E_\alpha|} \int_{E_\alpha} \hat{u}\, dS \\ &= dC_s, \end{aligned}$$

and applying Equation (1.8) to the system in the Cartesian coordinate system presented before, we have that the sample impedance Z_s is given by

$$Z_s(\omega) = \frac{V_{(\alpha,\beta)}(\omega)}{\hat{I}_\alpha(\omega)} = \frac{-V_{(\alpha,\beta)}(\omega)}{\hat{I}_\beta(\omega)} = \frac{d}{(\sigma_s + i\omega\epsilon_s)A}, \tag{1.11}$$

with magnitude and phase equal to

$$|Z_s(\omega)| = \frac{d}{\sqrt{{\sigma_s}^2 + (\epsilon_s\omega)^2}A}, \tag{1.12}$$

$$\arg(Z_s(\omega)) = -\phi_{\sigma_s\epsilon_s} = -\arctan\left(\frac{\omega\epsilon_s}{\sigma_s}\right). \tag{1.13}$$

Equation (1.11) shows that, if the voltage between the two electrodes and the current flowing through their surfaces are known, one can compute the impedance imposed by the dielectric placed in the middle. This is the principles behind the so-called 2-electrode measurement technique, widely employed in the impedance measurement. This technique will be discussed in Section 1.3.

Equation (1.12) and Equation (1.13) show how the permittivity ϵ_s and the conductivity σ_s of the sample can be estimated using the impedance and system geometry. The following proposition allows to define two properties of an electric system that make it possible to link the PDE System (1.9) and a $R|C$ circuit: the resistance and the capacitance.

Proposition-Definition 1. *It is easy to see that we have the following limit:*

$$\lim_{\omega \to 0} Z_s(\omega) = \frac{d}{\sigma_s A}.$$

The limit is denoted by R

$$R = \frac{d}{\sigma_s A}$$

and it is called resistance. It corresponds to the capacity of an electrical system to resist to the flow of the current.
We also have the following limit:

$$\lim_{\omega \to \infty} i\omega Z_s(\omega) = \frac{d}{\epsilon_s A}.$$

The limit is denoted with $\frac{1}{C}$ where

$$C = \frac{\epsilon_s A}{d}$$

is called capacitance and it coincides with the ability of an electric system to store electrical energy.

Remark 1. *The permittivity ϵ_s is given by:*

$$\epsilon_s = \epsilon_0 \epsilon_r$$

where ϵ_0 is the electrical vacuum permittivity ($8.85 \cdot 10^{-12}$ $F \cdot m^{-1}$) and ϵ_r the relative permittivity depending on the material where the current flows.

It is very easy to show using Definition (1.11) that there is a relation between the impedance, the resistance and the capacitance given by the following proposition:

Proposition 1. *Considering a system as presented in Figure1.1a where a AC signal is imposed and denoting by Z_s its impedance, R its resistance and C its capacitance, we have*

$$\frac{1}{Z_s} = \frac{1}{R} + i\omega C. \tag{1.14}$$

This formula corresponds to the impedance of a $R|C$ circuit (depicted in Figure 1.1b), *i.e.* a resistance R and a capacitance C coupled in parallel. Thus, it comes that for the system exposed in this sections and presented in Figure 1.1a, the corresponding EC is a $R|C$ circuit.

Remark 2. *An EC does not take into account the geometrical properties of the system under analysis. That is why using an EC we can study the resistance and the capacitance related to the elements composing the circuit the but not the conductivity and the permittivity which are specific properties of the the material whose they are composed.*

Impedance spectroscopy data representation

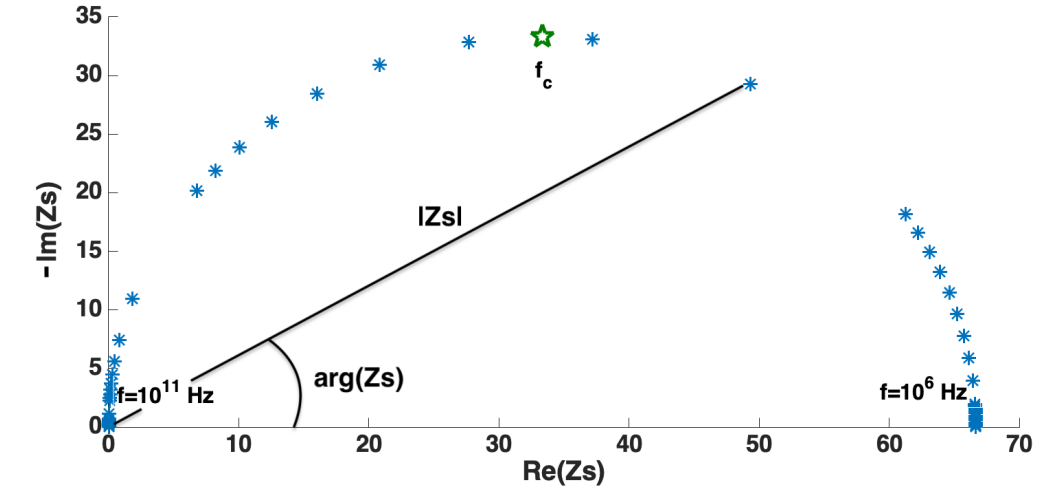

(a) Nyquist plot.

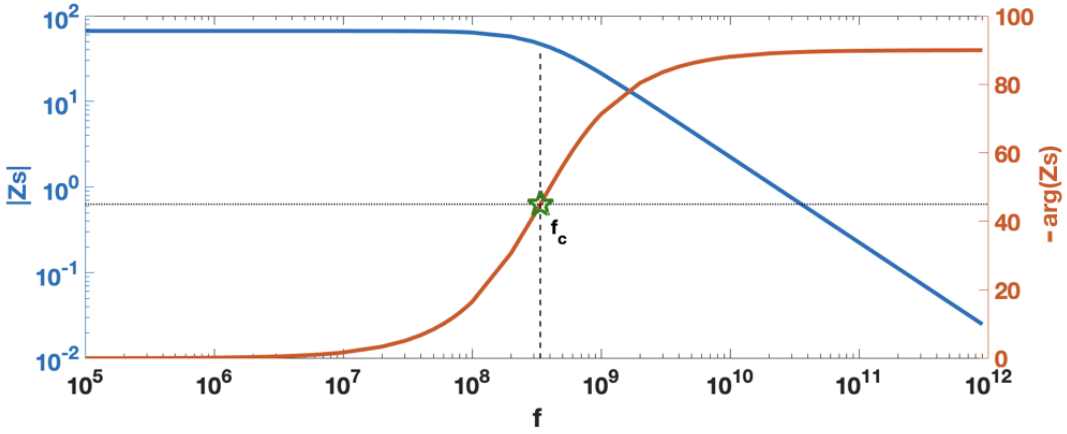

(b) Bode plot

Figure 1.2 – Presentation of the impedance data respectively in a Nyquist plot (up) and in a Bode plot(down)($\sigma = 1.5\text{S}\cdot\text{m}^{-1}$, $d = 10^{-2}\text{m}$, $A = 10^{-4}\text{m}^2$, $\epsilon_r = 80\text{F}\cdot\text{m}^{-1}$).

There are several ways to represent the EIS data. The representation of an impedance Z on the complex plan, plotting the real part $\Re(Z)$ on the x-axis and the imaginary part $\Im(Z)$ on the y-axis, is the so-called Nyquist plot. We present in Figure 1.2a the Nyquist plot associated with the sample impedance Z_s, given by Equation (1.11): the frequencies f are taken between 1MHz and 10^5MHz, where $f = \frac{\omega}{2\pi}$. The y-axis is chosen in negative notation. Each point of the plot corresponds to the impedance related to one frequency. In the Nyquist plot, the impedance can be seen as a vector with module $|Z_s|$ and his direction is given by the angle with the x-axis that is equal to the impedance phase $\arg(Z_s)$. For frequencies $\sim 10^6$ (on the right part of the plot), the resistive aspect is dominant: $\Re(Z_s) = R$ and $\Im(Z_s) = 0$. For greater frequencies, the capacitance C gives his contribution to the total impedance: the imaginary part of the points is bigger when the frequency rises. This happens until the AC frequency value joins the

critical relaxation frequencies $f_c = \frac{\sigma}{2\pi\epsilon}$. The critical frequency f_c corresponds to the midpoint transition where $\Re(Z_s) = \Im(Z_s)$. For frequencies greater than f_c (left part of the plot), the points approach the imaginary axis because the capacitive aspect is dominant, $Z_s \sim \frac{1}{i\omega C}$. The impedance is now inversely proportional to the frequency and then it falls to zero.
In the Nyquist plot, the information about the frequency is not directly provided. Moreover, the Nyquist plot does not show clearly the low impedance values, typically observed at very high frequencies, as in the example exposed. Another way to present the impedance data is by the Bode plot. The Bode plot consists of representing the impedance phase and impedance module as a function of frequency. Figure 1.2b shows the Bode plot related to Equation (1.12) and Equation (1.13) for frequencies between 0.1MHz and 10^6MHz. Observing this plot, one can reach the same conclusions expressed for the Nyquist plot, but it possible to focus on the frequency information. The phase $\arg(Z)$ is equal to zero for low frequencies, $<$ 1MHz, then the impedance has an imaginary part equal to zero and the magnitude is equal to the real part: the impedance is totally resistive and then $|Z| = R$. For frequencies between 1MHz and 10^5MHz, the module decreases and the phase grows, then the imaginary part is non-zero: the total impedance is a combination of both capacitive and resistive impedances. For frequencies greater than 10^4MHz, $\arg(Z)$ tends to $-90°$ and the module $|Z|$ tends to zero: the impedance becomes totally capacitive and it falls to zero for greater frequencies.

Constant phase angle element

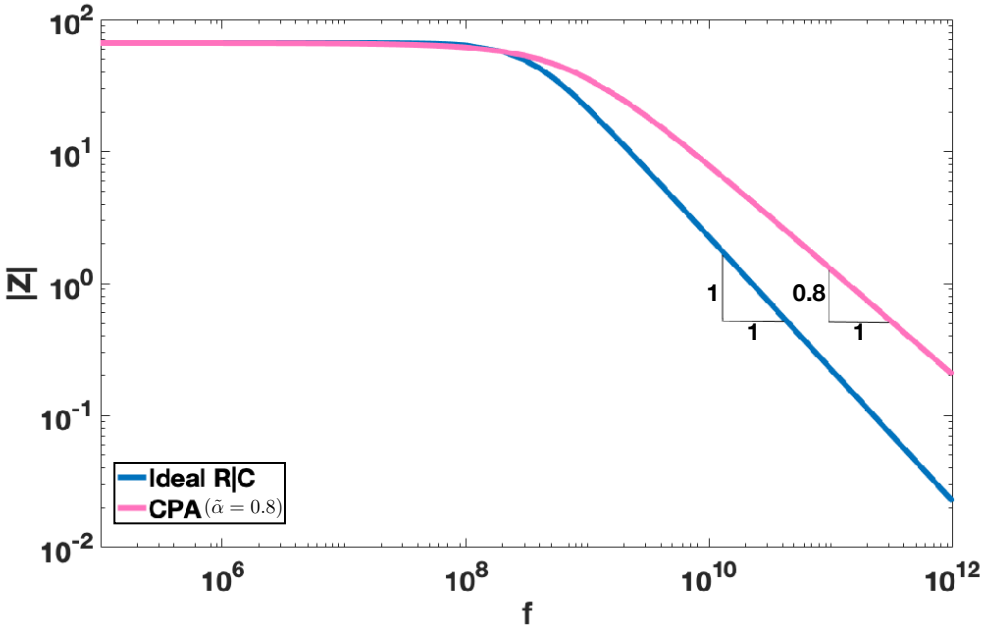

Figure 1.3 – Comparison between the modules impedance of a $R|C$ ideal circuit and a $R|Q$ circuit with $\tilde{\alpha} = 0.8$.

In this section, we present an ideal electrical system, with completely smooth electrodes and homogeneous sample material in the middle, to which corresponds

the Bode plot depicted in Figure 1.2b. In biological applications, a capacitor, such as a lipid bilayer, does not reproduce the same ideal behavior. If a voltage is applied to an electrode not completely smooth or to an inhomogeneous material, the resulting global current is composed of many current filaments, different from each other. The result is frequency-dependent effects as, for example, a capacitive effect that is manifested at higher frequencies. The resulting impedance plot differs from the ideal case shown here. Instead of a Bode plot as in Figure 1.2b, where the magnitude decreases with slope equal to 1 for frequencies higher than 100 MHz, the Bode plot of a non-ideal capacitor has a slope $\tilde{\alpha} < 1$. A way to reproduce this behavior mathematically is by the so-called constant constant phase angle (CPA) element for which the impedance is expressed by

$$Z_{\text{CPA}} = \frac{1}{Q(i\omega)^{\tilde{\alpha}}} = \frac{1}{Q\omega^{\tilde{\alpha}}}\left[\cos\left(\tilde{\alpha}\frac{\pi}{2}\right) - i\sin\left(\tilde{\alpha}\frac{\pi}{2}\right)\right]$$

with $\tilde{\alpha} \in [0, 1]$ and Q [omh$^{-1}\cdot$ s$^{\tilde{\alpha}}$] is the CPA coefficient. This model hypothesis depends on mathematical analysis more than physical theory. A CPA element is an EC used to represent a circuit element whose phase angle is AC frequency-independent. For example, it is employed to model a bilayer capacitor, typically used for EIS experiments. In EIS experiment, the electrodes are often in contact with an electrolyte, *i.e.* an electrically conducting solution. Because of the high current intensity, a thin water layer appears in the electrode-electrolyte interface, (more details in Section 1.3). Due to the difference in conductivity between electrolyte and water, some more realist boundary conditions could take into account to model the system. Then some more explication about the link between CPA element and bilayer capacitor could be available.

The 2-electrode measurement method and its limits

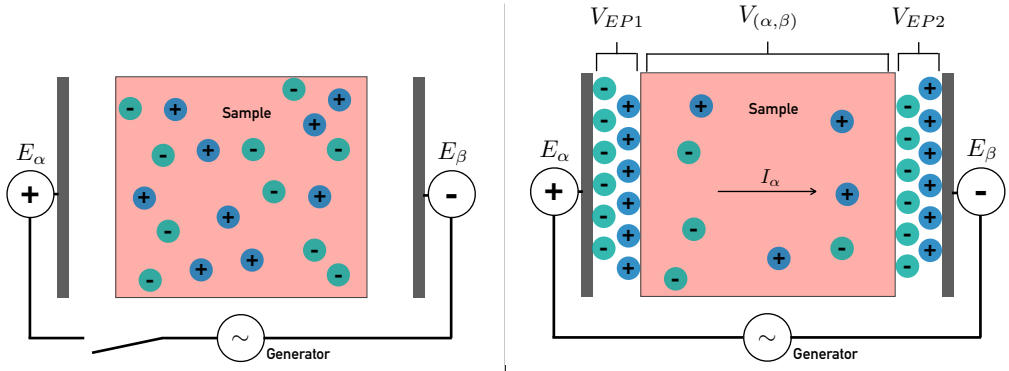

(a) Before the measurement. **(b)** During the measurement.

Figure 1.4 – Under the effect of the electric field, the free ions present in the sample move towards the electrode-sample surface creating an ion double layer that affects the measurement. The phenomenon is called electrode polarization.

Still referring to the 2-electrode system given in Figure 1.1a, the 2-electrode technique is resumed as follows:

1. An AC signal I_α [resp. an AC voltage $V_{(\alpha,\beta)}$] is imposed between the two electrodes and a pulse crosses the sample.
2. The voltage $V_{(\alpha,\beta)}$ [resp. the current I_α] between the two electrodes is then measured.
3. The sample impedance is approximated by the ratio of the voltage $V_{(\alpha,\beta)}$ on the current I_α.

Then, in the ideal case, the impedance Z_{2E} measured with a 2-electrode technique corresponds to the sample impedance given by Equation (1.11).

$$Z_{2E} \simeq Z_s.$$

As shown in the formula, it is only an approximation because this measurement technique, especially in a biologically or highly conductive system, finds some limit. All conductive systems contain free ions. When a metallic electrode is in contact with a sample consisting in a saline solution or in biological tissue, under the effect of an electric field, the ions present in the sample tend to move towards the electrode-sample interface causing the formation of an ionic double layer in such region [25, 42]. We can imagine it as a water layer whose molecules are oriented according to the electric field. As a consequence, when a voltage is imposed by the electrodes, a significant electrical polarization is provoked. This phenomenon is known as electrode polarization (EP). The resulting capacitance, caused by the EP, can dominate the signal at lower frequencies and affect the impedance measurement in the case of a 2-electrode system. As Figure 1.4 depicts, because the EP, the voltage $V^{(EP)}_{(\alpha,\beta)}$ between the two electrodes is

$$V^{(EP)}_{(\alpha,\beta)} = V_{EP1} + V_{(\alpha,\beta)} + V_{EP2},$$

where V_{EP1} and V_{EP2} are the voltage of the two double layers and $V_{(\alpha,\beta)}$ the sample voltage computed in Section 1.3. Then Z_{2E} is equal to:

$$Z_{2E} = Z_s + \frac{V_{EP1} + V_{EP2}}{I_\alpha}.$$

It follows that, not only the measurement is distorted, but also the difference of potential effectively seen by the sample is not what is theoretically imposed by the device.
Then a readjustment of the measurement is necessary. A way to avoid the influence due to the EP is to use a 4-electrode measurement technique that is exposed in the next section.

Four-electrode impedance measurement method

A 4-electrode system is used to perform impedance measurements of a given sample. This technique, born from the need to avoid the distortion induced in a 2-electrode measurement by the EP effect, consists in to employ two electrodes to impose the current and two ulterior electrodes to measure it. It is possible to increase the intern resistance of the measurement system connected to these two

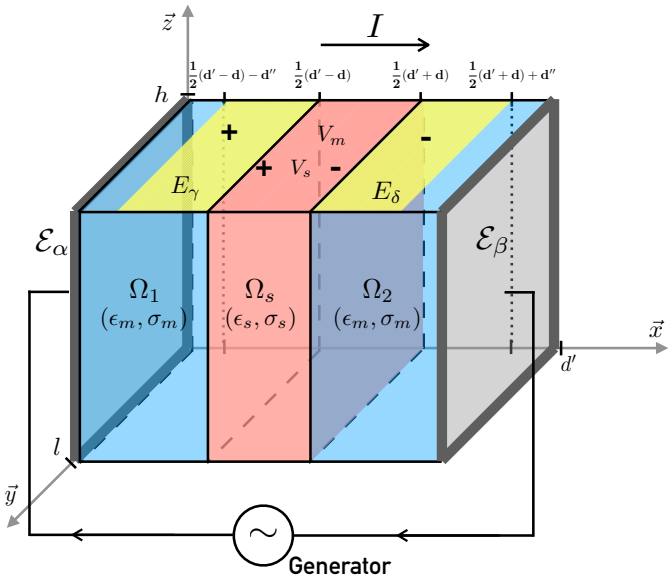

Figure 1.5 – The electrical properties ϵ_s and σ_s of the sample (in red) are estimate using a 4-electrode measurement system composed by the pair of active electrodes in $\mathcal{E}_\alpha$ and $\mathcal{E}_\beta$ (in grey) and the pair of measurement electrodes E_γ and E_δ (in yellow). In this example, in order to estimate σ_s and ϵ_s, is fundamental to know the electrical properties σ_m ans ϵ_m of the surrounding material (in blue) and the dimensions of the different elements composing the system.

last electrodes in order to have a weak current flow: this allows to measure the current (or the voltage) passing on the sample but also to reduce the EP effect on the measurement electrodes [5, 43].
Referring to Figure 1.5, in a space coordinate system with $\mathbf{x} = (x, y, z) \in \mathbb{R}^3$, let's image a rectangular parallelepiped domain Ω (section $A = l \times h$ and width d') filled by a homogeneous sample, occupying at the center a rectangular parallelepiped domain Ω_s (section $A = l \times h$ and width d), and by a surrounding homogeneous conductive material which occupies the domains Ω_1 and Ω_2, $\Omega_1 \cap \Omega_2 = \varnothing$. We want to estimate the sample permittivity ϵ_s and conductivity σ_s knowing the geometric characteristics of the domains Ω_s, Ω_1 and Ω_2, the permittivity ϵ_m and conductivity σ_m of the surrounding material.
Since the homogeneity of both materials, all the passive electrical properties are real constant numbers. The intersections between the sample and the surrounding material consist of two rectangles with area A. They are noted as $\Omega_s \cap \Omega_1 = \Gamma_1$ and $\Omega_s \cap \Omega_2 = \Gamma_2$. As for the 2-electrode system, two plate electrodes of surface A are placed respectively on two parallel sides $\mathcal{E}_\alpha$ and $\mathcal{E}_\beta$ of Ω. Connected to the potential generator, they are employed to impose an alternative current signal from $\mathcal{E}_\alpha$ to $\mathcal{E}_\beta$. Two more electrodes, with height l and width d'', connected to a voltage analyzer, are placed on the surface E_γ and E_δ at the edges of the sample to measure its voltage. We assume that the current flowing through these electrodes is negligible, thanks to a huge resistance inside the voltage analyzer. We assume that the potential and the current are continuous across the surface Γ_1 and Γ_2. We denote the current density in $\mathcal{E}_\alpha$ with $\hat{\mathbf{j}}_\alpha \in \mathbb{R}^3$ and the unit normal vectors to $\mathcal{E}_\alpha$ and to $\mathcal{E}_\beta$ directed towards the dielectric respectively with $\mathbf{n}_\alpha$ and $\mathbf{n}_\beta$. We

assume that there is no current dissipation in both sample and surrounding material neither exchanges with the external environment. Consequently, for the principle of current conservation, the amount of current crossing the surface $\mathcal{E}_\alpha$ is the same through $\mathcal{E}_\beta$. Following this hypothesis, we impose on the sample an AC signal by the active electrodes $\mathcal{E}_\alpha$ and $\mathcal{E}_\beta$:

$$\mathbf{j}(\mathbf{x})_{|\mathbf{x}\in\mathcal{E}_\beta}\cdot\mathbf{n}_\beta = -\mathbf{j}_\alpha\cdot\mathbf{n}_\alpha.$$

The potential $\hat{u}$ is given by the solution of the following problem:

$$\begin{cases} -\nabla\cdot((\sigma_s+i\omega\epsilon_s)\nabla\hat{u}) = 0 & \text{in } \Omega_s,\\ -\nabla\cdot((\sigma_m+i\omega\epsilon_m)\nabla\hat{u}) = 0 & \text{in } \Omega_1\cup\Omega_2,\\ \hat{u}_{|\Gamma_1{}^-} = \hat{u}_{|\Gamma_1{}^+},\\ (\sigma_m+i\omega\epsilon_m)\partial_{\mathbf{n}_\alpha}\hat{u}_{|\Gamma_1{}^-} = (\sigma_s+i\omega\epsilon_s)\partial_{\mathbf{n}_\alpha}\hat{u}_{|\Gamma_1{}^+},\\ \hat{u}_{|\Gamma_2{}^-} = \hat{u}_{|\Gamma_2{}^+},\\ (\sigma_s+i\omega\epsilon_s)\partial_{\mathbf{n}_\alpha}\hat{u}_{|\Gamma_2{}^-} = (\sigma_m+i\omega\epsilon_m)\partial_{\mathbf{n}_\alpha}\hat{u}_{|\Gamma_2{}^+},\\ (\sigma_m+i\omega\epsilon_m)\partial_{\mathbf{n}_\alpha}\hat{u} = \mathbf{j}_{\alpha,\mathbf{x}}\cdot\mathbf{n}_\alpha & \text{in } E_\alpha,\\ (\sigma_m+i\omega\epsilon_m)\partial_{\mathbf{n}_\beta}\hat{u} = -\mathbf{j}_{\alpha,\mathbf{x}}\cdot\mathbf{n}_\alpha & \text{in } E_\beta,\\ \partial_{\mathbf{n}}\hat{u} = 0 & \text{on } \partial\Omega\setminus\{\mathcal{E}_\alpha\cup\mathcal{E}_\beta\},\\ \displaystyle\int_\Omega \hat{u}dx = 0 \end{cases} \tag{1.15}$$

where $\mathbf{n}$ is the unit normal vector at $\partial\Omega$ inwardly directed. Γ_1^- and Γ_1^+ are the surface of Γ_1 in contact respectively with Ω_1 and Ω_s. Γ_2^- and Γ_2^+ are the surface of Γ_2 in contact respectively with Ω_s and Ω_2.
We consider the Cartesian coordinate system as in Figure 1.5: the surface $\mathcal{E}_\alpha$, $\mathcal{E}_\beta$, Γ_1 and Γ_2 are parallel to the yz plane and they correspond respectively to the coordinate $x=0$, $x=d'$, $x=x_1=\frac{1}{2}(d'-d)$ and $x=x_2=\frac{1}{2}(d'+d)$. As seen for System (1.9), in this frame of reference and since both materials are homogeneous, the solution of System (1.15) has the form

$$\hat{u}(x) = \begin{cases} C_s x + D_s & \text{in } \Omega_s,\\ C_1 x + D_1 & \text{in } \Omega_1,\\ C_2 x + D_2 & \text{in } \Omega_2. \end{cases}$$

If we consider the so-called transmission conditions of System (1.15)

$$\begin{cases} \hat{u}_{|\Gamma_1{}^-} = \hat{u}_{|\Gamma_1{}^+},\\ (\sigma_m+i\omega\epsilon_m)\partial_{\mathbf{n}_\alpha}\hat{u}_{|\Gamma_1{}^-} = (\sigma_s+i\omega\epsilon_s)\partial_{\mathbf{n}_\alpha}\hat{u}_{|\Gamma_1{}^+},\\ \hat{u}_{|\Gamma_2{}^-} = \hat{u}_{|\Gamma_2{}^+},\\ (\sigma_s+i\omega\epsilon_s)\partial_{\mathbf{n}_\alpha}\hat{u}_{|\Gamma_2{}^-} = (\sigma_m+i\omega\epsilon_m)\partial_{\mathbf{n}_\alpha}\hat{u}_{|\Gamma_2{}^+}, \end{cases}$$

it is easy to arrive at the conclusion that

$$\begin{cases} C_1 = C_2 = \dfrac{\sigma_s+i\omega\epsilon_s}{\sigma_m+i\omega\epsilon_m}C_s,\\ D_1 = \left(1-\dfrac{\sigma_s+i\omega\epsilon_s}{\sigma_m+i\omega\epsilon_m}\right)C_s x_1 + D_s,\\ D_2 = \left(1-\dfrac{\sigma_s+i\omega\epsilon_s}{\sigma_m+i\omega\epsilon_m}\right)C_s x_2 + D_s, \end{cases} \tag{1.16}$$

where D_s is fixed by the Gauge condition. The effective measured voltage $V_{(\gamma,\delta)}$ is at the edges of the sample. We consider its peak $\hat{V}$, given by

$$\begin{aligned}\hat{V}_{(\gamma,\delta)} &= \frac{1}{|\mathcal{E}_\delta|}\int_{\mathcal{E}_\delta} \hat{u}\, dS - \frac{1}{|\mathcal{E}_\gamma|}\int_{\mathcal{E}_\gamma} \hat{u}\, dS \\ &= C_s\left(\frac{\sigma_s + i\omega\epsilon_s}{\sigma_m + i\omega\epsilon_m}d'' + d\right).\end{aligned}$$

Then the voltage depends only on the sample and electrode sizes. This comes from the hypothesis that the electrodes are placed symmetrically respect to the sample et from the linearity of the solution.
The total current imposed on the system is the current I_α flowing across $\mathcal{E}_\alpha$. The current peak is

$$\begin{aligned}\hat{I}_\alpha &= \int_{\mathcal{E}_\alpha} \mathbf{j}_{\alpha,\mathbf{x}} \cdot \mathbf{n}_\alpha\, dS \\ &= (\sigma_m + i\omega\epsilon_m)C_1 A \\ &= (\sigma_s + i\omega\epsilon_s)C_s A\end{aligned}$$

Then the impedance computed with the 4-electrode technique corresponds to

$$\begin{aligned}Z_{4E}(\omega) &= \frac{\hat{V}_{(\gamma,\delta)}}{\hat{I}_\alpha} \\ &= \frac{1}{A}\left(\frac{d''}{(\sigma_m + i\omega\epsilon_m)} + \frac{d}{(\sigma_s + i\omega\epsilon_s)}\right).\end{aligned} \tag{1.17}$$

Since ϵ_m and σ_m are known, Equation (1.17) provides an explicit formula from which one can deduce ϵ_s and σ_s from the 4-electrode measurement. Moreover, when the electrode width d'' tends to zero, the electrodes can be considered as equipotential surface with the same potential at the sample borders. Then we have

$$\lim_{d''\to 0} Z_{4E}(\omega) = Z_s(\omega),$$

that means that a really good approximation of the sample impedance can be obtained with the 4-electrode measured impedance, if all the properties of Ω_1 and Ω_2 are known.

A three-reference calibration method

The ideal hypothesis assumed in the previous example, *i.e.* the material homogeneity, the continuity of the current flow, the absence of current dissipation, and the definition of the all smooth geometric properties, lead to deduce the explicit formula, Equation (1.17). The latter provides a way to compute the sample properties ϵ_s and σ_s using the 4-electrode technique. In a real-life system, it is not always possible to have the same ideal conditions and it is really hard to achieve an explicit formula that globally explains the studied phenomenon. In fact, the

real-life measurements are performed by using a measurement equipment counting micro-electrodes, voltage analyzer, current analyzer, cable ext. Then the measured impedance reflects not only the sample response but also the impedance imposed by the measurement equipment. Thus the measures have to be "clean" removing the measurement equipment effects. In this section, we present a strategy with which we can empirically calibrate a 4-electrode strategy in order to extract the impedance produced by the sample from the impedance measured. Once achieved the sample impedance, an EC strategy can be implemented to estimate then the sample electrical properties. Further details on this topic are available in [5]. In Section 1.5, we apply the calibration strategy to an EIS experiment performed by our collaborators.

Referring to Figure 1.6a, let us suppose that we want to compute the impedance

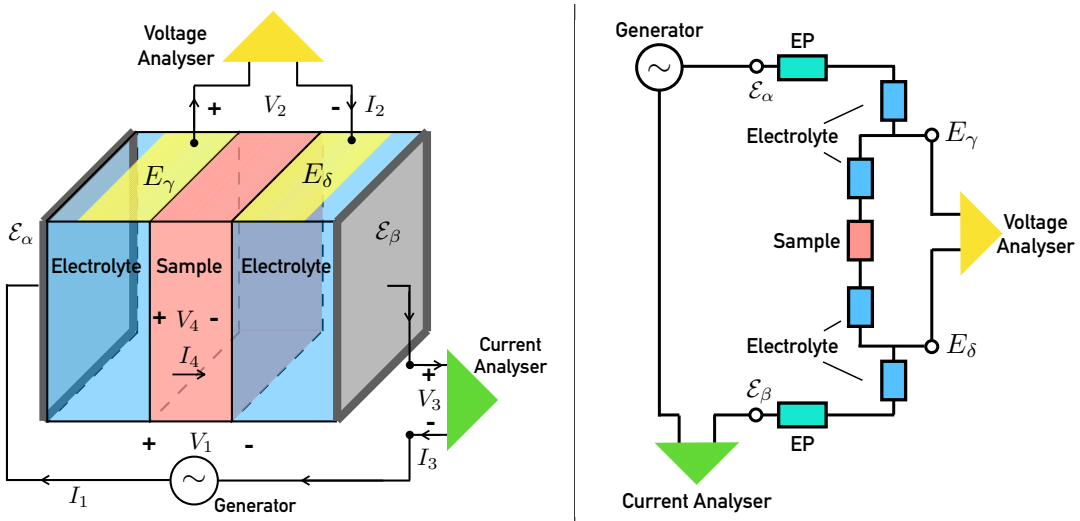

(a) Four-electrode system. **(b)** Four-electrode system EC.

Figure 1.6 – On the left, representation of a 4-electrode system where the AC signal is imposed by a generator of potential connected to two electrodes. Two more electrodes are placed on the system to compute the voltage on the sample and avoid distortions due to the polarization of the active electrodes. Current analyzer is added to measure the total current flowing in the system.

of a sample using a 4-electrode measurement method. To this end, the sample is placed inside a rectangular parallelepiped chamber and surrounded by a conductive solution (electrolyte). In two parallel sides of the chamber, we place two electrodes $\mathcal{E}_\alpha$ and $\mathcal{E}_\beta$. Thanks to a potential generator, an AC signal I_α is imposed from $\mathcal{E}_\alpha$ to $\mathcal{E}_\beta$. Besides, two electrodes E_γ and E_δ, placed in one side perpendicular to $\mathcal{E}_\alpha$ and $\mathcal{E}_\beta$ and connected to a voltage analyzer, are employed to measure the voltage $V_{(\gamma,\delta),m}$ at the edges of the sample. The reader should be aware that the measured voltage $V_{(\gamma,\delta),m}$ is not the true voltage at the sample edges $V_{(\gamma,\delta)}$ as wished, but a measure that has to be calibrated because of the measurement equipment distortion. A current analyzer is plugged into the system to measure the current passing on it. We denote with I_m the current measured by the current analyzer. We do not take into account the geometric properties of this system and then, differently from the example in Section 1.3, it is not possible to explicitly deduce

the spatial evolution of the potential. On the other hand, we can consider the corresponding EC that is depicted in Figure 1.6b: to design the EC we have to take into account the impedance produces by the voltage generator, by the EP of the active electrodes, by the current analyzer, by the sample and by the electrolyte. To quantify the measurement equipment distortion, it can be seen as a four-port electric circuit. In fact, to any port corresponds an element of the measurements equipment that has to be calibrated plus the sample. The elements connected to the ports are: the voltage generator, imposing a potential V_1 and current $I_1 = I_\alpha$; the voltage analyzer, measuring potential $V_2 = V_{(\gamma,\delta),m}$ and having current I_2; a current analyzer, having potential V_3 and measuring a current $I_3 = I_m$; a sample, having potential V_4 and current I_4. Assuming that the ports are linearly related, we obtain the following system:

$$\begin{pmatrix} V_1(\omega) \\ V_2(\omega) \\ V_3(\omega) \\ V_4(\omega) \end{pmatrix} = \begin{pmatrix} Z_{11}(\omega) & Z_{12}(\omega) & Z_{13}(\omega) & Z_{14}(\omega) \\ Z_{21}(\omega) & Z_{22}(\omega) & Z_{23}(\omega) & Z_{24}(\omega) \\ Z_{31}(\omega) & Z_{32}(\omega) & Z_{33}(\omega) & Z_{34}(\omega) \\ Z_{41}(\omega) & Z_{42}(\omega) & Z_{43}(\omega) & Z_{44}(\omega) \end{pmatrix} \begin{pmatrix} I_1(\omega) \\ I_2(\omega) \\ I_3(\omega) \\ I_4(\omega) \end{pmatrix}, \tag{1.18}$$

where the impedances Z_{ij} deriving from the voltage V_i and the current I_j, $i, j \in \{1, 2, 3, 4\}$.
Without going into the details because is not in the interest of this work, the reader should know that this system gives an idea to how the current which reaches any port is a function of all the elements composing the EC.
In order to avoid the polarization of the measurement electrodes, the voltage analyzer has a very large value of impedance, hence the current I_2 flowing on it is negligible compare to the other currents. The current measured by the current analyzer is suppose to be the same as that imposed, thus $I_1 = I_3$. The linear system (1.18) becomes:

$$\begin{pmatrix} V_1(\omega) \\ V_2(\omega) \\ V_3(\omega) \\ V_4(\omega) \end{pmatrix} = \begin{pmatrix} (Z_{11}(\omega) + Z_{13}(\omega)) & Z_{14}(\omega) \\ (Z_{21}(\omega) + Z_{23}(\omega)) & Z_{24}(\omega) \\ (Z_{31}(\omega) + Z_{33}(\omega)) & Z_{34}(\omega) \\ (Z_{41}(\omega) + Z_{43}(\omega)) & Z_{44}(\omega) \end{pmatrix} \begin{pmatrix} I_1(\omega) \\ I_4(\omega) \end{pmatrix}, \tag{1.19}$$

The goal of the experiment is to measure the sample impedance given by

$$Z_s(\omega) = \frac{V_4(\omega)}{I_4(\omega)}.$$

But finally, the effective measured impedance is:

$$Z_{4E,m}(\omega) = \frac{V_2(\omega)}{I_1(\omega)}.$$

From Equation (1.19),

$$Z_{4E,m}(\omega) = Z_{21}(\omega) + Z_{23}(\omega) + Z_{24}(\omega)\frac{I_4(\omega)}{I_1(\omega)},$$
$$Z_s(\omega) = (Z_{41}(\omega) + Z_{43}(\omega))\,\frac{I_1}{I_4} + Z_{44}(\omega).$$

From the last relations, it is easy to get the connection between the sample impedance and the measured impedance:

$$Z_s(\omega) = \frac{Z_{4E,m}(\omega)A_1(\omega) + A_2(\omega)}{Z_{4E,m}(\omega) + A_3(\omega)}, \tag{1.20}$$

$$A_1(\omega) = Z_{44}(\omega), \tag{1.21}$$
$$A_2(\omega) = Z_{24}(\omega)\left[Z_{41}(\omega) + Z_{43}(\omega)\right] - Z_{44}(\omega)\left[Z_{21}(\omega) + Z_{23}(\omega)\right], \tag{1.22}$$
$$A_3(\omega) = -Z_{21}(\omega) - Z_{23}(\omega). \tag{1.23}$$

For a given measurement system and angular frequency ω, $A_n(\omega)$, $n \in \{1,2,3\}$, are complex constants and they can be computed empirically. Considering three reference impedance measurements $(Z^{(l)}_{4E,m}, Z^{(l)}_s)$, $l \in \{1,2,3\}$, which differ only on the analyzed sample and in which both measured impedance and sample impedance are known, we can solve a 3×3 complex linear system where the unknowns are $A_n(\omega), n \in \{1,2,3\}$:

$$\begin{pmatrix} Z^{(1)}_{4E,m}(\omega) & 1 & -Z^{(1)}_s(\omega) \\ Z^{(2)}_{4E,m}(\omega) & 1 & -Z^{(2)}_s(\omega) \\ Z^{(3)}_{4E,m}(\omega) & 1 & -Z^{(3)}_s(\omega) \end{pmatrix} \begin{pmatrix} A_1(\omega) \\ A_2(\omega) \\ A_3(\omega) \end{pmatrix} = \begin{pmatrix} Z^{(1)}_s(\omega)Z^{(1)}_{4E,m}(\omega) \\ Z^{(2)}_s(\omega)Z^{(2)}_{4E,m}(\omega) \\ Z^{(3)}_s(\omega)Z^{(3)}_{4E,m}(\omega) \end{pmatrix}. \tag{1.24}$$

Once the solution (A_1, A_2, A_3) is found, a new unknown impedance measurement is performed to find the sample impedance Z_s by using Equation (1.20).

Remark 3. *In order to set up an efficient calibration strategy, the reference impedances have to be chosen so that their modules have to determine an interval such that the module of any successive measure to calibrate lies in this interval.*

Remark 4. *Once the sample impedance is obtained, in order to estimate the sample properties ϵ_s and σ_s, one has to focus on the sample composition to deduce the dependence of Z_s from ϵ_s and σ_s. This analysis can be done thanks to an EC model of Z_s.*

1.4 Biological measurements of electroporation with 4-electrode setup

Experiments presentation

In García-Sánchez et al. [20], the authors propose a multisine-based approach to perform, for the first time, fast EIS measurements (1 spectrum per millisecond) during the interpulse electroporation interval applied to the cells. For the experiments, a new micro-electrode assembly was proposed. The EIS data are used to characterize and better understand the fast changes produced in the cell membrane during electroporation pulse application.
An important part of this work concerns the analysis of the data resulting from the experiments. This has required a study of the experiment procedure and the setting of the data management based on a mathematical formalization to facilitate their understanding. In what follows, we present the experiment context and procedure and also our data preprocessing work.

Cells and electrolyte

C2C12 myoblasts were seeded into 24 multi-well plates at an initial density of 15×10^3 cells/well. During the experiments, the cells were immersed in an external media consisting of a low-conductivity electroporation (LCE) buffer composed of sucrose, Hepes and MgCl: the buffer contains inside free ions and it leads the passage of an electric current. Its conductivity is $\sigma = 0.098$ S·m^{-1}. Different concentrations of KCl were dissolved in the buffer to vary his conductivity. Different buffers with different conductivities are necessary for the calibration strategy.
Inside the plate, the ratio between the volume occupied by the cells and that occupied by the external media is $\varphi = 0.15$ (value estimated according to our information on the system).

Electrodes and arranged 4-electrode measurement strategy

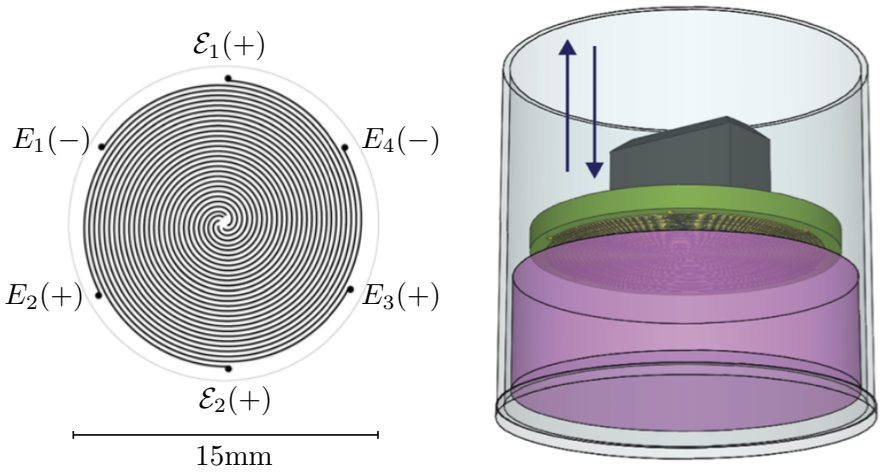

(a) Micro-electrode assembly. **(b)** Experiment set-up.

Figure 1.7 – On the left, a representation of the spiral micro-electrode geometry where are marked the different spirals: two of them are the active electrodes ($\mathcal{E}_1$ and $\mathcal{E}_2$), and the other four (E_1, E_2, E_3 and E_4) are used to measure the voltage. On the right, a representation of the experiment set-up: the micro-electrode is placed above the cells inside a cylindrical plate. Images source: [20].

For the experiments, a micro-electrode was assembly to perform electroporation on the cell monolayer culture and to gather information to the EIS analysis. The micro-electrode, pictured in Figure 1.7a, consists in a disc (15 mm diameter) comprising six equally spaced lines coiled in parallel around the centre of the disc and forming six parallel spirals of almost five loops around the center. Any spiral is an electrode. The dimensions of the lines are 75 μm in width and 150 μm spacing between them. Section 1.4 presents a computation of the electrodes length.
The sample, composed of cells immersed in the buffer or only the buffer, depending on the experiment, was placed in the bottom of a cylindrical plate and the micro-electrode assembly was positioned above the plate, as Figure 1.7b shows. To perform electrical impedance measurements with the present setup, a modified

arrangement of a 4-electrode measurement configuration was employed by duplicating potential measurement terminals. The impedance measurement system is conceived in order to impose an AC voltage V_2 (using the same notation than in Section 1.3) by electrodes $\mathcal{E}_1$ and $\mathcal{E}_2$. Then, the current I_3 was measured after conversion to voltage thanks the other four electrodes coupled two to two (E_1 coupled with E_2 and E_3 coupled with E_4). This configuration with six electrodes leads to increase the area under measure and allow to avoid the error due to local changes.

For a given angular frequency ω, the resulting measured impedance is

$$Z_{4E,m}(\omega) = \frac{V_2(\omega)}{I_3(\omega)}.$$

Actually, the measurement system generate a multisine bursts composed by 26 frequencies between 1kHz and 1MHz. The frequencies in kHz are presented in the following set:

$$\begin{aligned} F_{kHz} &= \{1, 3, 5, 7, 11, 15, 19, 25, 33, 41, 51, 63, 77, 95, 117, 143, \\ &\quad 173, 209, 253, 307, 371, 447, 539, 649, 781, 939\} \\ &= \{f_i | f_{i_1} < f_{i_2} \text{ if } i_1 < i_2\}. \end{aligned}$$

We denote with F the set of the corresponding angular frequencies:

$$F = \{\omega_i = 2\pi f_i | f_i \in F_{kHz},\, i \in \{1, \ldots, 26\}\}.$$

Remark 5. *With **measurement** we indicate the vector composed of 26 under analysis system measured impedances, one for any frequencies presents in F:*

$$(Z_{4E,m}(\omega_1), \ldots, Z_{4E,m}(\omega_{26})).$$

*Any **experiment** counts of more then one measurement.*

Computation of the electrode length

In Chapter 3 we will present the geometric simulations which reproduce the experiments. To this end, it is necessary to compute the electrodes length, that we suppose to be the same for all the electrodes.
To compute the length of one electrode, we consider the parametric equation of a spiral. Suppose an Archimedean spiral place on $x - y$ plane,

$$\begin{cases} x(\theta) &= (a + b\theta)\cos\theta \\ y(\theta) &= (a + b\theta)\sin\theta \end{cases}$$

where the parameter $a \in \mathbb{R}$ is the centerpoint of the spiral outward from the origin to x axis, the parameter $b \in \mathbb{R}$ controls the constant distance between loops and $\theta > 0$ is the angle between the starting and final points of the spiral.
In our case $a = 0$ and $b = \frac{l}{2\pi}$, where $l = (150 + 75) \times 6 \times 10^{-6}m= 1.35 \times 10^{-3}$m is the distance between spiral successive loops, and $0 \leq \theta \leq 10\pi$.
The length of a spiral electrode $\mathcal{E}$ is

$$L(\mathcal{E}) = \int_0^{10\pi} \sqrt{x'(\theta)^2 + y'(\theta)^2} d\theta \approx 0.1 \text{ m}.$$

Remark 6. *In Chapter 3 we will prove that the presented spiral shape electrodes have the same efficacy of straight and parallel electrodes. Thus, the spiral shape allows the compact dimension of the devise.*

Free-cell impedance measurement

To calibrate the measurement system, the three references calibration method seen in Section 1.3 was employed. The reference impedances $(Z^{(l)}_{4E,m}, Z^{(l)}_s)$, $l \in \{1,2,3\}$, were obtained by measuring, with the same setup, the impedance produced by the LCE buffer in absence of cells. In fact, it is possible to theorize the impedance of a saline solution knowing its electrical properties. This discussion is better detailed in Section 1.5. Different concentrations of KCl were dissolved in the buffer. A greater KCl concentration increases the buffer conductivity and this leads to recover a larger range of impedance module, according to Remark 3. A set of experiments were performed with this sample and, for any experiment, the KCl concentration dissolved of the buffer is one of the following set:

$$C_{FC} = \{0\text{mM}, 25\text{mM}, 50\text{mM}, 75\text{mM}, 100\text{mM}\},$$

with mM=mol·m^{-3} (millimolar). For any experiment, 1074 consecutive measurements of the buffer impedance were performed. Figure 1.8 depicts the Bode plots of the impedance measured. Each plot corresponds to an experiment: three experiments were performed at 0mM of KCl and two experiments for the other concentrations. Each plot are designed considering the vector $Z^{(c)}_{FC,\,m}$,

$$Z^{(c)}_{FC,\,m} = (Z^{(c)}_{FC,\,m}(\omega_1), \ldots, Z^{(c)}_{FC,\,m}(\omega_{26})),$$

composed by the average of the 1074 measurements taken during the experiment. Moreover, for the impedances measured at the same frequency $\omega \in F$, we consider the standard variation $\sigma^{(c)}_{ext}(\omega)$ and we design also the interval $[Z^{(c)}_{FC,\,m}(\omega) - 1.96 * \sigma^{(c)}_{exp}(\omega), Z^{(c)}_{FC,\,m}(\omega) + 1.96 * \sigma^{(c)}_{exp}(\omega)]$. Assuming that the measured impedances follow a Gaussian distribution of parameters $\left(Z^{(c)}_{FC,\,m}(\omega), \sigma^{(c)}_{exp}(\omega)\right)$, $\forall \omega \in F$, these intervals contain 95% of the measurements of one experiment.
One can remark that the experiments with the same hypothesis, *i.e.* the same KCl concentration, show behaviours that are distinctly different. This proves a low reproducibility of the experiment, especially at low concentrations. For this reason, we treat separately the information deriving from any experiment.

Impedance measurement with cells

Once obtained the references for the calibration strategy, the experiments used to investigate on the cell electrical properties variations after an electroporation pulse were performed.
During these experiments, the cells were immersed in the same LCE buffer presented in Section 1.4 and also used for free-cell measurements. The direct contact between the electrodes and the cells was prevented by using micro-separators of thickness 10 μm.

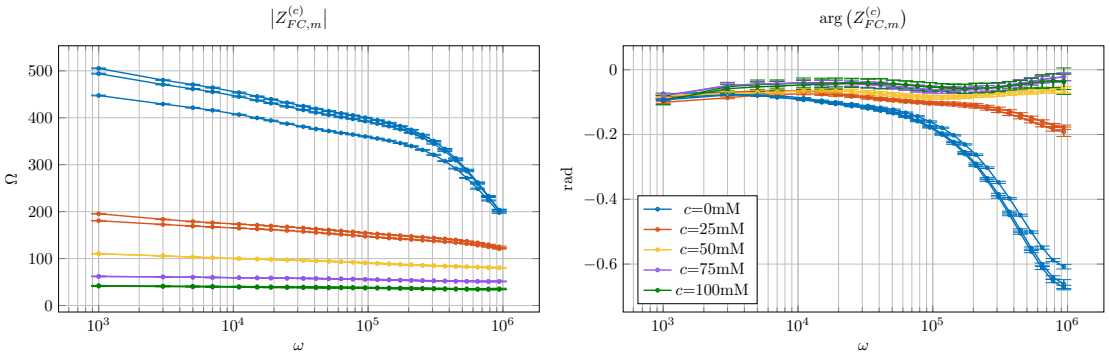

(a) **(b)**

Figure 1.8 – Bode plots (on the left the module and on right the phase) of the impedances measured on five saline solutions which are different from one other for the KCl concentration. Supposed a Gaussian distribution, we draw also the intervals $[Z^{(c)}_{FC,\,m}(\omega) - 1.96 * \sigma^{(c)}_{exp}(\omega), Z^{(c)}_{FC,\,m}(\omega) + 1.96 * \sigma^{(c)}_{exp}(\omega)]$, $\forall \omega \in F$, representing the 95% of the impedances measured at the same angular frequency $\omega \in F$.

The electroporation procedure started with 97 continuous initial pre-electroporation measurements (97 ms). Then the pulse generator was activated: one biphasic pulse was sent with duration 100 μs positive + 10 μs delay + 100 μs negative, frequency 1 Hz. Once the pulse was delivered, a bioimpedance measurement phase starts: 7 multsine bursts (composed by the frequencies $f_i \in F_{kHz}$) were continuously generated and acquired each 200 ms for 5 minutes after the pulse, for a total of $7 \times 1501 = 10507$ measurements.
The experiments differ from each other for the KCl concentration presents in the buffer, resumed in the set

$$C_{WC} = \{0\text{mM}, 5\text{mM}, 10\text{mM}, 20\text{mM}, 30\text{mM}\},$$

and for the voltage v of the elctroporation pulse, with

$$v \in V = \{12\text{V}, 30\text{V}\}.$$

For any couple of $(c, v) \in C_{WC} \times V$, two different experiments were performed.
To illustrative purposes, Figure 1.9 shows all the measurements done during one experiment with 5mM of KCl and an electroporation pulse voltage at 12 V: we can see in green the 97 measurements performed before the pulse and in blue the 10507 measurements after the electroporation pulse. The blue of the after pulse plots becomes clearer at the passage of time. The schema, on the bottom of Figure 1.9, explains the color scale and the sequence of electroporation and measurement signals.
One can remark two distinct behaviors between the observations before and after the pulse and also a continuous decay of the impedance during the time, to give evidence at the electroporation pulse effects. Since the low variation of the measurement before the pulse, for any experiment ($c \in C_{WC}$ and $v \in V$), we decide to take into account their average, denoted with $Z^{(c,v)}_{WC,BP,\,m}$,

$$Z^{(c,v)}_{WC,BP,\,m} = (Z^{(c,v)}_{WC,BP,\,m}(\omega_1), \ldots, Z^{(c,v)}_{WC,BP,\,m}(\omega_{26}))$$

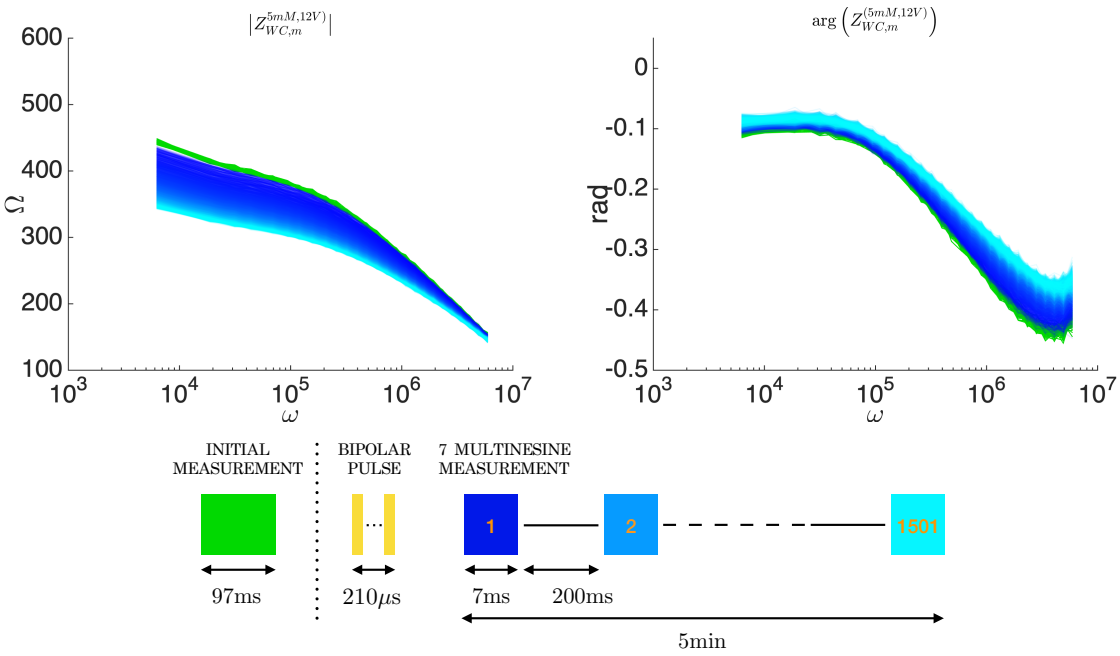

Figure 1.9 – Bode plots (on the left the module and on the right the phase) of the measurements performed during one of the two experiments done with 5mM of KCl in the buffer and an electroporation pulse at 12 V. We can distinguish the measurements before the pulse (in green) and those done after the pulse during five minutes (in blue, increasingly clear at the passage of the time.), as is also explained by the schema on the bottom.

For the same reason, we consider the average, denoted with $Z^{(c,v,t)}_{WC,AP,\,m}$, of the measurements taken at the same instant t after pulse,

$$Z^{(c,v,t)}_{WC,AP,\,m} = (Z^{(c,v,t)}_{WC,AP,\,m}(\omega_1)\ldots, Z^{(c,v,t)}_{WC,AP,\,m}(\omega_{26})),$$

$$t \in T = \{t_n = n \times 200\text{ms}\,|\,n = 1, 2\ldots 1501\}.$$

Even if the data before the pulse would manifest the same behavior, independently on the voltage pulse applied, we indicate the latter in order to point up that the measurements are part of two different experiments.

An ulterior dataset with cells

Another experiment has been performed to investigate the effects of the application of several pulses on the same cell sample.
The electroporation procedure starts with 97 continuous initial pre-electroporation measurements (97 ms). Then the pulse generator is active: 8 biphasic pulses are sent with duration 100 μs positive + 100 μs delay + 100 μ s negative, frequency 1 Hz. Once a pulse is delivered, a bioimpedance measurement phase starts after a fixed delay of 15 ms. The bioimpedance measurement system is conceived in order to impose a voltage by electrodes on the plate and then the current is measured after conversion to voltage: 860 multisine bursts are continuously generated and acquired. Then the pulse generator is reactive and the system waits for the next

pulse (125 ms). The sequence is repeated until completing the eight pulses. The sequence of electroporation and measurement signals is detailed in Figure 1.10.

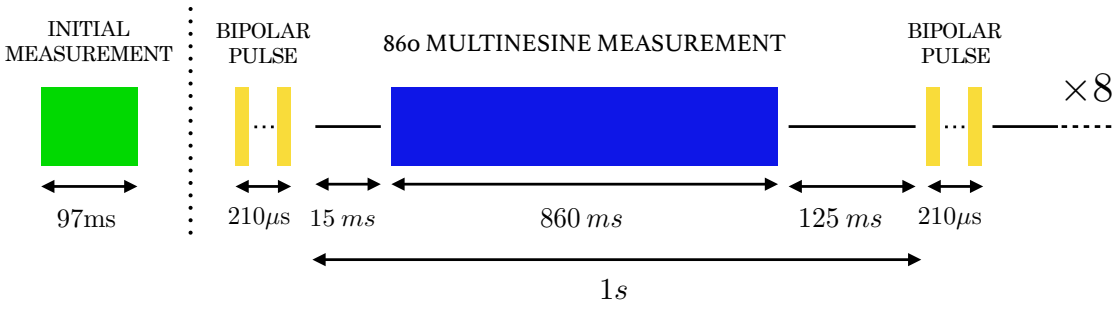

Figure 1.10 – Measurement system block diagram.

The buffer, in which the cells were immersed during the experiments, is always the same already presented in Section 1.4, but, in this case, without an additional concentration of KCl. The experiments differ for the electroporation pulse voltage. Four different voltages have been tested: 9V, 12V, 15V, 21V. Some theoretical issues remain to exploit these data. It is a perspective of this work.

1.5 Calibration method using free-cell data

To remark the effect of the measurement device on the observations, one can observe the free-cell measurement in Figure 1.8. For the range of frequencies used, the buffer response is mostly resistive, *i.e.* frequency independent. On the other hand, observing Figure 1.8a, it is easy to remark a frequency depending behavior of the free-cell measurements (where the sample is composed entirely by the buffer), especially at low KCl conductivity. This effect is due to the measurement system frequency response.
In order to identify this equipment response and to adjust the observations, the three-reference calibration method presented in Section 1.3 is applied. To assess the calibration parameters A_1, A_2 and A_3, three reference impedance couples $(Z_m^{(l)}, Z_s^{(l)})$, $l \in \{1,2,3\}$, are necessary. We recall that $Z_m^{(l)}$, $l \in \{1,2,3\}$, are the buffer impedances measured by a measurement equipment that has to be calibrated, that we can take among the observations $Z_{FC,\,m}^{(c)}$, $c \in C_{FC}$. On the other hand, $Z_s^{(l)}$, $l \in \{1,2,3\}$, are the true (and known) sample impedance that, in this case, is the buffer impedance. We indicate it with $Z_{FC,\,t}^{(c)}$, $c \in C_{FC}$. Our collaborators propose that, for any KCl concentration $c \in C_{FC}$, the true sample impedance corresponds to the measured impedance at angular frequency $\omega_5 = 569115$ rad·s^{-1} $\in F$:

$$Z_{FC,\,t}^{(c)}(\omega) = Z_{FC,\,m}^{(c)}(\omega_5), \quad \forall \omega \in F, \forall c \in C_{FC}.$$

Instead of using a fixed value, we develop a strategy based on modelling.

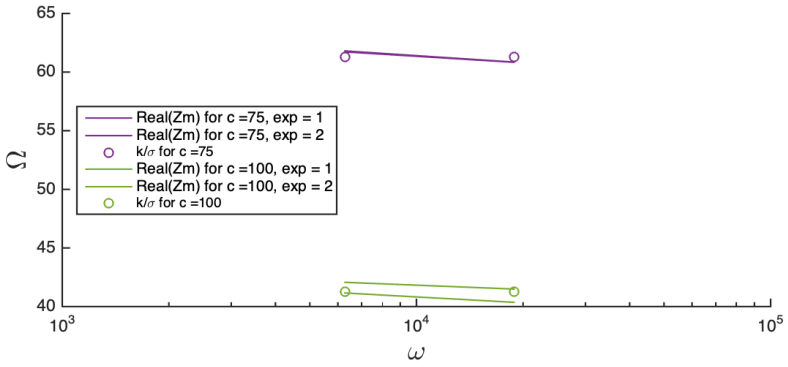

Figure 1.11 – Comparison $\Re\left(Z_m^{(c)}(\omega_i)\right)$ and $\frac{k}{\sigma_{(c)}}$, $c \in \{75\text{mM}, 100\text{mM}\}, i \in \{1, 2\}$.

Buffer conductimetry

As seen in Section 1.3 (Equation (1.11) with $k = d/\text{A}$), the theoretical impedance produced by the buffer, with a KCl concentration $c \in C_{FC}$, can be modelled as

$$Z_{FC,\,t}^{(c)}(\omega) = \frac{k}{\sigma_{(c)} + i\omega\epsilon_{(c)}}, \tag{1.25}$$

where k is a shape factor depending on the plate where the buffer is placed and $\epsilon_{(c)}$ and $\sigma_{(c)}$ are respectively the permittivity and the conductivity of the buffer. We assume that, in the range of angular frequencies in F, the buffer permittivity is frequency independent and comparable to the water permittivity for all concentrations of KCl

$$\epsilon_{(c)} = \epsilon_0\epsilon_r, \quad \forall c \in C_{FC},$$

where ϵ_0 is the vacuum permittivity and ϵ_r is the dielectric constant of distilled water at 25°C, that is comparable to the dielectric constant of a KCl solution, [17]. Table 1.1 reports their values.
To use this model to estimate A_1, A_2 and A_3, the first step consists in estimating k and $\sigma_{(c)}$. At small frequencies, the values of $\sigma_{(c)}$ are very large compared to $\omega\varepsilon_{(c)}$ (at least for high concentrations). Then we assume that:

$$Z_{FC,\,m}^{(c)}(\omega) \sim \frac{k}{\sigma_{(c)}}, \tag{1.26}$$

$c \in \{75\text{mM}, 100\text{mM}\}, \omega \in \{\omega_1 = 6283 \text{ rad} \cdot \text{s}^{-1}, \omega_2 = 18850 \text{ rad} \cdot \text{s}^{-1}\}$. Figure 1.8 confirms this assumption.

We know that the buffer conductivity with no KCl concentration inside is $\sigma_{0mM} = 0.098$ S·m^{-1}. In general, the conductivity of a solution results as the

$\epsilon_0 = 8.8541 \times 10^{-12}$ Fm^{-1} $\quad \epsilon_r = 78.57 \quad \Lambda_0 = 14.98 \times 10^{-3}$ S·m^{-1}·M^{-1}

Table 1.1 – The values of the constants used in the conductimetry and found in the literature [6, 17]

[KCl] (mM)	0	25	50	75	100
$\sigma_{(c)}$ ($S{\cdot}m^{-1}$)	0.098*	0.265	0.57	0.965	1.432

Table 1.2 – Conductivities of the Free-Cell solutions computed thanks to Equations (1.27) and (1.28), with $K = -42.14$. (*) Value already available.

sum of contributions from all ionic species [7]. Then, adding a KCl concentration $c \in C_{FC}$, we can consider the relation

$$\sigma_{(c)} = 0.098 + c\,\Lambda(c), \tag{1.27}$$

where Λ is the KCl molar conductivity ($S{\cdot}m^{-1}{\cdot}M^{-1}$). The compounds that exhibit molar conductivities that do not change significantly with concentration, for example salts as KCl, are called *strong electrolytes*. For these electrolytes, Λ is given by the Kohlrausch's Law:

$$\Lambda(c) = \Lambda_0 - K\sqrt{c}, \tag{1.28}$$

where K is the Kohlrausch coefficient, which depends on the stoichiometry of the specific salt in solution (KCl in this case), and Λ_0 is the molar conductivity at infinite dilution (Table 1.1 reports its value).
In order to estimate k and K we used the data at frequencies ω_1 and ω_2 and related to the KCl concentrations 75 mM and 100mM. For any concentration $c \in \{75\text{mM},100\text{mM}\}$, the data of two different experiments are available and we consider their average $\bar{Z}^{(c)}_{FC,\,m}(\omega_i)$, $i \in \{1,2\}$ (otherwise, using a single experiment for each concentration and then computing the average of the two-parameter estimations obtained leads to the same result). We estimate the parameters k and K thanks to a least-square algorithm present on Matlab (`lsqnonlin`, *trust region reflective*, Copyright 1990-2013 The MathWorks, Inc), that minimizes the cost function

$$p(k,K) = \sum_{c,\omega_i} \left(\bar{Z}^{(c)}_{FC,\,m}(\omega_i) - \frac{k}{0.098 + c\,(\Lambda_0 - K\sqrt{c})} \right)^2 .$$

Figure 1.11 shows the comparison between theoretical and measured impedances, obtained with the estimated parameters $k = 59.13$ and $K = -42.14$. The value of the parameter K is comparable to the value found in the literature, see [35]. Following Equations (1.27) and (1.28), the values of $\sigma_{(c)}$ are directly obtained and are given in Table 1.2.

Estimation of A_1, A_2 and A_3 using only three free-cell data: a huge variability

Following the three-reference calibration method presented in Section 1.3 and considering the observations of three experiments related to three different KCl concentrations $c_1, c_2, c_3 \in C_{FC}$, System (1.24) becomes

$$\begin{pmatrix} Z^{(c_1)}_{FC,\,m}(\omega) & 1 & -Z^{(c_1)}_{FC,\,t}(\omega) \\ Z^{(c_2)}_{FC,\,m}(\omega) & 1 & -Z^{(c_2)}_{FC,\,t}(\omega) \\ Z^{(c_3)}_{FC,\,m}(\omega) & 1 & -Z^{(c_3)}_{FC,\,t}(\omega) \end{pmatrix} \begin{pmatrix} A_1(\omega) \\ A_2(\omega) \\ A_3(\omega) \end{pmatrix} = \begin{pmatrix} Z^{(c_1)}_{FC,\,t}(\omega)\, Z^{(c_1)}_{FC,\,m}(\omega) \\ Z^{(c_2)}_{FC,\,t}(\omega)\, Z^{(c_2)}_{FC,\,m}(\omega) \\ Z^{(c_3)}_{FC,\,t}(\omega)\, Z^{(c_3)}_{FC,\,m}(\omega) \end{pmatrix}. \tag{1.29}$$

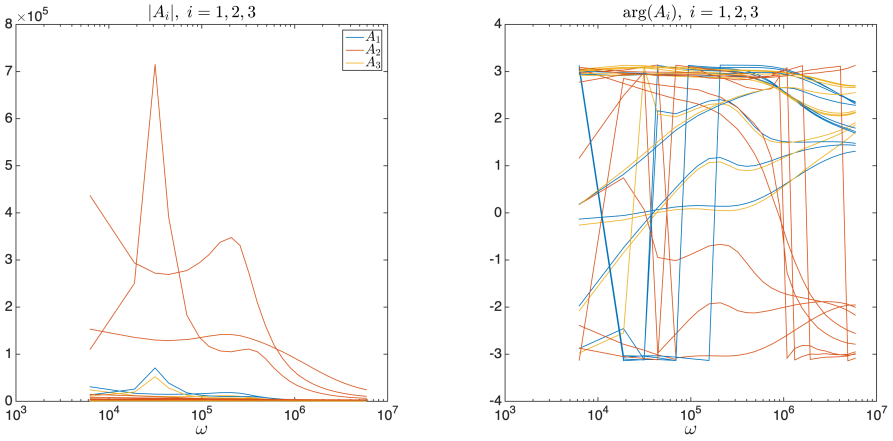

Figure 1.12 – Estimations of (A_1, A_2, A_3) using System (1.29) for all possible configurations.

By solving System (1.29) $\forall\, \omega \in F$, we determine the calibration parameters $A_1(\omega)$, $A_2(\omega)$ and $A_3(\omega)$. Figure 1.12 shows the A_1, A_2 and A_3 computed for all the possible combinations of experiment data related to three different concentrations $c_1, c_2, c_3 \in C_{FC}$. One can remark that the parameters $A_1(\omega), A_2(\omega)$ and $A_3(\omega)$ depend on the choice of the couples $(Z^{(c_l)}_{FC,\,m}(\omega), Z^{(c_l)}_{FC,\,t}(\omega))$, $l \in \{1,2,3\}$. Applying the different calibrations obtained with the three-reference method to the observations with cells, we obtain results really different from each other. Figure 1.13 compares the observations calibrated with the three-reference method (lines) related to four experiments: 20mM and 30mM of KCl concentration and 12V and 30V. One can notice the instability of this approach. We have to conclude that this calibration strategy is not robust when it is applied to this dataset. The failure of this calibration strategy can be explained by the data inaccuracies. More precisely, as seen in Section 1.3, the differences between the three references are the concentration of KCl (which does not seem exactly correspond the theoretical ones) and the sample. Figure 1.14 represents a section of the total system. In this case, the sample corresponds to the buffer portion between the potential measurement terminals. Hence, in the reference observations, not only the sample changes, but the whole buffer. As consequence, the calibration parameters A_1, A_2 and A_3 computed are not the same for all the reference observations. A way to compensate the weakness of the observations is to use the fact that more than three observations are available. As Figure 1.13 shows, the observations calibrated with the new method (dashed line) are of the same order of the other calibrated observations. In the next section, we discuss the details of this new strategy and the advantages of its use.

Estimation of A_1, A_2 and A_3 using all free-cell data: increase of stability

Considering the data of one experiment related to a concentration $c \in C_{FC}$ and fixing $\omega \in F$, for a given set of calibration parameters $A_1(\omega)$, $A_2(\omega)$ and $A_3(\omega)$, one can define a distance function between the *calibrated* sample impedance $Z^{(c)}_{FC,\,cal}$

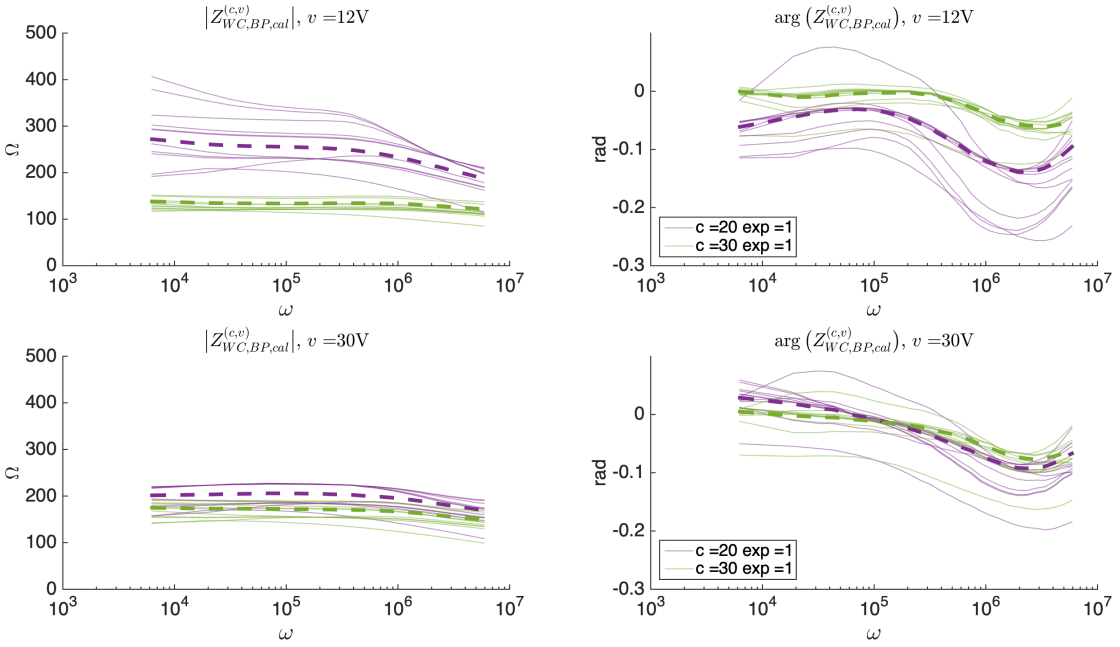

Figure 1.13 – Comparing the three-reference calibration method (lines) with the new calibration strategy (dashed line), we can see the instability of the results obtained with the first approach.

from Equation (1.20),

$$Z^{(c)}_{FC,\,cal}(\omega) = \frac{Z^{(c)}_{FC,\,m}(\omega)A_1(\omega) + A_2(\omega)}{Z^{(c)}_{FC,\,m}(\omega) + A_3(\omega)}, \tag{1.30}$$

with the theoretical sample impedance $Z^{(c)}_{FC,\,t}(\omega)$ given by Equation (1.25). Thus, a way to define the calibration strategy is to find $A_1(\omega)$, $A_2(\omega)$ and $A_3(\omega)$ which minimize the distance function between $Z^{(c)}_{FC,\,cal}(\omega)$ and $Z^{(c)}_{FC,\,t}(\omega)$, for all the available data and $\forall\omega \in F$. One can remark that the minimization problem is already overdetermined since, for each $\omega \in F$, we can use the data of ten experiments, two for each concentrations, to estimate three parameters (A_1, A_2 and A_3). Thus, we have decided to not exploit the information coming from any experiment separately, but to consider the average $\bar{Z}^{(c)}_{FC,\,m}(\omega)$ corresponding to the same concentration $c \in C_{FC}$ and the same angular frequency $\omega \in F$:

$$\bar{Z}^{(c)}_{FC,\,cal}(\omega) = \frac{\bar{Z}^{(c)}_{FC,\,m}(\omega)A_1(\omega) + A_2(\omega)}{\bar{Z}^{(c)}_{FC,\,m}(\omega) + A_3(\omega)}, \quad \forall\omega \in F,\ \forall c \in C_{FC}.$$

As already done for k and K, we estimate the calibration parameters thanks to a least-square algorithm present on Matlab, (`lsqnonlin`, *trust region reflective*, Copyright 1990-2013 The MathWorks, Inc), that minimizes the cost function

$$q(A_1, A_2, A_3) = \sum_{c \in C_{FC},\,\omega \in F} \left(\bar{Z}^{(c)}_{FC,\,cal}(\omega) - Z^{(c)}_{FC,\,t}(\omega)\right)^2.$$

Figure 1.15 depicts the estimated $A_1(\omega)$, $A_2(\omega)$ and $A_3(\omega)$, $\forall\omega \in F$. Figure 1.16 presents the comparison between $Z^{(c)}_{FC,\,t}$ (circle) and $\bar{Z}^{(c)}_{FC,\,cal}$ (line) obtained from

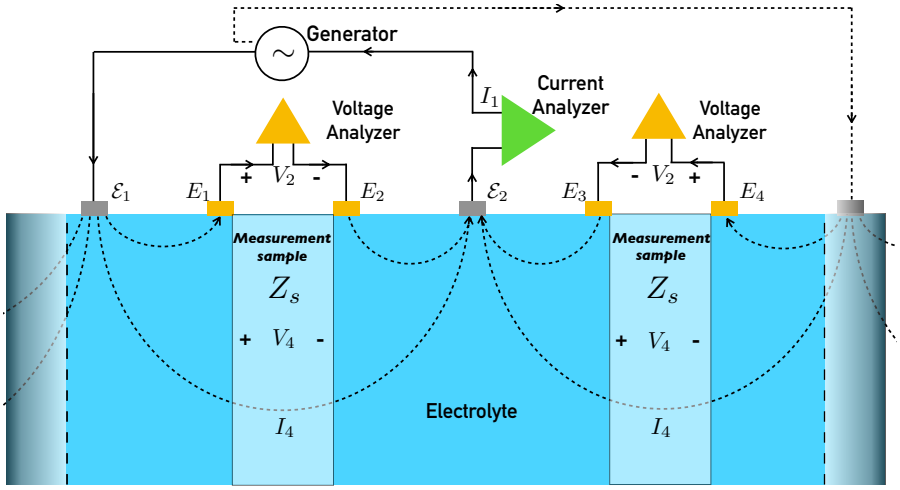

Figure 1.14 – Schema of section of the arranged 4-electrode system applied to the free-cell system. The sample under measure is the portion of buffer between the electrod measurement electrodes as highlighted in figure.

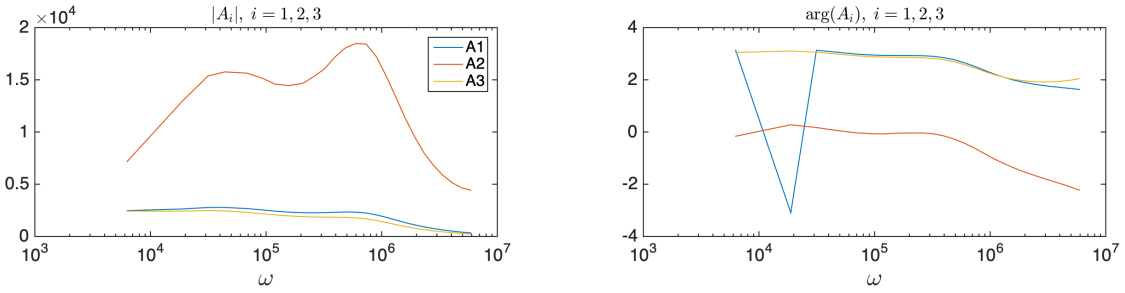

Figure 1.15 – Estimation of (A_1, A_2, A_3) using all the available observations.

the estimated A1, A2 and A3. The result is satisfactory as, in the module, the calibrated impedance follows the expected theoretical behavior. One can remark that KCl concentration of 25 mM, there is a more significant distance between calibrated data and theoretical impedance. We suppose that this is due to some uncertainties on the data (for example higher KCl concentration). Concerning the phase, the calibrated data and the theoretical impedance have different evolutions. But the relative error is still acceptable and we can conclude that the fact to use more available information than the three-reference method produces a more robust calibration.

The calibration strategy is now defined by the $A_1(\omega)$, $A_2(\omega)$ and $A_3(\omega)$ and can be applied (thanks to Equation (1.20)) to the raw data with cells, $Z^{(c,v)}_{WC,BP,\,m}(\omega)$ and $Z^{(c,v,t)}_{WC,AP,\,m}(\omega)$, $\forall\omega \in F$ and $\forall t \in T$. We indicate with $Z^{(c,v)}_{WC,BP,\,cal}(\omega)$ and $Z^{(c,v,t)}_{WC,AP,\,cal}(\omega)$ the calibration results. In Figure 1.9 we have presented all the measurements performed during an experiment with 5mM of KCl in the buffer and an electroporation pulse voltage at 12 V. Figure 1.17 shows the measurements of the same experiment after being calibrated.

The calibrated observations represent the effective frequency response produced by the sample, in this case consisting of cells and buffer. The phenomenon can be

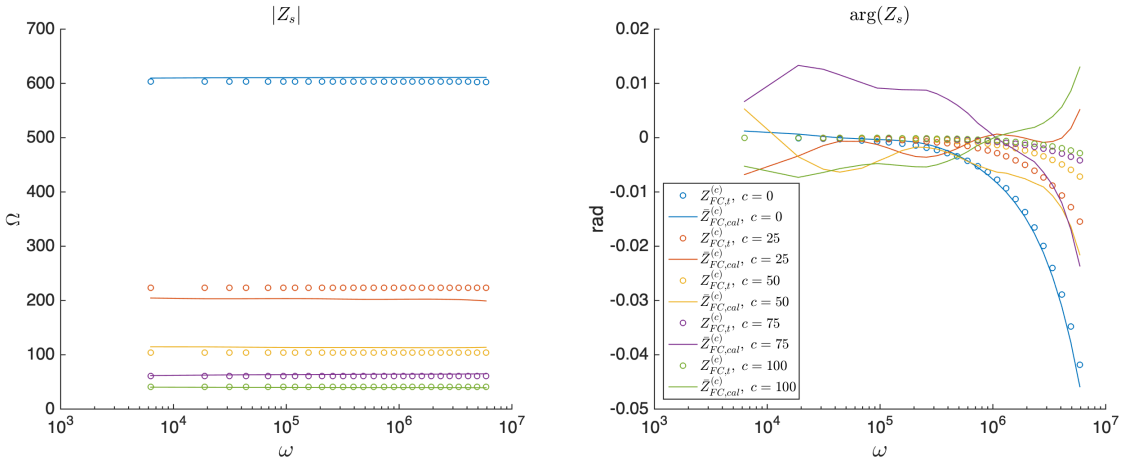

Figure 1.16 – The data (circle), calibrated with the new strategy, follow the expected theoretical behaviour (line). Concerning the phase calibration, even if the results are not perfect there are still acceptable regarding the scale of the figure (< 0.02 rad).

reproduced and studied thanks the EC presented in next section.
We should expect that, for the lowest frequencies in F, the insulating membrane hinders the current from passing through a cell that flows only into the buffer, which means a flat behavior of the calibrated data. Nevertheless, for $\omega < 2 \times 10^4$ rad·s^{-1}, we can observe a low increase in the impedance module. This attitude is stronger for the experiments with lower conduction. A reason is that we probably did not take into account some physical aspects of the studied phenomenon, or just this new calibration method does not compensate for the limits of the three-reference calibration method completely. That is why, to avoid some imprecision deriving from a not perfect calibration, in that follows, we decide not to use the calibrated data with cells related to an angular frequency lower than $\omega_4 = 43982 (= 2\pi \times 7000)$ rad·s^{-1}.

1.6 Equivalent Circuit of the sample in experiments with cells

In this section, we propose an EC model able to reproduce the behavior of the calibrated data resulting from the EIS experiments with cells. The elements composing the EC define the electrical parameters that regulate the under analysis system. The EC is designed to take into account the two elements composing the sample: the buffer and the cells. As Figure 1.18 depicts, the EC is composed of two parallel branches. In one branch, the resistance R_b represents the buffer resistivity: as already seen in Section 1.5, for the range of frequencies used during the experiments, the capacitive nature of the buffer can be neglected and it can be modelled as a pure resistor by Equation (1.26). In the other branch, we consider the cell EC. The biological cell structure is usually reduced to the membrane and the cytoplasm [30]. The cytoplasm presents the same electrical characteristics of an electrolyte and, as done for the external media, we can neglect his capacitive

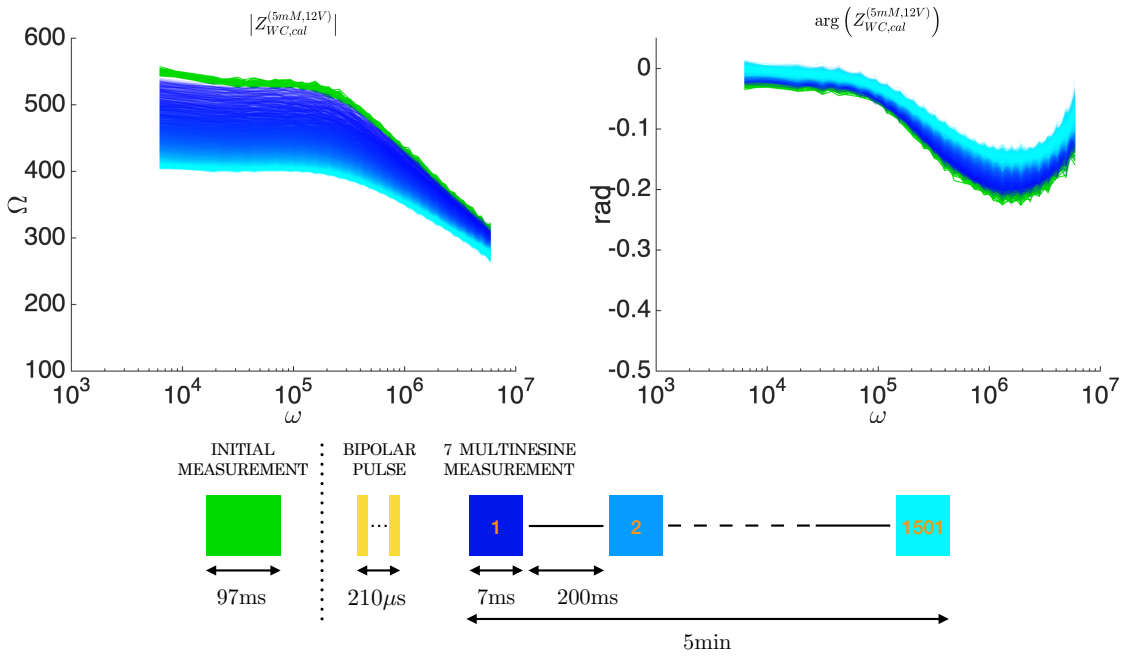

Figure 1.17 – Bode plots (on the left the module and on the right the phase) of the calibrated measurements of one of the two experiments done with 5mM of KCl in the buffer and a electroporation pulse at 12 V. As already done for the raw measurements in Figure 1.9, we can distinguish the measurements before the pulse (in green) and those done after the pulse during five minutes (in blue, increasingly clear at the passage of the time.)

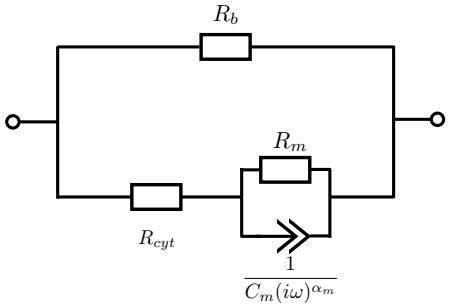

Figure 1.18 – EC for the buffer-cells system.

component and model it as a pure resistor R_{cyt}. In series with the cytoplasm, the membrane can be modelled as a resistance R_m in parallel with a CPA element with parameters C_m and α_m [30]. According to electrical circuit theory and denoting with $\theta = (R_b, R_{cyt}, R_m, C_m, \alpha_m) \in \mathbb{R}^5$ the parameter vector, the impedance $Z_{eq}(\omega, \theta)$ related to this EC respects the following relation:

$$Z_{eq}(\omega, \theta) = \frac{R_b \, Z_{cells}(\omega, \theta)}{R_b + Z_{cells}(\omega, \theta)}, \tag{1.31}$$

where

$$Z_{cells}(\omega, \theta) = R_{cyt} + \frac{R_m}{1 + R_m C_m (i\omega)^{\alpha_m}}. \tag{1.32}$$

$Z_{eq}(\omega, \theta), Z_{cells}(\omega, \theta) : \mathbb{R}^6 \to \mathbb{C}$ are two complex-valued functions of the angular frequency ω and the parameter vector $\theta \in \mathbb{R}^5$. In that follows, we see that with Z_{eq}, according to a properly choice of the vector θ, we are able to fit the calibrated data $Z^{(c,v)}_{WC,BP,\,cal}(\omega)$ and $Z^{(c,v,t)}_{WC,AP,\,m}(\omega)$, $\forall \omega \in F$. This leads to estimate the values of the resistances R_b, R_m and R_{cyt} and the capacitance C_m and then to assess the contributes of any single EC component at the total sample impedance. Fitting separately the observations before and after the pulse allows to study how the parameters evolves over time and to analyse the effects of the electroporation on the cells. We start with the formalization of the estimation problem.

Fixing $\theta \in \mathbb{R}^5$, we denote with $Z_{eq,F}(\theta)$ the vector of equivalent impedances computed for each angular frequency:

$$Z_{eq,F}(\theta) = \Big(Z_{eq}(\omega_4, \theta), \ldots, Z_{eq}(\omega_{26}, \theta) \Big).$$

For an experiment which counts KCl concentration $c \in C_{WC}$ and voltage $v \in V$, we consider the vector

$$Z^{(c,v)}_{WC,\,cal} = \Big(Z^{(c,v)}_{WC,\,cal}(\omega_4), \ldots, Z^{(c,v)}_{WC,\,cal}(\omega_{26}) \Big)$$

related to the its observations before or after the pulse. To fit the vector $Z^{(c,v)}_{WC,\,cal}$, we solve the following minimization problem.

Minimization-Problem 1. *To find the parameter vector $\tilde{\theta} \in \mathbb{R}^5$ which minimizes the function $d^{(c,v)}$:*

$$\tilde{\theta} \in \mathbb{R}^5 \quad s.t. \quad d^{(c,v)}(\tilde{\theta}) = \min_{\theta \in \mathbb{R}^5} d^{(c,v)}(\theta), \tag{1.33}$$

where $d^{(c,v)}$ is the distance function between the vectors $Z^{(c,v)}_{WC,\,cal}$ and $Z_{eq,F}(\theta)$ defined as:

$$d^{(c,v)} : \begin{cases} \mathbb{R}^5 & \to & \mathbb{R}, \\ \theta & \mapsto & \left\| \frac{Z^{(c,v)}_{WC,\,cal} - Z_{eq,F}(\theta)}{Z_{eq,F}(\theta)} \right\|_{l_2}, \end{cases}$$

where $\|.\|_{l_2}$ is the l_2-norm of a complex vector.

Before to pass to the resolution of Minimization-Problem 1, an analytic discussion on the model is necessary. In fact, it is vital to point up that the model composed by Equation (1.31) and Equation (1.32) is **non-identifiable**, *i.e.* two different parameter vectors could give the same (at least very close) impedances: for a given angular frequency $\omega \in F$,

$$\exists\, \theta_1, \theta_2 \in \mathbb{R}^5, \theta_1 \neq \theta_2 \text{ s.t. } Z_{eq}(\omega, \theta_1) = Z_{eq}(\omega, \theta_2).$$

This means that the distance function $\theta \to d(\theta)$ admits local minima and the resolution of Minimization-Problem 1 does not guarantee the estimation of the true parameters values. In fact, the first order Taylor approximation of Z_{eq} when $w = C_m(i\omega)^{\alpha_m}$ tends to zero gives:

$$Z_{eq} = Z_{eq|w=0} + \partial_w Z_{eq|w=0} w + \mathcal{O}(w^2), \tag{1.34}$$

with

$$Z_{eq|w=0} = \frac{R_b(R_m + R_{cyt})}{R_b + R_m + R_{cyt}},$$
$$\partial_w Z_{eq|w=0} = -\frac{(R_m R_b)^2}{(R_b + R_m + R_{cyt})^2}.$$

Thus, when $C_m(i\omega)^{\alpha_m}$ tends to zero, we have:

$$Z_{eq} = Z_{eq|w=0}$$

Figure 1.19 provides an example where two different triplets (R_b, R_m, R_{cyt}) (with acceptable physical values) give two frequency evolutions of the impedance that are very close.

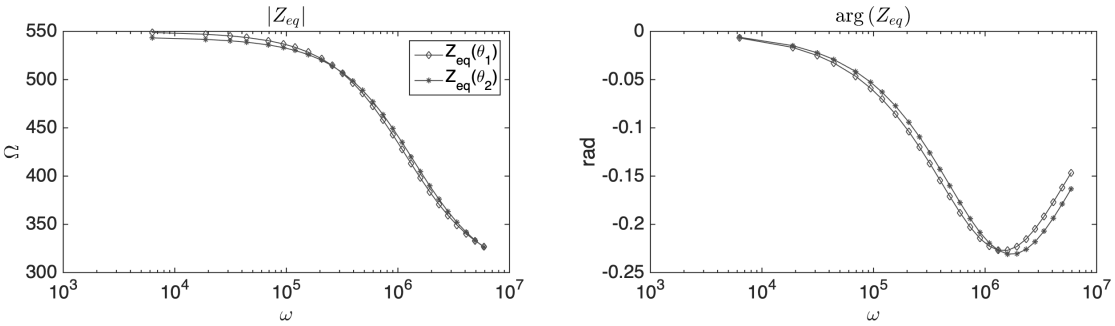

Figure 1.19 – The plots $Z_{eq}(\omega, \theta)$ obtained with $\theta_1 = (572, 594, 1e{-}8, 1e{-}8, 0.82)$ and $\theta_2 = (550, 650, 8e{-}6, 1e{-}8, 0.82)$, $\forall \omega \in F$, show the same behaviour although the difference of the parameters.

To overcome this difficulty, we will reduce the research domain of the parameters. The strategy is presented in what follows: the first next (resp. second) paragraph concerns the estimation of the parameters before (resp. after) pulse.

k=59.13 m^{-1}	$\varphi = 0.15$	σ_{cyt}=0.5 $\text{S}\cdot\text{m}^{-1}$	$S_m = 1$ $\text{S}\cdot\text{m}^{-2}$	$A_m = 2e^4$ m^{-2}

Table 1.3 – The table presents the values of the elements used to define the *a priori* values of the parameters. k and φ are estimated thanks the available geometric information of the under study system. σ_{cyt}, S_m and A_m are provided by the literature [40, 52].

Estimation of the parameters before pulse: $R_m \sim \infty$

The membrane of a living cell acts as a bad conductor. Therefore the resistance R_m is huge respect to buffer and cytoplasm resistances: $R_m \gg R_b, R_{cyt}$. As already seen in Section 1.5 for the buffer resistance R_b, an estimation of the membrane resistance R_m is given by the ratio between the shape factor k of the plate where the experiments are performed and the membrane conductivity σ_m, and since the plate volume is occupied by the cells and the external media, the shape factor k is divided by their volumetric ratio φ:

$$R_m \sim \frac{k}{\varphi\sigma_m}, \tag{1.35}$$

where σ_m is given by

$$\sigma_m = \frac{S_m}{A_m} = 2e^{-4} \text{ S},$$

with S_m the membrane conductance and A_m the ratio between thickness and volume of the membrane. Their values are reported in Table 1.3.
It follows from Equation (1.34) that when $C_m(i\omega)^{\alpha_m}$ tends to zero and R_m tends to infinity, we have:

$$Z_{eq} = R_b.$$

Therefore, the value of R_b affects more incisively the impedance than the other parameters. Other assumptions on the parameters would be useful. Calibrated impedance data seem to be independent of the frequencies for $\omega < 2e^5$ $\text{rad}\cdot\text{s}^{-1}$, see Figure 1.17 for example. Then we assume that, in this range of angular frequencies, the current can not pass through the membrane and then it flows only through the buffer. According to our choice of EC, it means that the term $C_m(i\omega)^{\alpha_m}$ has to be negligible for this range of angular frequencies. Thus, we choose $C_m < 1e-8$. The parameter α_m has a really low influence on the fitting. Thus, we suppose that its value is constant respect to the buffer conductivity and is equal to the average of the estimated values.
As already seen in Section 1.5, the buffer resistance R_b depends on the KCl concentrations $c \in C_{WC}$. From Equation (1.26) derives the approximation

$$R_b \sim \frac{k}{(1-\varphi)\sigma_{(c)}}. \tag{1.36}$$

We recall, k is the shape factor of the plate where the experiments are performed,

φ is the volumetric ratio of the cells and the external media inside the plate. The values of k and φ are reported in Table 1.3. The last relation provides an *a priori* estimation of R_b and we can define its *trust region* as follows

$$R_b \in \left[\frac{k}{(1-\varphi)\sigma_{(c)}}(1-\varepsilon_b), \frac{k}{(1-\varphi)\sigma_{(c)}}(1+\varepsilon_b)\right], \ \varepsilon_b = 0.9.$$

As already exposed, the resistance R_b has to correspond to the impedance module of the observations at the lowest frequencies of F. For this reason, we give a certain flexibility to its research domain, fixing $\varepsilon_b = 0.9$. As well, the cytoplasm resistance R_{cyt} depends on the cytoplasm conductivity σ_{cyt} (its value is reported in Table 1.3):

$$R_{cyt} \sim \frac{k}{\varphi\,\sigma_{cyt}}. \tag{1.37}$$

Then we can define the *trust region* for R_{cyt} as follows

$$R_{cyt} \in \left[\frac{k}{\varphi\,\sigma_{cyt}}(1-\varepsilon_{cyt}), \frac{k}{\varphi\,\sigma_{cyt}}(1+\varepsilon_{cyt})\right], \ \varepsilon_{cyt} = 0.25.$$

The resistance R_{cyt} has a lower influence on the fitting. Then, we assume that R_{cyt} is almost constant respect to the buffer conductivity and its value is close to the *a priori* estimation: we fix $\varepsilon_{cyt} = 0.25$.

The definition of the *trust regions* for each parameter reduces the domain of definition of the distance function $d(\theta)$. Now we pass to the resolution of Minimization-Problem 1. To this end, we use an iterative least-squares algorithm called *trust region reflective*, that is present on Matlab (`lsqnonlin`, Copyright 1990-2013 The MathWorks, Inc). This algorithm looks for the minimum of the distance function $d^{(c,v)}$ in the union of the *trust regions*. When a parameter vector to which corresponds a lower value of the distance function is found within the *trust region*, the region is expanded. Otherwise, the region is contracted in order to converge to the minimum. More details about *trust region* algorithms are present in [13].
Table 1.4 presents the parameters estimated with the *trust region reflective* algorithm and Figure 1.20 shows the resulting fits. One can observe that the EC model can reproduce the behavior of the data with realistic values of the parameters. As Table 1.4 states, the error of the fits respect to the calibrated data is always less than 1.5% ($\|.\|_{l_2} \times 100(\%)$). The results are satisfactory and validate the modelling and the calibration strategy.

Remark 7 (Consequences of an imperfect calibration method)**.** *We recall that the calibration produces some imprecisions at low frequencies. Thus, the calibrated data for frequencies inferior to ω_4 have been neglected. As Figure 1.21 shows, the EC model is not able to fit the phases at low frequencies.*

Estimation of the parameters after pulse

This section concerns the estimation of the parameters related to the observations after the electroporation pulse.
Recalling the electroporation theory, once the pulse is applied, the permeability

Voltage (V)	12				
KCl (mM)	0	5	10	20	30
$R_b(\Omega)$ (exp 1)	703	543	422	259	136
$R_b(\Omega)$ (exp 2)	818	554	338	188	162
$R_{cyt}(\Omega)$ (exp 1)	670	669	655	591	778
$R_{cyt}(\Omega)$ (exp 2)	719	619	651	877	670
C_m(F) (exp 1)	9.99e-09	9.81e-09	9.55e-09	9.74e-09	5e-09
C_m(F) (exp 2)	1e-08	1.06e-08	8.64e-09	5.11e-09	6.22e-09
α_m (exp 1)	0.82	0.82	0.82	0.82	0.82
α_m (exp 2)	0.82	0.82	0.82	0.82	0.82
Error $\|.\|_{l_2}$(exp 1)	0.00123	0.00124	0.0012	0.00122	0.00175
Error $\|.\|_{l_2}$(exp 2)	0.0012	0.00121	0.00116	0.00153	0.00138
Voltage (V)	30				
KCl (mM)	0	5	10	20	30
$R_b(\Omega)$ (exp 1)	1.34e+03	403	343	207	173
$R_b(\Omega)$ (exp 2)	-	531	306	208	140
$R_{cyt}(\Omega)$ (exp 1)	696	666	756	740	773
$R_{cyt}(\Omega)$ (exp 2)	-	670	797	776	594
C_m(F) (exp 1)	9.16e-09	8.15e-09	8.5e-09	6.89e-09	5.67e-09
C_m(F) (exp 2)	-	9.15e-09	7.79e-09	6.35e-09	5.87e-09
α_m (exp 1)	0.82	0.82	0.82	0.82	0.82
α_m (exp 2)	-	0.82	0.82	0.82	0.82
Error $\|.\|_{l_2}$(exp 1)	0.00142	0.000978	0.00119	0.00109	0.000899
Error $\|.\|_{l_2}$(exp 2)	-	0.00106	0.0012	0.00112	0.00139

Table 1.4 – Estimation of the parameters for all the experiments.

of the cells decreases considerably and the exchanges between the cytoplasm and the external media (the buffer) raise. In the case of reversible electroporation, the permeability alteration persists for several minutes. During this period, since the passage of ions across the membrane, the membrane resistance at the current flow decreases significantly.
Figure 1.17 shows the (calibrated) impedances produced by the sample (buffer and cells) during an experiment with $c = 0$mM and $v = 12$V: we can observe that the impedance decreases with the time. This behavior is common to all the experiments. This phenomenon is due to the structural alteration of the cell membrane. As previously, we will fit the EC depicted in Figure 1.18 to the data by estimating the parameters. In this case, R_m is of the same order of the other resistance R_b and R_{cyt}. Then, the model is not identifiable and, to circumvent this difficulty, we will constraint the values of the parameters using physical knowledge of the electroporation processus. We assume that R_m evolves over time because of the electroporation effects, nevertheless we suppose that its variation is independent of the buffer conductivity. We suppose that also the other cell parameters, R_{cyt}, C_m and α_m behave similarly whatever the buffer. On the other hand, we suppose that they do not change after the electroporation pulse and they are constant during the time. Concerning R_b, we assume that it changes during the time because of

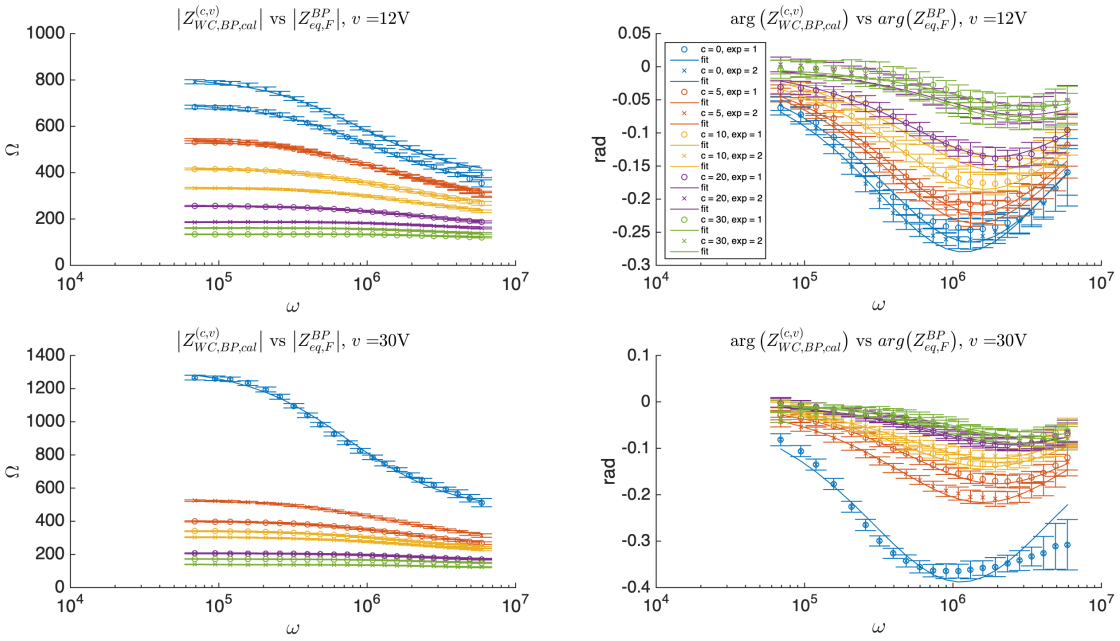

Figure 1.20 – After the parameter estimation strategy, the model fits properly the calibrated data. Different colors correspond to different KCl concentrations. The plots with the same color correspond at the same KCl concentration (but for different experiments).

the cell-buffer exchanges. For any experiment, we choose as *a priori* value the value $R_{b,estim}$ estimated right before the pulse. Thus, for an experiment with a KCl concentration $c \in C_{WC}$ and pulse voltage $v \in V$, the *trust region* of R_b is

$$R_b \in \left[R^{(c,v)}_{b,estim}(1-\varepsilon_b), R^{(c,v)}_{b,estim}(1+\varepsilon_b)\right]$$

and with $\varepsilon_b = 0.3$
We can identify an supremum for R_m thanks to Equation (1.35):

$$R_m^{(max)} = \frac{k}{\varphi\sigma_m}, \tag{1.38}$$

where φ is supposed to behave similarly whatever the buffer. Thus, we impose a *trust region* for R_m as follow:

$$R_m \in [0, R_m^{(max)}].$$

Since the other cell parameters are supposed to be constant respect to the time and the buffer conductivity, R_m has an important role in the fitting of the after pulse data. For this reason, we leave more flexibility to its domain of research.
Figure 1.22 shows the temporal evolutions of the estimated parameters R_b and R_m during the five minutes after the electroporation pulse. As expected, the electroporation pulse application causes a decrease of the membrane permeability, which can be traduced as a reduction of the membrane resistance R_m during several minutes, as depicted in Figure 1.22c and in Figure 1.22d. Consequently, the pulse application stimulates the buffer-cell exchanges (which contain ions) and this increases

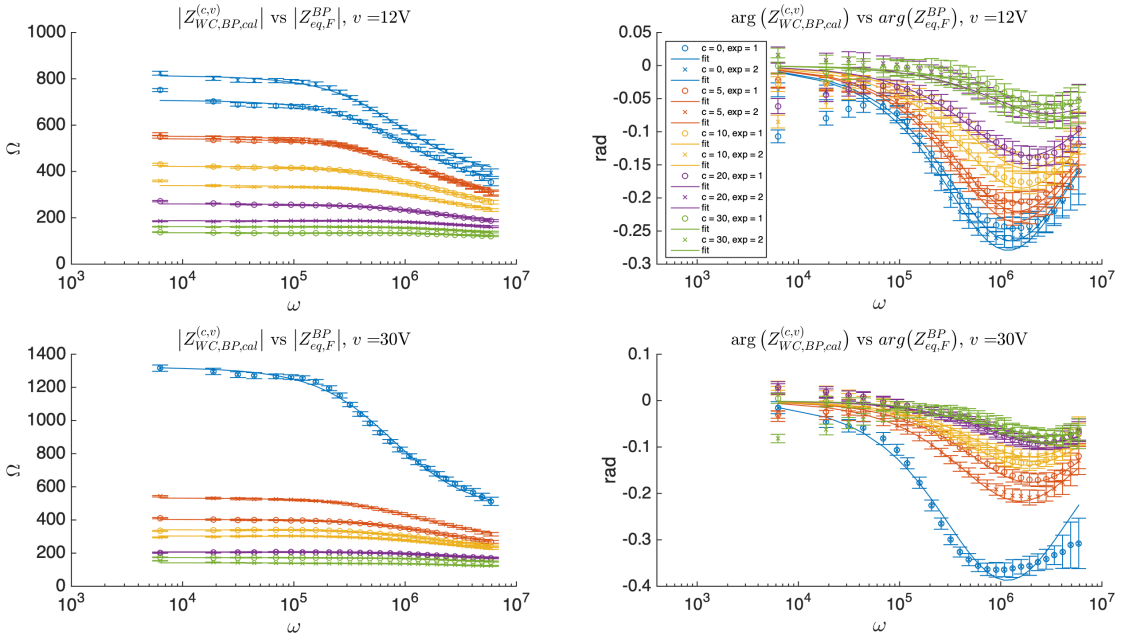

Figure 1.21 – Because of some calibration imprecision then we use also the calibrated impedance data at low frequencies, we are not able to fit the behaviour of the phase at small frequencies.

the buffer conductivity. In fact Figure 1.22a and Figure 1.22b show that R_b starts at the values estimated before the pulse (negative time) and decreases during the minutes after the pulse. The phenomenon is accentuated at higher pulse voltage.

Voltage (V)	12				
KCl (mM)	0	5	10	20	30
Error $\|.\|_{l_2}$(exp 1)	0.0012	0.0013	0.0012	0.0012	0.0019
SD (exp 1)	3.79e-05	3.5e-05	3.76e-05	5.12e-05	6.66e-05
Error $\|.\|_{l_2}$(exp 2)	0.0012	0.0013	0.0012	0.0016	0.0014
SD (exp 1)	3.23e-05	8.7e-05	4.17e-05	5.84e-05	6.05e-05
Voltage (V)	30				
KCl (mM)	0	5	10	20	30
Error $\|.\|_{l_2}$(exp 1)	0.0016	0.0027	0.0014	0.0011	0.0011
SD (exp 1)	0.0002	0.0006	9.05e-05	5.75e-05	8.46e-05
Error $\|.\|_{l_2}$(exp 2)	0.0016	0.0019	0.0014	0.0011	0.0017
SD (exp 1)	0.0002	0.0003	0.0001	6.5e-05	0.0001

Table 1.5 – The parameter estimation result for all the experiments.

Table 1.5 reports the averages over time of the error between the fits and the observations and the standard variations respective. Since the error is always less that the 0.3% ($\|.\|_{l_2} \times 100(\%)$), we consider that our choice of the EC model and the parameter estimation strategy are satisfactory. We want to emphasize that the hypothesis done on the parameter *a priori* values and the related *trust region* play an important role on the estimation strategy. In special way, without the hypoth-

esis of the independence of R_m on the buffer conductivity, we can not achieve to a realistic time evolution estimation of this parameter.

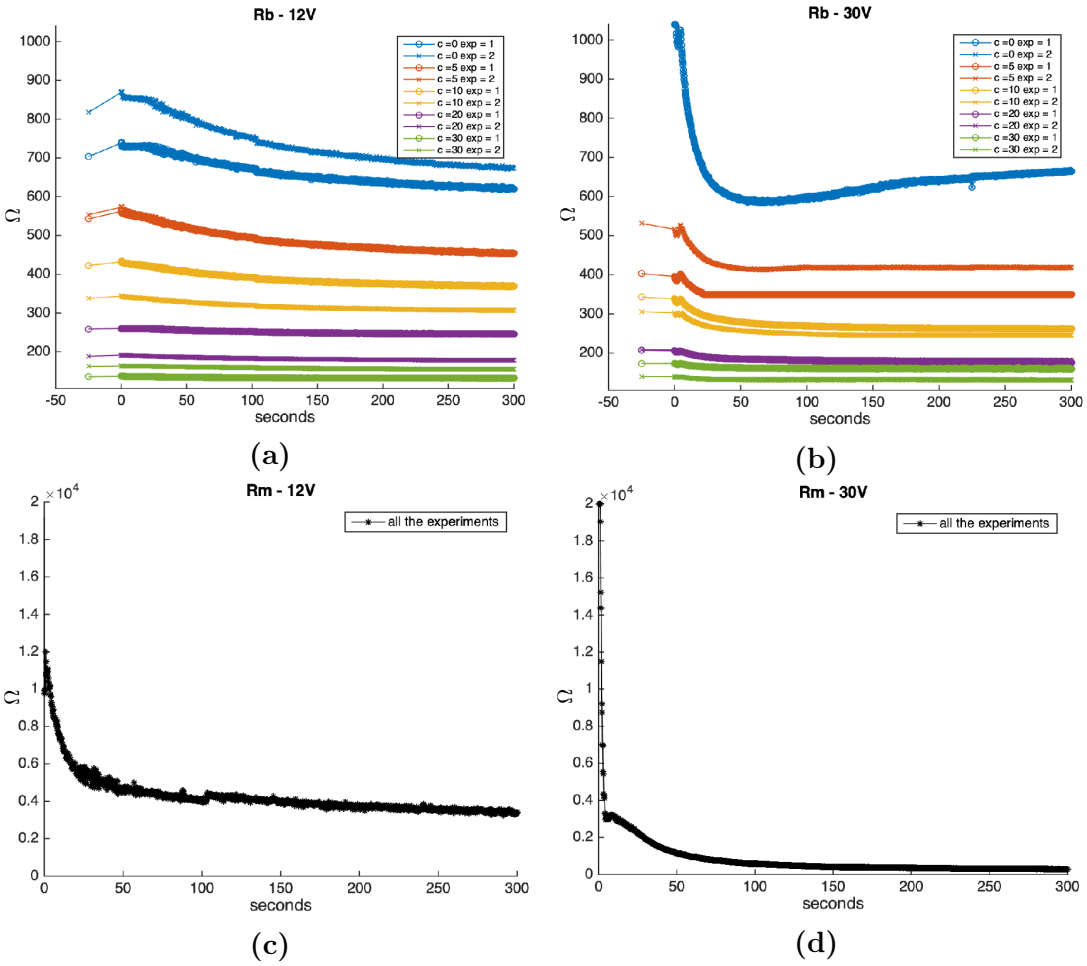

Figure 1.22 – Time evolution of the estimated values of R_b and R_m. In Figure 1.22a and Figure 1.22b, R_b decreases because the cells reject ions on the buffer during the electroporation. The values corresponding at the negative time are the estimated values obtained before pulse. At the same time, the decay of the membrane permeability produces a reduction of the resistance of the membrane R_m (Figure 1.22c and Figure 1.22d). We suppose that this decay is independent on the the buffer conductivity. The parameter variation are more pronounced for an higher pulse voltage.

1.7 Conclusion and perspectives

This chapter presented the work done to analyse, through an EC model, the EIS data resulting from an electroporation experiment performed on a cells monolayer.

In the first part, we have discussed the physical principle behind the topics of the chapter. In particular, we have focused on two impedance measurement techniques: the 2-electrode method and the 4-electrode method. For a given sample, we have proven that the two techniques achieve the same measure but that in a real-life experiment, there exist factors that bring to side effects. In fact, the EP causes some distortion in the 2-electrode measurement, which requires a readjustment. We have shown that this phenomenon is prevented by using the 4-electrode technique. Then, we have discussed the calibration of a 4-electrode measurement device through the three-reference calibration method. This calibration needs three samples of which both the actual responses to the current passage, *i.e.* the effective impedance Z_s, and the impedance measured by the device, Z_m, are known. To obtain the Z_m, three measurements are performed using the same device setup (*i.e.* the measurements differ from each one only by the sample) and, at the end of one measurement, the impedance of the whole sample is measured. Thanks to the three couples of Z_s and Z_m, it is possible to solve a 3×3 linear system whose unknowns are the calibration parameters A_1, A_2 and A_3. Then, for a given angular frequency ω, one can compute the unknown impedance of a new sample from the impedance measured by the device thanks to the calibration formula:

$$Z_s(\omega) = \frac{Z_m(\omega)A_1(\omega) + A_2(\omega)}{Z_m(\omega) + A_3(\omega)}.$$

In particular, we have emphasized the hypothesis necessary for a proper application of this method, stressing on the fact that what changes between the references is only the considered sample.

In the second part of this chapter, we have presented the EIS experiments performed by García-Sánchez et al. [20], and with the purpose to understand the cell membrane structural variations after the application of an electroporation pulse. We have described the arranged 4-electrode measurement system used during the experiments, the electroporation-measurement procedure and the resulting data. A considerable work has been done during this thesis to elaborate the data: we have produced a method and a relative code (consisting in a C++ library and Matlab scripts) capable of handling a large amount of data, differentiating the experiments by the presence of cells, the KCl concentration on the buffer, the voltage of the electroporation pulse and preserving the time evolution of the data.

We have learned that the free-cell impedance measurements could be used to calibrate the measurement system, applying the three-reference calibration method. We have then characterized the theoretical response of the buffer to the passage of an AC signal and we have used it, in combination with the free-cell measurements, to apply the three-reference calibration method. We have illustrated the limits of this calibration strategy when it is applied to our dataset. We have suggested that this is due to some imprecisions on the measurements – for example, the quantity of KCl dissolved in the buffer is different from the scheduled quantity – and on the fact that the hypothesis necessary to the application of this calibration method are

not respected. We have noticed that, in the considered experiments, the measured sample was only a part of the compound placed in the plate: this implies that changes between the references are not only due the sample but to the whole compound. Then, we have proposed to compensate the weakness of the observations by exploiting more than three references. The result is a new calibration strategy which is more stable and reliable and allows us to cast aside the provided calibrated observations and to produce our own.

In the last part, we have studied them by an EC model. First of all, we have designed the EC, which reflects the electrical properties of the two elements composing the sample: the buffer and the cells. In this way, we have determined the parameters which characterize the EC model: R_b, R_{cyt}, R_m, C_m and α_m. We have set the purpose to find the parameter values which allow to fit the calibrated observations in order to obtain a quantitative analysis of the electroporation phenomenon. The parameters estimation was a difficult step because of some non-identifiable parameters. This fact imposed a research more rigorous, based on strong hypothesis on the parameters resulting from physical analysis of the sample elements and a in-depth data review. This leads to assume that, contrary to R_b, the cells parameters (R_{cyt}, R_m, C_m, α_m) are independent on the buffer conductivity. Moreover, we have assumed also that R_{cyt}, C_m and α_m are constant over time. We have also assumed that R_m has infinity value before the pulse and then, after the pulse application, that it is of the same order of the other resistances. Thus, we have used the after pulse observations to study the time evolutions of R_b and R_m, allowing a limited freedom for the other parameters. During this step, it was fundamental to assume R_m independent on the buffer conductivity. The estimation shows interesting time evolutions: both R_b and R_m decrease progressively during the minutes after the pulse. Those are the exactly the behaviors expected from these two parameters to show the dynamics of the electroporation. Their values could even quantify the electroporation phenomenon.

During this work, we have produced an efficient strategy to analysis the data coming from a kind of EIS experiment devoted to the study of the electroporation phenomenon. As seen in this document, a weakness of this method consists in the calibration strategy: we would like to reinforce the method used to obtain more accurate calibrated data and in order to be able to use all the information available. However, the actual strategy is satisfactory and it could be interesting its application to the dataset presented in Section 1.4 that we have not treated during this work. Here, the challenge is that only one buffer conductivity has been tested, which means less information available to estimate the parameters, requiring a further analysis of the studied system and the resulting observations.

Chapter 2

Asymptotic analysis of the conductivity problem with high conductive thin passive electrodes

2.1 Introduction

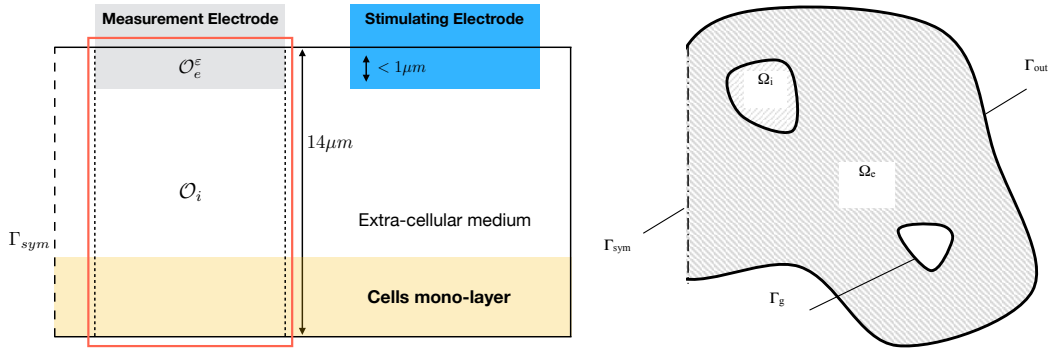

(a) Thin film electrode. **(b)** Volume electrode.

Figure 2.1 – Representations of two different 4-electrode systems: *in vitro* (left) and in a volume tissue (right) that lead to two *floating potential* problems

The electrical impedance Z – already defined in Chapter 1 – is the measure of the opposition that a system presents to a displacement of electric alternative current. The electrical impedance Z is defined as the ratio between the time-harmonic voltage U applied to the system and the electric current I:

$$Z = \frac{U}{I}.$$

Bioimpedance measurements give informations on the electrical properties of biological entities, from cells to tissue [5, 12, 32]. This technique is particularly interesting to investigate the cell response to electrical stress.

As seen in Chapter 1 unlike the standard 2-electrodes device that impose the electric stress and measure the response, bioimpedance measurements performed

with 4 electrodes (2 electrodes that impose the electric stress and 2 passive electrodes that measure the response of the sample) do not contain the measure distortion due to interfacial water in the vicinity of the active electrode [5, 20, 26].

An example of the 4-electrode system *in vitro* is presented in Chapter 1 and has been proposed by Garcia-Sachez *et al.* [20]. The system is composed of a buffer layer, an electrolyte with or without a cell mono-layer, on the bottom and of very thin electrodes placed on the top of the buffer (see Figur 2.1a). Another example of a 4-electrode system in a tissue as presented in Figure 2.1b has been used in [21,51] (see Appendix B for more details). In this case the passive electrodes are not thin.

Both active and inactive electrodes are not perfect conductor but, supposing intense enough electric field, we can represent the delivering electrodes as equipotential surface. Unlike the active electrodes on which either the potential or the current are imposed, which correspond to the Dirichlet or Neumann boundary conditions, for the inactive electrodes the value of the equipotential is an unknown of the partial differential equation. The main goal of this chapter is to present a mathematical analysis of the floating potential problem and to perform an asymptotic analysis to improve the accuracy of the approximation.

The first modeling approach consists in seeing the inactive electrode as a highly conductive medium. The electroquasistatic potential satisfies Poisson equation in each domain: the high conductive passive electrodes, and the biological sample, corresponding to the cell-buffer system or the biological tissue. In this problem, the ratio ξ between the conductivities of the biological tissue (or the buffer-cell system) and the electrode conductivity plays a crucial role. Since the large contrast between the conductivities, we have $\xi \ll 1$. When solving the problem using difference finite method, the presence of a small value could lead to an *ill-conditioned* matrix. In the case of an electrode which can be seen as a *thin film*, an other small parameter has to be taken into account: the ratio δ between the electrode thickness and the total domain size. A small δ means small space step in order to discretize the electrode: this brings to more instability and increases the computational cost.

To avoid the aforementioned difficulties, another approach consists in considering the measurement electrode as a perfect conductor. Then the passive electrode becomes an equipotential and the electric field vanishes in the electrode. In other words, the surface of the electrode is an equipotential and the total flux through this surface is zero, which is the so called *floating potential* [28]. The advantage of the *floating potential* approach is to avoid the large heterogeneity of the conductivity and to reduce the mesh size, since only the (lower) conductive biological sample is considered. A study of a *floating potential* problem is presented in Amann *et al.* [4], which propose a boundary element method to tackle the *floating potential* in the case shown in Figure 2.1b, where $\delta \sim 1$ and $\xi \ll 1$. They also consider an asymptotic regime for which the *floating potential* gives better approximation than the full problem.

In this chapter, we focus on the problem with *thin film* electrode, *i.e.* $\xi \ll \delta \ll 1$. We propose an asymptotic analysis to exhibit the full problem of which *floating potential* is the first order approximation. In addition, we characterize the floating potential thanks to appropriate Dirichet to Neumann maps, which makes it possible to use standard Finite Element Method (FEM) or Finite Difference Method (FDM) codes to tackle the *floating potential* problem. This also makes it

possible to prove that *floating potential* problem is well-posed. The analysis of the case with volume electrode, $\xi \ll 1,\ \delta \sim 1$ is discussed in Appendix B.

The chapter is structured as follows. In Section 2.2 the asymptotic regime assumptions and the problem are presented. Section 2.2 also investigate the numerical peculiarities of the electrostatic problem with very conductive and passive electrodes. The goal of this section is to point up the highlights and the weaknesses of both strategies: direct resolution of the statement problem and *floating potential* approach. Section 2.3 treats of the asymptotic expansion of the electric potential and of the proof of the convergence of the expansion. Section 2.4 exposes the conclusions and the perspectives of our work.

2.2 Modeling Approaches

Problem Statement

In this section, we present the problem in the case of a *thin electrode*. To avoid singularities that complexify the asymptotic expansion, we consider a *toy model* which contains the main asymptotic properties of the problem deprived from the singularities. More precisely the domain is composed of an inner conducting domain, representing the buffer, surrounding by a thin highly conducting sheet, representing the measurement electrode. We denoted by Ω_i the inner domain

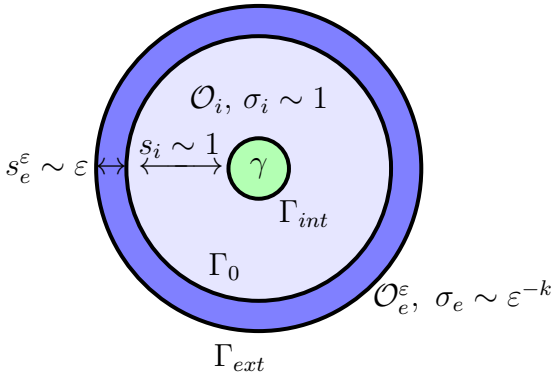

Figure 2.2 – Scheme of the *toy model*: the buffer domain is embedded in the electrode domain.

corresponding to the sample with a smooth boundary $\partial\Omega_i$. Let Ω_e^ε be a thin layer with constant thickness surrounding Ω_i. The ratio between the sizes of the two domains is order ε. The inner domain Ω_i contains a hole corresponding to the source coming from the stimulating electrode. Let Γ_{int} be the inner boundary of Ω_i, Γ_0 the interface between Ω_i and Ω_e^ε, Γ_{ext} the exterior boundary of Ω_e^ε. Figure 2.2 illustrates these notations. Let be $\Omega = \overline{\Omega_i} \cup \Omega_e^\varepsilon$ and assume that Γ_0 is a 2D smooth compact domain. The electric potential u_ε in Ω is the solution to the following problem

$$\begin{cases} -\nabla \cdot (\sigma^\varepsilon \nabla u_\varepsilon) = f \quad \text{in} \quad \Omega, \\ \partial_n u_{\varepsilon|\Gamma_{ext}} = 0, \\ u_{\varepsilon|\Gamma_{int}} = \gamma, \end{cases} \tag{2.1}$$

where $f \equiv 0$ in $\overline{\Omega_e^\varepsilon}$, $f \in L^2(\Omega_i)$, $supp(f) \subsetneq \Omega_i$ for the sake of simplicity, $\gamma \in H^{\frac{1}{2}}(\Gamma_{int})$. The conductivity σ is given by

$$\sigma^\varepsilon(x) = \begin{cases} \sigma_i(x), & \text{if} \quad x \in \Omega_i, \\ \varepsilon^{-k}\sigma_e, & \text{if} \quad x \in \Omega_e^\varepsilon = \Omega \setminus \overline{\Omega_i}, \end{cases} \tag{2.2}$$

with $k \geq 1$. We suppose that σ_i is a positive function in Ω_i whereas σ_e is a positive constant in Ω_e^ε. As Ω_i represents a dielectric and Ω_e^ε a conductor, we have $\sigma_i \ll \varepsilon^{-k}\sigma_e$. From this, we obtain the following *transmission conditions*

$$\begin{cases} u_{\varepsilon|\Gamma_0{}^i} = u_{\varepsilon|\Gamma_0{}^e}, \\ \sigma_i\, \partial_n u_{\varepsilon|\Gamma_0{}^i} = \varepsilon^{-k}\sigma_e\, \partial_n u_{\varepsilon|\Gamma_0{}^e}. \end{cases} \tag{2.3}$$

Under this hypothesis System (2.1-2.3) has a unique solution $u_\varepsilon \in H^1(\Omega)$. See [41] for more details.
The only parameter of the model is k. The parameter k sets the growth rate of the exterior conductivity $\varepsilon^{-k}\sigma_e$ when ε tends to zero. In other words k links the conductivities ratio and the domain sizes ratio. The limit model depends on the different values of k. The ideal case of perfect conductor is achieved when ε approaches zero with $k = 2$. In the next section, a numerical example is given to explain the specificities and the numerical complexities of the asymptotic regime $k = 2$.

Numerical assessment

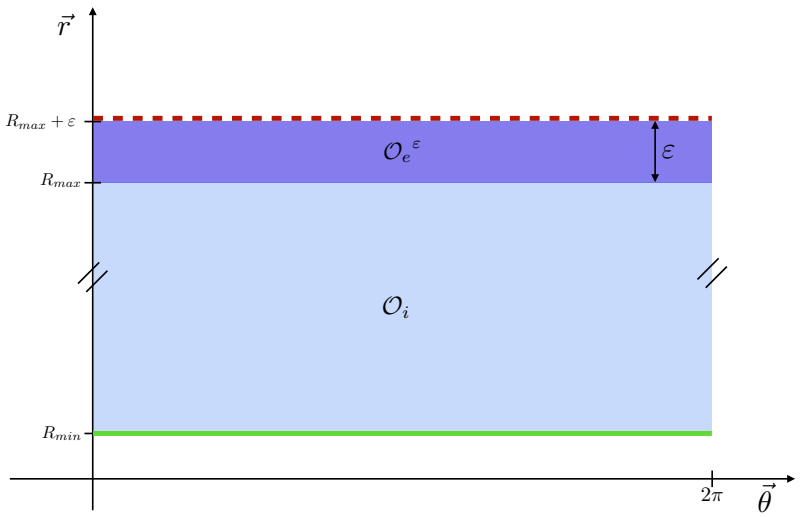

Figure 2.3 – 2D Polar Domain

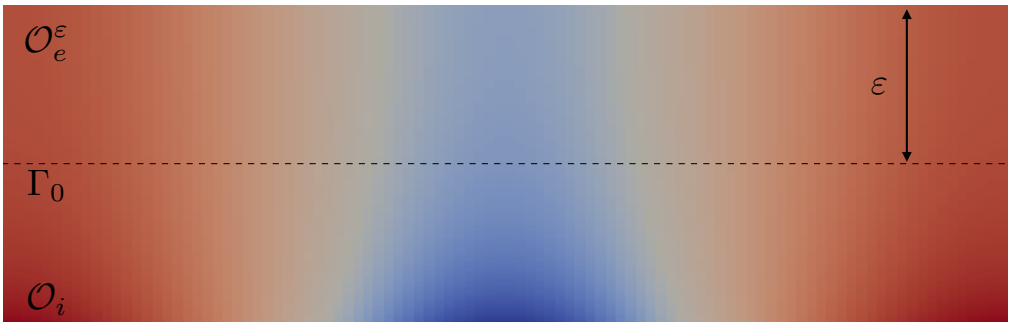

(a) $\varepsilon = 1$

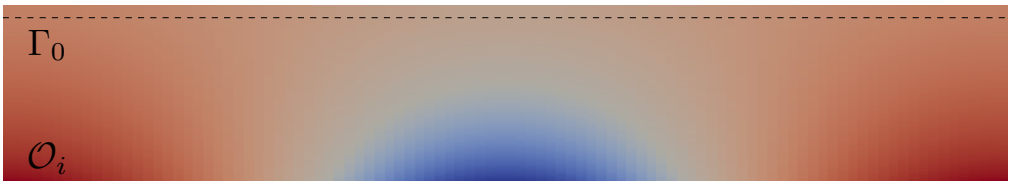

(b) $\varepsilon = 0.1$

Figure 2.4 – Numerical solution of System (2.1-2.3) with two different values for ε: $\varepsilon = 1$ and $\varepsilon = 0.1$. One can remark that when ε tends to zero the electric potential in the domani $\mathcal{O}_e^\varepsilon$ becomes homogeneous.

A C++ FDM library (around 3200 code lines) has been implemented in order to numerically solve System (2.1-2.3). In this section, the difficulties of the direct numerical resolution of System (2.1-2.3) are presented.

We use a representation of the original system where the choice of the domain and the boundary conditions are imposed in order to create a problem for which we know the exact solution. In this way, the numerical solution can be compared with the exact solution. Considering the geometry presented in Figure 2.2, in this *toy problem* the inner domain Ω_i is an annulus centered in the origin and with smaller radius R_{min} and greater radius R_{max}, such that $R_{max} - R_{min} = 1$. The outer domain ${\Omega_e}^\varepsilon$ is an annulus surrounding Ω_i and with thickness ε. To represent the system on a 2D Cartesian grid, all the equations have been rewritten in polar coordinates. The discretization of the interface Γ_0 is part of the employed mesh. Figure 2.3 shows the domain in polar coordinates. In the exterior boundary Γ_{ext}, that in this example corresponds to the set of points such that $r = R_{max} + \varepsilon$, Neumann homogeneous condition are imposed since there is no electrical flow coming outside from the system. On the other hand, on the interior boundary Γ_{int}, that in this example corresponds to the set of points such that $r = R_{min}$, Dirichlet conditions are imposed to simulate the flow of electric current given by the pulse of the active

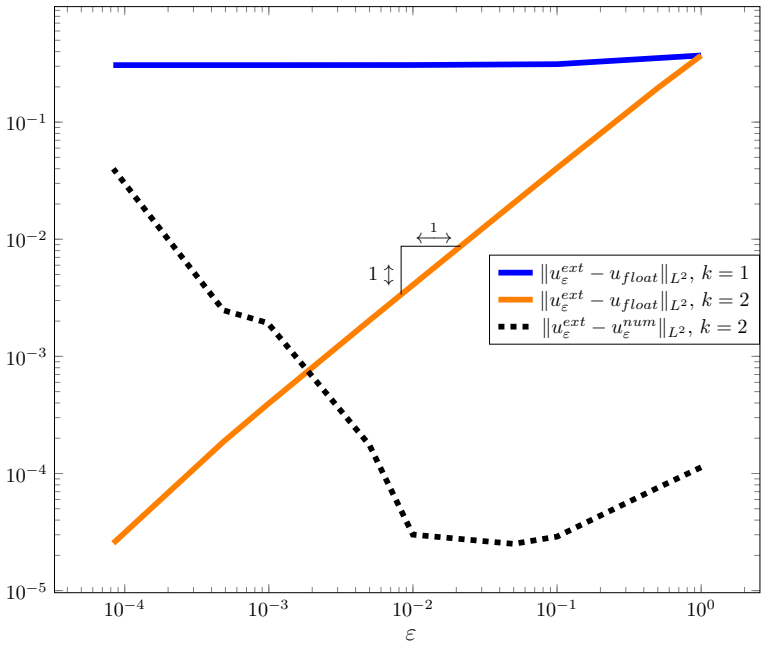

Figure 2.5 – $k = 1$: when ε tends to zero, the exact solution does not converge to the *floating potential approach* solution. $k = 2$: the exact solution converges to the *floating potential approach* approximation when ε tends to zero. Due a high *condition number* of the matrix, a direct resolution gives a worse approximation for smaller ε.

electrode. The model to solve is

$$\begin{cases} -\left(\dfrac{\partial^2 u_\varepsilon}{\partial r^2} + \dfrac{1}{r}\dfrac{\partial u_\varepsilon}{\partial r} + \dfrac{1}{r^2}\dfrac{\partial^2 u_\varepsilon}{\partial \theta^2}\right) = 0 & \text{in} \\ &]\,0; 2\pi[\times]R_{min}; R_{max}\,[\,\cup\,]0; 2\pi[\times]R_{max}; R_{max} + \varepsilon\,[, \\ \partial_r u_{\varepsilon|r=R_{max}+\varepsilon} = 0, \\ u_{\varepsilon|r=R_{min}} = e^{i\theta} + 1, \\ u_{\varepsilon|\theta=0} = u_{\varepsilon|\theta=2\pi}, \end{cases} \tag{2.4}$$

with the transmission conditions

$$\begin{cases} u_{\varepsilon|r=R_{max}^-} &= u_{\varepsilon|r=R_{max}^+}, \\ \sigma_i \partial_r u_{\varepsilon|r=R_{max}^-} &= \varepsilon^{-k}\sigma_e\, \partial_r u_{\varepsilon|r=R_{max}^+}, \end{cases} \tag{2.5}$$

where $k \geq 1$ and

$$\sigma(r,\theta) = \begin{cases} \sigma_i \in \mathbb{R}, & \text{if} \quad (r,\theta) \in]\,0; 2\pi[\times]R_{min}; R_{max}\,[, \\ \varepsilon^{-k}\sigma_e \in \mathbb{R}, & \text{if} \quad (r,\theta) \in]0; 2\pi[\times]R_{max}; R_{max} + \varepsilon\,[. \end{cases}$$

The numerical solution is computed for several values of the parameter k for which different behaviours of the solution are achieved. We found that for $k = 2$ in Ω_e^ε the electrical potential becomes homogeneous when ε tends zero. We will see later that this is not the case with $k = 1$ (for more details see Appendix A.1). Figure 2.4 shows simulations corresponding to the numerical solution of System (2.1 - 2.3) with $k = 2$ for $\varepsilon = 1$, on top, and $\varepsilon = 0.1$, on bottom.

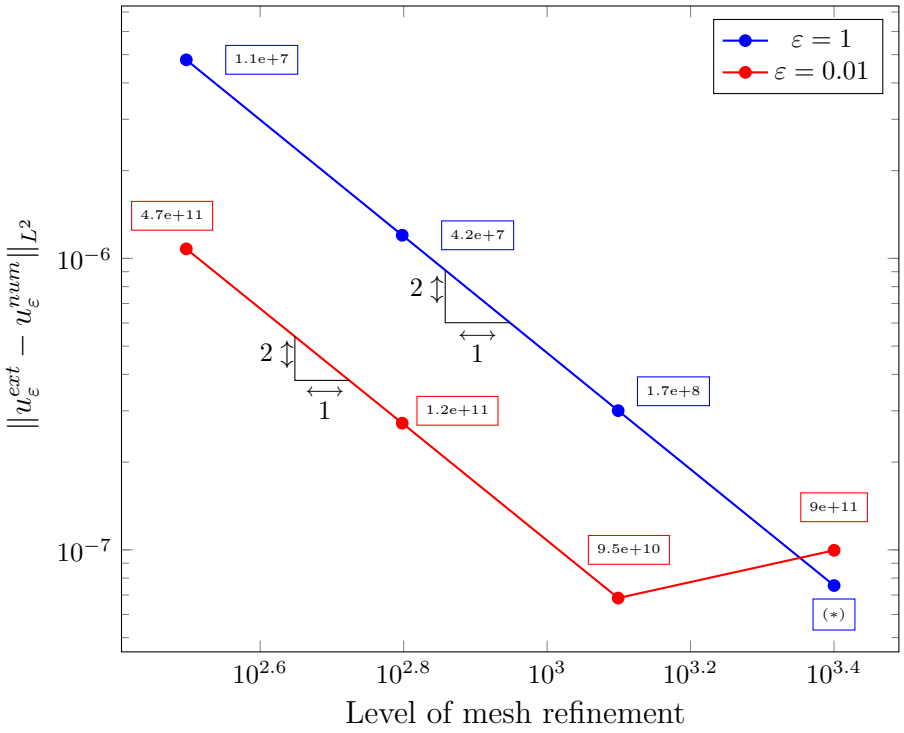

Figure 2.6 – The blue line shows that the distance between the exact and the numerical solution with $\varepsilon = 1$ tends to zero for smaller discretization steps at the second order. The red line is for $\varepsilon = 0.01$. $(d\theta, dr) \in \{(314, 200), (628, 400), (1256, 800), (2512, 1600)\}$. Condition number of the matrix of System (2.4-2.5) grows considerably when ε approaches zero. With small discretization steps the instability increases and the numerical solution has lower accuracy. $(*)$ value not available due to not reasonable computational cost to compute it.

One possibility to obtain a good approximation of a physical system consists in considering a small value of ε with respect to the domain Ω_i. This brings to two possibilities: a very small discretization step in both directions or two discretization steps with different magnitude order. In both case an increase of the computational cost, specially in the first case, and the instability, specially in the second case, is noted. Several simulations with different values of ε are performed. We compare the exact solution u_ε^{ext} of System (2.4-2.5) with the numerical solution u_ε^{num} obtained by a difference finite method where all the equations are discretized at the second order approximation. The discretization steps are $d\theta = 0.063$ and $dr = 1.7 \times 10^{-5}$: dr is chosen in order to discretize the domain Ω_e^ε in case of a small electrode thickness ($\varepsilon = 10^{-4}$) and a bigger $d\theta$ is taken to reduce the computational cost. Results are given in Figure 2.5. The dashed black curve represents the L^2-norm of the difference between u_ε^{ext} and u_ε^{num}: the difference finite method gives a solution getting worse for smaller ε. The reason of bad approximation lies in the fact that a small value of ε leads also to more instability in the problem since it increases the condition number of the matrix, by the presence of small values in the *transmission conditions*. Several simulations have been performed with ε fixed and

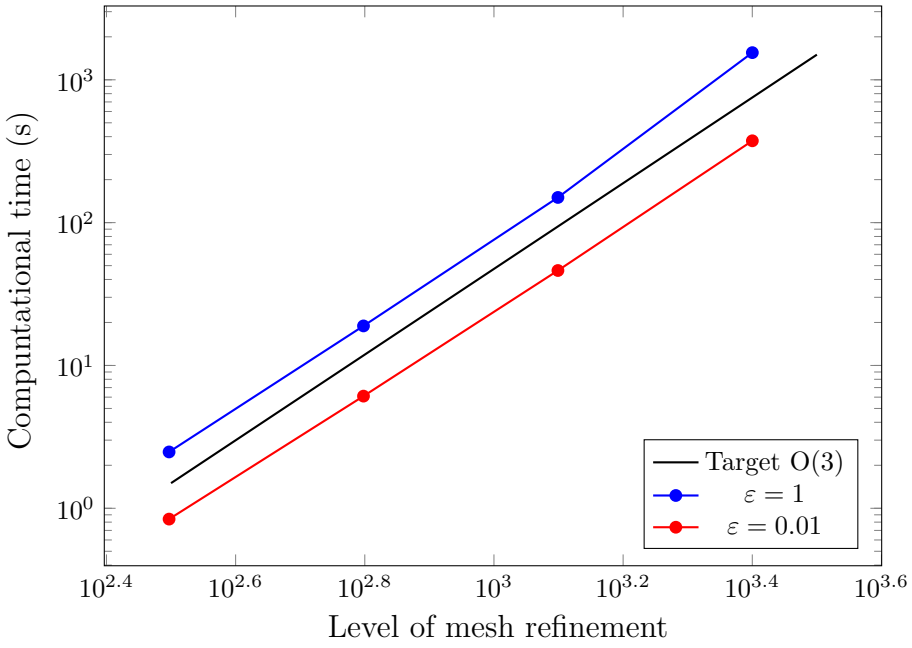

Figure 2.7 – Computational time for $(d\theta, dr) = (2^k \times 314, 2^k \times 200), k = 0, \cdots 3$. The computational time increases exponentially with the number of discretization points.

changing the discretization steps in both directions, see Figure 2.6. The relative distance between the exact solution and the numerical solution is computed by using the L^2-norm. One can remark that fixing a big ε (for example when internal domain Ω_i and external domain Ω_e^ε have the same thickness) and increasing the number of the discretization points, the numerical solution gives an approximation of the exact solution at the second order accuracy, as expected from the choice of the numerical approximations. For smaller ε the problem becomes *ill-conditioned*, that is why for smaller discretization steps the numerical solution diverges from the exact solution as shown by the dashed line in Figure 2.5. A way to reduce the instability in the problem could be to consider more homogeneous discretization steps but this requires not reasonable computational cost. Figure 2.7 shows how the computational time increases exponentially with shorter discretization steps. The simulations are performed by using an ordinary laptop (a MacBook Pro with processor 3,3 GHz Intel Core i7).

In conclusion, it possible to reproduce the behaviour of the electric potential in a electrode using System (2.1-2.3). Nevertheless it is hard to obtain a good approximation since the direct resolution of this problem requires a high computational cost and/or to solve an ill-conditioned problem. That is why in this work we focus on a alternative method. A way to avoid this is to consider the limit problem obtained when ε tends to zero. In this case the electrode is part of the boundary of the domain Ω_i. The goal is then to determinate the electrode boundary condition. This leads to the *floating potential approach*. Next section focuses on this approach.

The *floating potential* approach

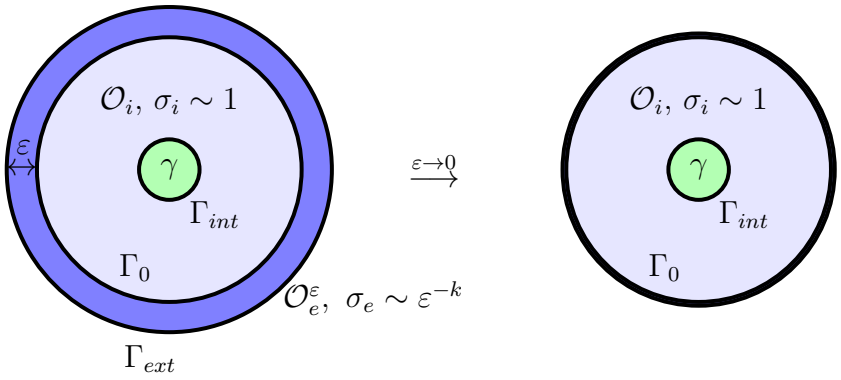

Figure 2.8 – Scheme of the buffer domain embedded in the electrode domain.

As seen in Section 2.2, the direct resolution of the electric potential diffusion between two domains with both large conductivities and sizes contrasts requires high computational resources and leads to numerically *ill-conditioned* matrix. In order to avoid these difficulties, we propose to perform an asymptotic expansion when the electrode thickness ε tends to zero, see Figure 2.8. The simulation domain is then restricted to the domain Ω_i, whose boundary is an equipotential surface. The problem to solve reads then as follows:

$$\text{Find } (u_0, \alpha_0) \in H^1(\Omega_i) \times \mathbb{R} \text{ such that } \begin{cases} -\nabla \cdot (\sigma_i \nabla u_0) = f \quad \text{in } \Omega_i, \\ u_{0|_{\Gamma_0}} = \alpha_0, \\ \displaystyle\int_{\Gamma_0} \sigma_i \partial_n u_0 \, ds = 0, \\ u_{0|_{\Gamma_{int}}} = \gamma. \end{cases} \tag{2.6}$$

with $f \in L^2(\Omega_i)$, $\gamma \in H^{\frac{1}{2}}(\Gamma_{int})$ and σ_i positive function of Ω_i and where n is the outer normal vector of Γ_0. Under these hypotheses, there exists a unique solution of Problem (2.6).

Existence and Uniqueness of *floating potential* problem

In order to prove the existence and uniqueness of System (2.6), we consider the following *Dirichlet-to-Neumann operators*

$$\Lambda_0 : H^{\frac{1}{2}}(\Gamma_{int}) \longrightarrow H^{-\frac{1}{2}}(\Gamma_0)$$
$$\gamma_{int} \overset{\Lambda_0}{\longmapsto} \partial_n v_{|_{\Gamma_0}} \quad \text{s. t.} \quad \begin{cases} -\nabla \cdot (\sigma_i \nabla v) = f \quad \text{in } \Omega_i, \\ v_{|_{\Gamma_0}} = 0, \quad v_{|_{\Gamma_{int}}} = \gamma_{int}; \end{cases} \tag{2.7}$$

$$\Lambda_1 : H^{\frac{1}{2}}(\Gamma_0) \longrightarrow H^{-\frac{1}{2}}(\Gamma_0)$$
$$\gamma_0 \overset{\Lambda_1}{\longmapsto} \partial_n w_{|_{\Gamma_0}} \quad \text{s. t.} \quad \begin{cases} -\nabla \cdot (\sigma_i \nabla w) = 0 \quad \text{in } \Omega_i, \\ w_{|_{\Gamma_0}} = \gamma_0, \quad w_{|_{\Gamma_{int}}} = 0; \end{cases} \tag{2.8}$$

Now considering u_0 solution of System (2.6), it is easy to get

$$\partial_n u_{0|\Gamma_0} = \Lambda_1(\alpha_0) + \Lambda_0(\gamma).$$

From System (2.6), we obtain

$$\int_{\Gamma_0} \sigma_i \partial_n u_0 \, ds = 0,$$

then we have

$$\int_{\Gamma_0} \sigma_i \left(\Lambda_1(\alpha_0) + \Lambda_0(\gamma)\right) \, ds = 0.$$

As Λ_0 and Λ_1 are linear operator, $\alpha_0 \in \mathbb{R}$ and since [1] $\int_{\Gamma_0} \sigma_i \Lambda_1(1) ds \neq 0$, it is possible to write an explicit formula for α_0

$$\alpha_0 = -\frac{\displaystyle\int_{\Gamma_0} \sigma_i \Lambda_0(\gamma) \, ds}{\displaystyle\int_{\Gamma_0} \sigma_i \Lambda_1(1) \, ds}. \tag{2.9}$$

Equation (2.9) allows us to compute the value of the constant α_0 using only the solutions of Dirichlet problems for which, as it is known in the literature [41], the existence and uniqueness of a solution are proven. Then the constant α_0 is uniquely determined by Equation (2.9). Once computed α_0, System (2.6) becomes a Dirichlet problem that admits one and only one solution $u_0 \in H^1(\Omega_i)$. Then this proves that there exists a unique couple $(u_0, \alpha_0) \in H^1(\Omega_i) \times \mathbb{R}$ solution of System (2.6).

Remark 8. *In Chapter 3, the case of multiple passive electrodes is considered. The same approach leads to the well-posedness: the floating potential of each passive electrode is obtained thanks to an invertible Gram matrix (see Proposition 7).*

Floating potential problem assessment

As in Section 2.2, we solve System (2.6) in the case where the domain Ω_i is an annulus centered in the origin and with smaller radius R_{min} and greater radius R_{max}, such that $R_{max} - R_{min} = 1$. To represent the system on a 2D Cartesian grid, all the equations are rewritten in polar coordinates. Figure 2.9 shows the domain in polar coordinates. Furthermore, we suppose that the conductivity σ_i is constant

1. Denoting by w the solution to Problem (2.8) with $\gamma_0 = 1$, one has

$$\int_{\Gamma_0} \sigma_i \Lambda_1(1) \, ds = \int_{\Gamma_0} \sigma_i \partial_n w \, w \, ds = \int_{\Omega_i} \sigma_i \nabla w \nabla w \, dx \neq 0.$$

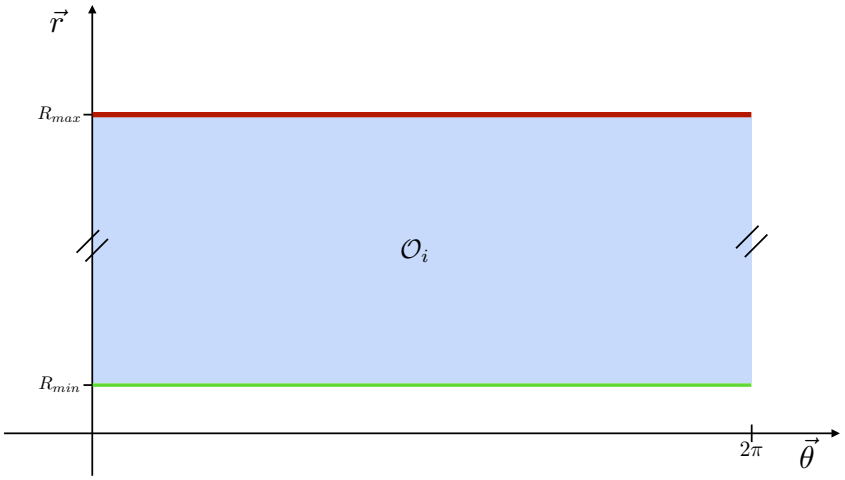

Figure 2.9 – 2D Polar Domain with $\varepsilon = 0$

in the domain Ω_i. System (2.6) can be rewritten as follows

$$\begin{cases} -\sigma_i \left(\dfrac{\partial^2 u_0}{\partial r^2} + \dfrac{1}{r}\dfrac{\partial u_0}{\partial r} + \dfrac{1}{r^2}\dfrac{\partial^2 u_0}{\partial \theta^2} \right) = f(\theta, r) \quad \text{in} \quad]\,0; 2\pi[\times]R_{min}; R_{max}\,[, \\ u_{0|r=R_{max}} = \alpha_0, \\ u_{0|r=R_{min}} = \gamma, \\ u_{0|\theta=0} = u_{0|\theta=2\pi}, \end{cases} \tag{2.10}$$

The proof of the existence and the uniqueness of System (2.6) given in Section 2.2 directly provides a way to approximate the solutions by following these computational steps:

— compute α_0,
— solve the Laplace problem with Dirichlet conditions.

The value of α_0 is given by

$$\alpha_0 = -\frac{\displaystyle\int_0^{2\pi} \partial_r v_{0|r=R_{max}} d\theta}{\displaystyle\int_0^{2\pi} \partial_r v_{1|r=R_{max}} d\theta},$$

where v_0 and v_1 are respectively solution of the following problems:

$$\begin{cases} -\sigma_i \left(\dfrac{\partial^2 v_0}{\partial r^2} + \dfrac{1}{r}\dfrac{\partial v_0}{\partial r} + \dfrac{1}{r^2}\dfrac{\partial^2 v_0}{\partial \theta^2} \right) = f \quad \text{in} \quad]\,0; 2\pi[\times]R_{min}; R_{max}\,[, \\ v_{0|r=R_{max}} = 0, \quad v_{0|r=R_{min}} = \gamma, \\ v_{0|\theta=0} = v_{0|\theta=2\pi}, \end{cases}$$

$$\begin{cases} -\sigma_i \left(\dfrac{\partial^2 v_1}{\partial r^2} + \dfrac{1}{r}\dfrac{\partial v_1}{\partial r} + \dfrac{1}{r^2}\dfrac{\partial^2 v_1}{\partial \theta^2} \right) = 0 \quad \text{in} \quad]\,0; 2\pi[\times]R_{min}; R_{max}\,[, \\ v_{1|r=R_{max}} = 1, \quad v_{1|r=R_{min}} = 0, \\ v_{1|\theta=0} = v_{1|\theta=2\pi}. \end{cases}$$

Numerical solution	ε	Numb. mesh point	$\|err\|_{L^2}$	comp. time
u_ε^{ext}	0.0005	300×15000	$2.3e^{-4}$	170s
u_{float}	0.0005	100×6000	$1.2e^{-4}$	16s

Table 2.1 – A direct resolution of the two domains problem requires a refiner mesh in order to discretize the thin electrode. Using the *floating potential* problem a coarser mesh is allowed. The results are a lower error, since the discretizzation steps are more homogeneous, and a decrease of the computational cost.

This means that to find u_0, the resolution of three Dirichlet problems is required. Using a difference finite method, one can remark that the matrix is the same for the three problems. That means that a not-time consuming method can be implemented and applied.

Supposing: $R_{min} = 1$, $R_{max} = 2$, $f \equiv 0$ and $\gamma = e^{i\theta} + 1 \ \forall \theta \in [0, 2\pi]$, $\sigma_i = 0.1$, $\sigma_e = 1$ and using the mesh introduced in Section 2.2 limited to the domain Ω_i, one can compare the exact solution u_ε^{ext} of System (2.4-2.5) with the numerical solution u_{float} of the *floating potential* problem (2.10). Results are given in Figure 2.5. For $k = 1$, as we know, the two domains problem does not reach the assumption of an equipotential conductor when ε tends to zero. That is why there is a great distance between u_ε^{ext} and u_{float} for $k = 1$ (blue line). Differently, for $k = 2$, the solution of the solution of (2.4-2.5) converges to the solution of the *floating potential* problem (2.10) when ε tends to zero (orange line).

We conclude by saying that modeling the system by the *floating potential* approach leads to a stable and more accurate solution, respect to the solution of the two domains problem. Furthermore, the *floating potential* problem requires a coarser mesh discretizing only one domain. This implies an important decrease of the computational time. An example is given in Table 2.1.

2.3 Theoretical Study of *floating potential approach*

In Section 2.2, the convergence of the solution of the two domains problem (2.1-2.3) to the solution of the floating potential (2.6) has been demonstrated numerically when ε tends to zero. In this section we prove the convergence theoretically. We use similar hypothesis on the two domains problem (2.1-2.3), and we assume that the source terms f and γ are as regular as needed. We call ξ the ratio between low and high conductivities and δ the ratio between the electrode thickness and buffer domain size. According to Equation (2.2), the relation between conductivities and dimensions is given by $\delta = \varepsilon$ and $\xi = \varepsilon^k$, with ε a small parameter. An asymptotic expansion of the solution of the two domains problem (2.1-2.3) is considered based on the small value ε:

$$u_0 + u_1\varepsilon + u_2\varepsilon^2 + \dots .$$

It is proved that the zero order solution of the asymptotic development coincides with the case where inactive electrode is considered as plate perfect conductor.

We refine the accuracy of the solution computing a first order correction. It is shown that the same strategy used for the resolution of System (2.6) is employed to compute the zero and the first order coefficients.

Geometric preliminaries

First we have to analyse some geometric aspects of the domain in order to describe how the geometry and the equations evolve in the limit case when ε tends to 0. The geometric preliminaries are presented in 3D even if in what follows, the asymptotic analysis is done in 2D. Obviously, the full analysis is valid in 3D.
Let be $x_T = (\xi_1, \xi_2)$ a system of local coordinates on $\Gamma_0 = \{\psi(x_T)\}$. We define the following map Φ by

$$\Phi(x_T, \xi_3) = \psi(x_T) + \xi_3 \vec{n}(x_T) \quad \forall (x_T, \xi_3) \in \Gamma_0 \times \mathbb{R},$$

where $\vec{n}$ is the outer normal vector of Γ_0. The layer Ω_e^ε is parameterized by

$$\Omega_e^\varepsilon = \{\Phi(x_T, \xi_3) \mid (x_T, \xi_3) \in \Gamma_0 \times (0, \varepsilon)\}.$$

Considering the Euclidean metric in (x_T, ξ_3), the coefficients of metric tensor $(g_{ij})_{i\,j=1,2,3}$ with $g_{ij} = \langle \partial_i \Phi, \partial_j \Phi \rangle$ have the form [38]

$$\begin{aligned} &g_{33} = 1, \quad g_{\alpha,3} = g_{3,\alpha} = 0 \quad \forall \alpha \in \{1,2\}, \\ &g_{\alpha,\beta}(x_T, \xi_3) = g^0_{\alpha,\beta}(x_T) + 2\,\xi_3\, b_{\alpha,\beta}(x_T, \xi_3) + {\xi_3}^2\, c_{\alpha,\beta}(x_T, \xi_3 \quad \forall \alpha, \beta \in \{1,2\}^2, \end{aligned}$$

where

$$g^0_{\alpha,\beta} = \langle \partial_\alpha \psi, \partial_\beta \psi \rangle,\ b_{\alpha,\beta} = \langle \partial_\alpha \vec{n}, \partial_\beta \psi \rangle,\ c_{\alpha,\beta} = \langle \partial_\alpha \vec{n}, \partial_\beta \vec{n} \rangle.$$

The Laplace-Beltrami operator deriving from this system of local coordinates of Ω_e^ε is given by

$$\Delta_g = \frac{1}{\sqrt{g}} \sum_{i,j=1,2,3} \partial_i (\sqrt{g} g^{ij} \partial_j),$$

where $(g^{ij}) = (g_{ij})^{-1}$ and g the absolute value of the tensor metric determinant.
It is possible to define, $\forall l \in \mathbb{N}$,

$$\begin{aligned} a^l_{i,j} &= \partial_3^l \left(\frac{\partial_i(\sqrt{g}\, g^{ij})}{\sqrt{g}} \right)\Big|_{\xi_3=0}, \qquad \forall (i,j) \in \{1,2,3\}^2, \\ A^l_{\alpha,\beta} &= \partial_3^l \left(g^{\alpha\,\beta} \right)\big|_{\xi_3=0}, \qquad \forall (\alpha,\beta) \in \{1,2\}^2, \end{aligned}$$

and the differential operator on Γ_0 of order 2

$$S^l_{\Gamma_0} = \sum_{\alpha,\beta=1,2} a^l_{\alpha,\beta} \partial_\beta + A^l_{\alpha,\beta} \partial_\alpha \partial_\beta.$$

Remark 9. *As shown in [38], the operator $S^0_{\Gamma_0}$ is the Laplace-Beltrami operator computed on the surface Γ_0. Let denote it with Δ_{Γ_0}*

$$S^0_{\Gamma_0} = \Delta_{\Gamma_0}.$$

The Laplace-Beltrami operator can be rewritten as

$$\Delta_g = \partial_3^2 + \sum_{l\geq 0} \frac{\xi_3^l}{l!}(a_{33}^l \partial_3 + S_{\Gamma_0}^l) \quad \forall (x_T, \xi_3) \in \Gamma \times (0, \varepsilon).$$

Performing the change of variable $\eta = \xi_3/\varepsilon$, we obtain

$$\Delta_g = \frac{1}{\varepsilon^2}\partial_\eta^2 + \frac{1}{\varepsilon} a_{33}^0 \, \partial_\eta + \sum_{l\geq 0} \varepsilon^l \frac{\eta^l}{l!} \left(\frac{\eta}{l+1} a_{33}^{l+1} \partial_\eta + S_{\Gamma_0}^l \right) \quad \forall (x_T, \xi_3) \in \Gamma_0 \times (0, 1),$$

and

$$\partial_n = \frac{1}{\varepsilon}\partial_\eta.$$

Limit Problems

The *toy model* presented in Section 2.2 is considered. Assuming that u^ε as

$$u^\varepsilon(x) = \begin{cases} u_i^\varepsilon \text{ in } \Omega_i, \\ u_e^\varepsilon \text{ in } \Omega_e^\varepsilon, \end{cases}$$

it is possible to rewrite System (2.1-2.3) in the following form

$$\begin{cases} -\nabla \cdot (\sigma_i \nabla u_i^\varepsilon) = f \quad \text{on } \Omega_i, \\ \Delta_g u_e^\varepsilon = 0 \quad \text{on } \Gamma_0 \times (0,1), \\ u_{i|_{\Gamma_0}}^\varepsilon = u_{e|_{\eta=0}}^\varepsilon, \\ \sigma_i \, \partial_n u_{i|_{\Gamma_0}}^\varepsilon = \varepsilon^{-(k+1)} \sigma_e \, \partial_\eta u_{e|_{\eta=0}}^\varepsilon, \\ \partial_\eta u_{e|_{\eta=1}}^\varepsilon = 0, \\ u_{i|_{\Gamma_{int}}}^\varepsilon = \gamma. \end{cases} \tag{2.11}$$

In System (2.11), the equations are separated respect to the domain there they are involved. This is useful when we apply an asymptotic analysis to see how the equations evolve when ε tends to zero.

In order to approach the problem by an asymptotic analysis in the case $k = 2$, let suppose that the solution of System (2.11) has the form of a power series of ε

$$u^\varepsilon(x) = \begin{cases} u_0^i + \varepsilon \, u_1^i + \varepsilon^2 u_2^i + \dots \\ u_0^e + \varepsilon \, u_1^e + \varepsilon^2 u_2^e + \dots \end{cases}, \tag{2.12}$$

By replacing the solution (2.12) in System (2.11), one can identify the terms with the same power of ε, getting the so called **p-th order problem**:

$$\begin{cases} -\nabla \cdot \left(\sigma_i \nabla u_p^i\right) = \delta_p f \quad \text{in } \Omega_i, \\ \partial_\eta^2 u_p^e = -a_{33}^0 \partial_\eta u_{p-1}^e - \sum_{l=0}^{p-2} \frac{\eta^l}{l!} \left(\frac{\eta}{l+1} a_{33}^{l+1} \partial_\eta u_{p-2-l}^e + S_{\Gamma_0}^l u_{p-2-l}^e \right) \text{ in } \Gamma_0 \times (0,1), \\ u_{p|_{\Gamma_0}}^i = u_{p|_{\eta=0}}^e, \\ \sigma_i \, \partial_n u_{p-3|_{\Gamma_0}}^i = \sigma_e \, \partial_\eta u_{p|_{\eta=0}}^e, \\ \partial_\eta u_{p|_{\eta=1}}^e = 0, \\ u_{p|_{\Gamma_{int}}}^i = \delta_p \gamma. \end{cases} \tag{2.13}$$

where

$$\delta_p = \begin{cases} 1 & \text{if } p = 0, \\ 0 & \text{otherwise.} \end{cases}$$

As we will see in what follows, to determine u_p^i, we use p-th, $p+1$-th and $p+2$-th order problems. From this, we can determine the problem satisfied by each single coefficient of the expansion.
In this section, we present a first order solution in the internal domain Ω_i. That is why we have to consider at least the 3 first order problems. The 0 order problem is:

$$\begin{cases} -\nabla \cdot (\sigma_i \nabla u_0^i) = f \quad \text{in } \Omega_i, \\ \partial_\eta^2 u_0^e = 0 \quad \text{in } \Gamma_0 \times (0,1), \\ u_0^i|_{\Gamma_0} = u_0^e|_{\eta=0}, \\ \partial_\eta u_0^e|_{\eta=0} = 0, \\ \partial_\eta u_0^e|_{\eta=1} = 0, \\ u_0^i|_{\Gamma_{int}} = \gamma. \end{cases} \tag{2.14}$$

The 1-st order problem is:

$$\begin{cases} -\nabla \cdot (\sigma_i \nabla u_1^i) = 0 \quad \text{in } \Omega_i, \\ \partial_\eta^2 u_1^e = -a_{33}^0 \partial_\eta u_0^e \quad \text{in } \Gamma_0 \times (0,1), \\ u_1^i|_{\Gamma_0} = u_1^e|_{\eta=0}, \\ \partial_\eta u_1^e|_{\eta=0} = 0, \\ \partial_\eta u_1^e|_{\eta=1} = 0, \\ u_1^i|_{\Gamma_{int}} = 0. \end{cases} \tag{2.15}$$

The 2-nd order problem is:

$$\begin{cases} -\nabla \cdot (\sigma_i \nabla u_2^i) = 0 \quad \text{in } \Omega_i, \\ \partial_\eta^2 u_2^e = -a_{33}^0 \partial_\eta u_1^e - \eta a_{33}^1 \partial_\eta u_0^e - S_{\Gamma_0}^0 u_0^e \quad \text{in } \Gamma_0 \times (0,1), \\ u_2^i|_{\Gamma_0} = u_2^e|_{\eta=0}, \\ \partial_\eta u_2^e|_{\eta=0} = 0, \\ \partial_\eta u_2^e|_{\eta=1} = 0, \\ u_i^2|_{\Gamma_{int}} = 0. \end{cases} \tag{2.16}$$

The 3-rd order problem is:

$$\begin{cases} -\nabla \cdot (\sigma_i \nabla u_3^i) = 0 \quad \text{in } \Omega_i, \\ \partial_\eta^2 u_3^e = -a_{33}^0 \partial_\eta u_2^e - \left(\eta a_{33}^1 \partial_\eta u_1^e + S_{\Gamma_0}^0 u_1^e\right) \\ \qquad\qquad - \eta \left(\frac{\eta}{2} a_{33}^2 \partial_\eta u_0^e + S_{\Gamma_0}^1 u_0^e\right) \quad \text{in } \Gamma_0 \times (0,1), \\ u_3^i|_{\Gamma_0} = u_3^e|_{\eta=0}, \\ \sigma_i \partial_n u_0^i|_{\Gamma_0} = \sigma_e \partial_\eta u_3^e|_{\eta=0}, \\ \partial_\eta u_3^e|_{\eta=1} = 0, \\ u_i^3|_{\Gamma_{int}} = 0. \end{cases} \tag{2.17}$$

Using the p-th problem, $p \in \{0,1,2,3\}$ one can achieve to identify the problems satisfied by the two first terms, u_0^i and u_1^i, of the expansion in the internal domain Ω_i. We prove the two following propositions (the proofs are given in Appendix A.2).

Proposition 2. *The limit problem to determine u_0^i is given by: find $(u_0^i, \alpha_0) \in H^1(\Omega_i) \times \mathbb{R}$ solution of*

$$\begin{cases} -\nabla \cdot (\sigma_i \nabla u_0^i) = f \quad \text{in } \Omega_i, \\ u_0^i|_{\Gamma_0} = \alpha_0, \\ \displaystyle\int_{\Gamma_0} \sigma_i \partial_n u_0^i \, ds = 0, \\ u_0^i|_{\Gamma_{int}} = \gamma. \end{cases} \tag{2.18}$$

with $f \in L^2(\Omega_i)$, $\gamma \in H^{\frac{1}{2}}(\Gamma_{int})$.

Proposition 3. *The problem satisfied by u_1^i is given by: find $(u_1^i, \alpha_1) \in H^1(\Omega_i) \times \mathbb{R}$ solution of*

$$\begin{cases} -\nabla \cdot \left(\sigma_i \nabla u_1^i\right) = 0 \quad \text{in} \quad \Omega_i, \\ u^i_{1|\Gamma_0} = \bar{u}_1^e + \alpha_1, \\ \displaystyle\int_{\Gamma_0} \sigma_i \, \partial_n u^i_{1|\Gamma_0} = 0, \\ u^i_{1|\Gamma_{int}} = 0, \end{cases} \tag{2.19}$$

with $\bar{u}_1^e \in H^2(\Gamma_0)$ solution of

$$\begin{cases} \sigma_e \Delta_{\Gamma_0} \bar{u}_1^e = \sigma_i \partial_n u_0^i|_{\Gamma_0}, \\ \displaystyle\int_{\Gamma_0} \bar{u}_1^e = 0. \end{cases} \tag{2.20}$$

Considering the solution a formal series with respect to the small parameter ε, one can remark that breaking the series to the zero order the measurement electrode coincides with a perfect conductor. In fact the voltage has constant value α_0 on the electrode. Since the value α_0 is a unknown of the problem, System (2.18) is a *floating potential* problem and it has the same form than System (2.6) studied in Section 2.2. Thanks to elliptic regularity shift, one has the following

Proposition 4. *Assume that $f \in H^{k-1/2}(\Omega_i)$, $\gamma \in H^{k+1}(\Gamma_{int})$, for any $k \geq 0$. Then there exists a constant C_k depending on f, γ and the domain Ω_i such that*

$$\begin{aligned} \|u_0^i\|_{H^{k+3/2}(\Omega_i)} &\leq C_k, \\ \|u_1^i\|_{H^k(\Omega_i)} &\leq C_k. \end{aligned}$$

Remark 10. *Choosing $k = 2$, a specific relation is fixed between the conductivities of the domains and their sizes. The considerations about the zero order limit problem are valid since $k = 2$. Considering the case $k = 1$, the zero order limit problem obtained by the asymptotic analysis is not a floating potential problem and it cannot be used to describe the behaviour of a quasi-perfect conductor. More details are given in Appendix A.1.*

The potential is then approached one step further with the first order correction (second term of the expansion). System (2.19) has the same form of System (2.18) related to u_0^i. As already shown in Section 2.2, Systems (2.18) and (2.19) are well-posed problem and for the resolution of both, the strategy exposed in Section 2.2 can employed. Neglecting the resolution of the 1D problem for $\bar{u}_1^e$, with this strategy it is possible to add one more order of accuracy in the solution just doubling the time computing and using the same code to get the two solution terms.

Convergence

In this section we study the convergence when ε tends to zero of the numerical solutions of System (2.1-2.3) to the solution obtained by solving System (2.6) (or System (2.18)) and System (2.19-2.20). We assume the data f, Γ_{int} and the domain Ω_i as regular as necessary so that Proposition 4 holds for k high enough. We recall that the solution u^ε has the form

$$u^\varepsilon(x) = \begin{cases} u_0^i + \varepsilon\, u_1^i + \varepsilon^2 u_2^i + \dots \\ u_0^e + \varepsilon\, u_1^e + \varepsilon^2 u_2^e + \dots \end{cases},$$

and consider the extension by zero in Ω_e^ε of the solution of the limit problems

$$\begin{cases} -\nabla\cdot(\sigma_i\,\nabla u_0^i) &=& f, & \Omega_i. \\ -\nabla\cdot(\sigma_i\,\nabla u_1^i) &=& 0, & \Omega_i, \\ u_{0|_{\Gamma_0}}^i &=& \alpha_0, & \\ u_{1|_{\Gamma_0}}^i &=& \alpha_1 + \bar{u}_1^e, & \\ u_0^i &=& \alpha_0 & \Omega_e^\varepsilon, \\ u_1^i &=& \alpha_1 + \bar{u}_1^e & \Omega_e^\varepsilon, \\ u_{0|_{\Gamma_{int}}}^i &=& \gamma, & \\ u_{1|_{\Gamma_{int}}}^i &=& 0, & \\ \displaystyle\int_{\Gamma_{ext}} \partial_n u_0^i &=& 0, & \\ \displaystyle\int_{\Gamma_{ext}} \partial_n u_1^i &=& 0. & \end{cases} \tag{2.21}$$

We define v^ε by $v^\varepsilon = u^\varepsilon - u_0 - \varepsilon u_1$ and v^ε is solution of

$$\begin{cases} -\nabla\cdot(\sigma_i\,\nabla v^\varepsilon) &=& 0, & \Omega_i, \\ \Delta v^\varepsilon &=& -\varepsilon\Delta_{\Gamma_0}\bar{u}_1^e + \varepsilon^2\psi, & \Omega_e^\varepsilon, \\ \partial_n v^\varepsilon_{|_{\Gamma_{ext}}} &=& 0, & \\ \dfrac{\sigma_e}{\varepsilon^2}\partial_n v^\varepsilon_{|_{\Gamma_0^+}} &=& \sigma_i\partial_n v^\varepsilon_{|_{\Gamma_0^-}} + \sigma_i\partial_n u^i_{0|_{\Gamma_0^-}} + \sigma_i\varepsilon\partial_n u^i_{1|_{\Gamma_0^-}}, & \\ [\![v^\varepsilon]\!]_{\Gamma_0} &=& 0, & \\ v^\varepsilon_{|_{\Gamma_{int}}} &=& 0. & \end{cases} \tag{2.22}$$

with $[\![v^\varepsilon]\!]_{\Gamma_0} := \left|v^\varepsilon{}_{|_{\Gamma_0^+}} - v^\varepsilon{}_{|_{\Gamma_0^-}}\right|$ and $\psi = O(\varepsilon)$.

Remark 11. *We have*

$$n_{|_{\Gamma_0^-}} = -n_{|_{\Gamma_0^+}} := n_{|_{\Gamma_0}}.$$

Before to make estimates of v^ε, we introduce the following propositions.

Proposition 5. *Let $\phi \in H^1(\Omega_e^\varepsilon)$ such that $\int_{\Omega_e^\varepsilon} \phi dx = 0$. There exists a constant C independant of ε such that*

$$\|\phi\|_{L^2(\Omega_e^\varepsilon)} \leq C\|\nabla\phi\|_{L^2(\Omega_e^\varepsilon)}.$$

Proof. Let define ϕ^ε by

$$\phi^\varepsilon : \left\{ \begin{array}{ccc} \Gamma_0 \times (0,1) & \to & \mathcal{R} \\ (x_T, \eta) & \mapsto & \phi(x_T, \varepsilon\,\eta) \end{array} \right. \tag{2.23}$$

we have $\partial_\eta \phi^\varepsilon = \varepsilon \partial_{\xi_3}\phi(x_T, \xi_3)$. We apply Poincaré-Wirtinger inequality on ϕ^ε: there exists a constant C which depends only on Γ_0 (then which is independant of ε) such that

$$\left\| \phi^\varepsilon - \int_{\Gamma_0\times(0,1)} \phi^\varepsilon \right\|_{L^2(\Gamma_0\times(0,1))} \leq C\|\nabla\phi^\varepsilon\|_{L^2(\Gamma_0\times(0,1))}.$$

As we have

$$\int_{\Gamma_0\times(0,1)} \phi^\varepsilon = \frac{1}{\varepsilon}\int_{\Gamma_0\times(0,\varepsilon)} \phi = 0,$$

$$\int_{\Gamma_0\times(0,1)} (\phi^\varepsilon)^2 = \frac{1}{\varepsilon}\int_{\Gamma_0\times(0,\varepsilon)} (\phi)^2$$

and

$$\int_{\Gamma_0\times(0,1)} |\nabla\phi^\varepsilon|^2 = \frac{1}{\varepsilon}\int_{\Gamma_0\times(0,\varepsilon)} ((\partial_{x_T}\phi)^2 + \varepsilon^2(\partial_\eta\phi)^2) \leq \frac{1}{\varepsilon}\int_{\Gamma_0\times(0,\varepsilon)} ((\partial_{x_T}\phi)^2 + (\partial_\eta\phi)^2) \text{ since } \varepsilon \text{ is small,}$$

we obtain

$$\|\phi\|_{L^2(\Omega_e^\varepsilon)} \leq C\|\nabla\phi\|_{L^2(\Omega_e^\varepsilon)}.$$

□

Proposition 6. *Let $\phi \in H^1(\Omega_e^\varepsilon)$ such that $\int_{\Omega_e^\varepsilon} \phi dx = 0$. There exists a constant independent of ε such that*

$$\|\phi\|_{L^2(\Gamma_0)} \leq C\varepsilon^{-1/2}(\|\phi\|_{L^2(\Omega_e^\varepsilon)} + \|\nabla\phi\|_{L^2(\Omega_e^\varepsilon)}).$$

Proof. We apply Sobolev trace inequality on ϕ^ε (defined in the proof of Proposition 5): there exists a constant C (independant of ε) such that

$$\|\phi^\varepsilon\|_{L^2(\Gamma_0)} \leq C\|\phi^\varepsilon\|_{H^1(\Gamma_0\times(0,1))} \leq C(\|\phi^\varepsilon\|_{L^2(\Gamma_0\times(0,1))} + \|\nabla\phi^\varepsilon\|_{L^2(\Gamma_0\times(0,1))})$$

Using computations of Proposition 5 and

$$\|\phi^\varepsilon\|_{L^2(\Gamma_0)} = \|\phi\|_{L^2(\Gamma_0)},$$

we obtain the expected result. □

Now we can pass to make estimates of v^ε. ****
Multiplying the first equation of System (2.22) by v^ε and integrating by parts leads to

$$\begin{aligned}\int_\Omega \nabla\cdot(\sigma\nabla v^\varepsilon)\, v^\varepsilon =& \frac{\sigma_e}{\varepsilon^2}\int_{\Omega_e^\varepsilon}\Delta v^\varepsilon\, v^\varepsilon + \int_{\Omega_i}\nabla\cdot(\sigma_i\nabla v^\varepsilon)\, v^\varepsilon \\ =& -\frac{\sigma_e}{\varepsilon^2}\int_{\Omega_e^\varepsilon}\nabla v^\varepsilon\cdot\nabla v^\varepsilon - \int_{\Omega_i}\sigma_i\nabla v^\varepsilon\cdot\nabla v^\varepsilon + \frac{\sigma_e}{\varepsilon^2}\int_{\Gamma_{ext}}\partial_{n_{|\Gamma_{ext}^-}} v^\varepsilon\, v^\varepsilon \\ &+ \frac{\sigma_e}{\varepsilon^2}\int_{\Gamma_0}\partial_{n_{|\Gamma_0^+}} v^\varepsilon\, v^\varepsilon + \int_{\Gamma_0}\sigma_i\partial_{n_{|\Gamma_0^-}} v^\varepsilon\, v^\varepsilon + \int_{\Gamma_{int}}\sigma_i\partial_{n_{|\Gamma_{int}^-}} v^\varepsilon\, v^\varepsilon.\end{aligned}$$

Using Remark 11 and System (2.22), we obtain

$$\frac{\sigma_e}{\varepsilon^2}\int_{\Omega_e^\varepsilon}\left(-\varepsilon\Delta_{\Gamma_0}\bar{u}_1^e+\varepsilon^2\psi\right)v^\varepsilon = -\frac{\sigma_e}{\varepsilon^2}\int_{\Omega_e^\varepsilon}|\nabla v^\varepsilon|^2 - \int_{\Omega_i}\sigma_i\,|\nabla v^\varepsilon|^2 + \int_{\Gamma_0}\sigma_i\left(\partial_n u_0^i+\varepsilon\partial_n u_1^i\right)v^\varepsilon.$$

Finally we infer

$$\begin{aligned}\frac{\sigma_e}{\varepsilon^2}\int_{\Omega_e^\varepsilon}|\nabla v^\varepsilon|^2 + \int_{\Omega_i}\sigma_i\,|\nabla v^\varepsilon|^2 &= -\frac{\sigma_e}{\varepsilon^2}\int_{\Omega_e^\varepsilon}\left(-\varepsilon\Delta_{\Gamma_0}\bar{u}_1^e+\varepsilon^2\psi\right)v^\varepsilon + \int_{\Gamma_0}\sigma_i\left(\partial_n u_0^i+\varepsilon\partial_n u_1^i\right)v^\varepsilon \\ &= \int_{\Gamma_0}\left(\varepsilon\,\nabla u_1^i\cdot n_{\Gamma_0}+\varepsilon\psi\right)v^\varepsilon\, dx_T. \qquad (2.24)\end{aligned}$$

Choose now φ as the solution of the following system

$$\left\{\begin{array}{rcll}\Delta\varphi & = & 0 & \Omega_e^\varepsilon \\ \partial_n\varphi_{|\Gamma_0} & = & \varepsilon\,\nabla u_1^i\cdot n_{\Gamma_0}+\varepsilon\psi & \\ \partial_n\varphi_{|\Gamma_{ext}} & = & 0 & \\ \int_{\Omega_e^\varepsilon}\phi & = & 0 & \end{array}\right. \qquad (2.25)$$

Using Proposition 5 and 6, there exists C independent of ε such that $\|\varphi\|_{L^2(\Gamma_0)} \le C\varepsilon^{-1/2}\|\nabla\varphi\|_{L^2(\Omega_e^\varepsilon)}$.
Then using the Green's identity, it follows that

$$\begin{aligned}\|\nabla\varphi\|^2_{L^2(\Omega_e^\varepsilon)} &= \int_{\Gamma_0}\partial_n\varphi\,\varphi - \int_{\Omega_e^\varepsilon}\Delta\varphi\,\varphi \\ &\le \int_{\Gamma_0}\partial_n\varphi\,\varphi \\ &\le \varepsilon\,\left\|\nabla u_1^i\cdot n_{\Gamma_0}+\psi\right\|_{L^2(\Gamma_0)}\|\varphi\|_{L^2(\Gamma_0)} \\ &\le C\varepsilon^{1/2}\|\nabla\varphi\|_{L^2(\Omega_e^\varepsilon)}.\end{aligned}$$

Then we can infer that there exists $C\in\mathbb{R}$ independent of ε such that

$$\|\nabla\varphi\|_{L^2(\Omega_e^\varepsilon)} \le C\varepsilon^{1/2}. \qquad (2.26)$$

Multiplying the first equation of System (2.25) by v^ε and integrating by parts lead to

$$\int_{\Omega_e^\varepsilon} \Delta\varphi v^\varepsilon = -\int_{\Omega_e^\varepsilon} \nabla\varphi \cdot \nabla v^\varepsilon + \int_{\Gamma_{ext}} \partial_n\varphi\, v^\varepsilon + \int_{\Gamma_0} \partial_n\varphi\, v^\varepsilon.$$

Hence

$$\int_{\Gamma_0} \left(\varepsilon\, \nabla u_1 \cdot n_{\Gamma_0} + \varepsilon\psi\right)\, v^\varepsilon = \int_{\Omega_e^\varepsilon} \nabla\varphi \cdot \nabla v^\varepsilon.$$

From (2.24), using Cauchy-Schwarz inequality, we infer

$$\frac{\sigma_e}{\varepsilon^2}\|\nabla v^\varepsilon\|^2_{L^2(\Omega_e^\varepsilon)} + \sigma_i\|\nabla v^\varepsilon\|^2_{L^2(\Omega_i)} \leq \|\nabla\varphi\|_{L^2(\Omega_e^\varepsilon)}\|\nabla v^\varepsilon\|_{L^2(\Omega_e^\varepsilon)}.$$

Using Equation 2.26, one can prove that

$$\|\nabla v^\varepsilon\|_{L^2(\Omega_e^\varepsilon)} \leq C\varepsilon^{5/2}, \qquad \|\nabla v^\varepsilon\|_{L^2(\Omega_i)} \leq C\varepsilon^{\sqrt{5}/2}. \tag{2.27}$$

Using uniform estimates (2.27) and the fact that $v^\varepsilon_{|\Gamma_{int}} = 0$, we obtain that v^ε tends to 0 when ε approaches 0. The order of convergence is comprised between 1 and 2. Considering the 0 order approximation, we have

$$\begin{aligned}\|u^\varepsilon - u_0^i\|_{H^1(\Omega_i)} &\leq \|u^\varepsilon - u_0^i - \varepsilon u_1^i\|_{H^1(\Omega_i)} + \varepsilon\|u_1^i\|_{H^1(\Omega_i)} \\ &= \|\nabla v^\varepsilon\|_{L^2(\Omega_i)} + \varepsilon\|u_1^i\|_{H^1(\Omega_i)}.\end{aligned}$$

Using (2.27), we infer that the order of convergence for u_0^i is equal to 1. Following the same strategy by studying the terms with $\varepsilon^2 u_2^i$ can give order 2 for $u_0^i + \varepsilon u_1^i$.

Numerical assessment of 1st order solution

In this section we prove numerically the theoretical result obtained in Section 2.3 about the convergence order given by the solutions of System (2.18) and System (2.19) and the exact solution of System (2.1-2.3) when ε tends to zero. We consider the same hypothesis of the *toy model* used in Section 2.2. As we can see in Figure 2.10, the convergence is reached when ε approaches zero with the expected order. However, when the ε is too small, the accuracy of the finite difference solution at the first order is not sufficient enough and the error due to the mesh is greater than the error due to the truncation of the asymptotic expansion.

2.4 Conclusion and perspectives

It has been studied in this chapter two ways to model the behaviour of the electric potential in presence of an inactive electrode. In particular, it has been considered the case of a 4-electrode system with *thin film* electrode. We have started by considering a transmission problem between two domains with an important difference in the conductivities. Using a difference finite method, the small dimensions of the electrode respect to the whole domain requires a small discretization step. Furthermore, we have proved that the high contrasts in the conductivities and in the sizes of the two domains lead to use a *ill-conditioned* matrix. These two

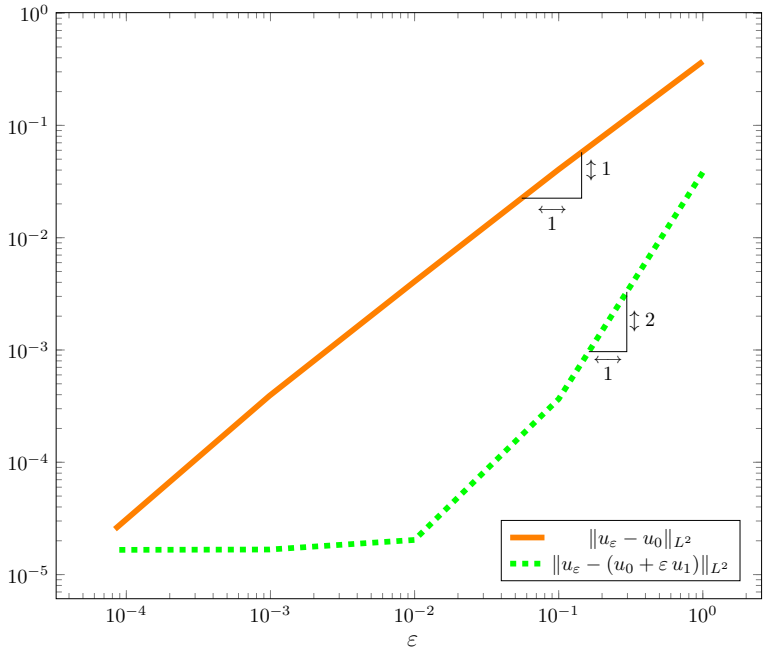

Figure 2.10 – The distance between the exact solutions and the numerical solutions found with a *floating potential* tends to zero when ε approaches zero at the expected order.

aspects bring to a high computational cost and unstable solution. A *floating potential* problem is therefore treated. We have proved the existence and uniqueness of the solution of the problem. The proof also allows us to traduce the zero-flux constraint into two Dirichlet problems. From this, we can compute the value of the unknown constant potential. We have observed that one can use a coarse mesh to solve the system. Then, with the *floating potential* approach, a more stable and accurate solution is obtained with a low computational cost. An asymptotic analysis was set up based on the small value ε to show the connection between the two domains problem and the *floating potential* problem. We impose the ratio between the electrode thickness and the total domain size $\delta = \varepsilon$ and the ratio between the high and low conductivities $\xi = \varepsilon^k$. We have proved that in the case $k = 2$, we obtain the *floating potential* problem already studied. The other terms can be computed by resolving a similar problem in order to increase the approximation of the electrode as a not-perfect conductor. The convergence study shows that this approach enables to improve the solution when perfect conductor is assumed.

Our work represents a good theoretical basis to model a realistic 4-electrode system. To improve the accuracy of the solution, we could consider a problem with non linear dependence of the conductivities with respect to the electric field.

Chapter 3

Validation of the floating potential model for an arranged 4-electrode setup

3.1 Introduction

The main goal of this chapter is to link the two previous chapters: the Electrical Impedance Spectroscopy (EIS) data analysis discussed in Chapter 1 and the floating potential (FP) model developed in Chapter 2. We compute numerically the experimental 4-electrode set-up in a 2D domain thanks to geometric assumption. Similarly to Chapter 1, the experimental data come from [20]. As already explained previously, the micro-electrode set-up is composed by six parallel spiral shape electrodes of length $75 \times 10^{-6} \times 0.1\text{m}^2$ and spaced of 150μm from each other (see Figure 3.1a). As depicted by Figure 3.1b, the device is placed on a Petri dish of thickness of 13μm filled up with a saline solution with or without adhered cells on the bottom.

The electric potential u satisfies the electroquasistatic approximation with well-designed boundary conditions, namely non homogeneous Neumann conditions on the active electrodes and FP condition on the passive electrodes. As argued, FP condition has to be preferred to the classical methods as the homogeneous Neumann conditions, which are not realistic, and to the penalization method which is numerically expensive and unstable.

In what follows, we present the simulations of a system composed of buffer in which an AC signal is imposed by two active electrodes. There are also four passive electrodes to simulate the measurement electrodes of the experiments. An essential point of this chapter is the comparison between the simulations and the experimental data. This step is necessary to validate the calibration method and the equivalent circuit of the impedance and the modeling with the floating potential.

In Section 3.2, we formalize the problem to solve, inspired by the experimental set-up. Section 3.3 presents the numerical computation of the problem and shows the obtained results. Section 3.4 discusses the comparison between the simulations and the experimental data. Finally, Section 3.6 presents the conclusions and the perspectives of this work.

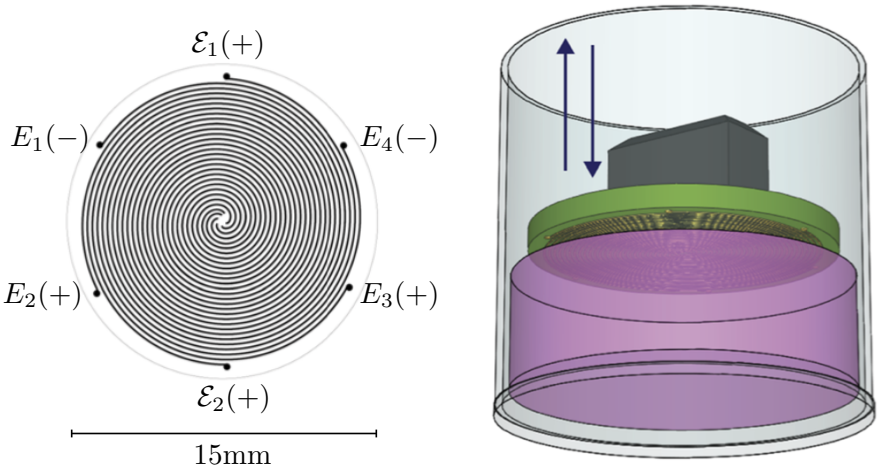

(a) Micro-electrode assembly. **(b)** Experiment set-up.

Figure 3.1 – On the left, a representation of the spiral micro-electrode geometry where are marked the different spirals: two of them are the active electrodes, $\mathcal{E}_\alpha$ and $\mathcal{E}_\beta$, and the other four ($\mathcal{E}_\gamma$, $\mathcal{E}_\delta$, $\mathcal{E}_\epsilon$ and $\mathcal{E}_\zeta$) are used to measure the voltage. On the right, a representation of the experiment set-up: the micro-electrode is placed above the cells inside a cylindrical plate. Images source: [20].

3.2 Application of the floating potential condition to the arranged 4-electrode measurement system

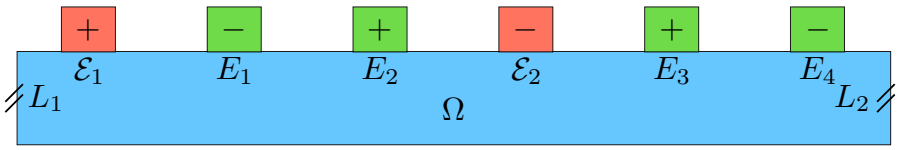

Figure 3.2 – Section of the plate filled with the buffer: intersections with six electrodes (two active and four passive electrodes).

The aim of the chapter is to reproduce numerically the experiment performed in [20] in a 2D domain Ω representing a section of the plate filled with the buffer, with conductivity σ, and presenting on the top the intersections with six electrodes (two active and four passive). Figure 3.2 gives a representation of Ω. The active electrodes impose on the buffer an AC signal in harmonic regime. The passive electrodes consist of four equipotential surfaces of the domain boundary whose potential values are unknowns of the system.

Consider a rectangular domain Ω with six perfect inclusions, and denote with E_j, $j \in \{1,2,3,4\}$ and with $\mathcal{E}_k$, $k \in \{1,2\}$ the interfaces between the inclusions and Ω as shown in Figure 3.2. We denote with L_1 and L_2 respectively the left side and the right side of Ω, and with $\partial\Omega$ the outer boundary of Ω.

The electroquasistatic potential u is the solution to the following problem: for given functions $(g_1, g_2) \in H^{-\frac{1}{2}}(\mathcal{E}_1) \times H^{-\frac{1}{2}}(\mathcal{E}_2)$ such that $\int_{\mathcal{E}_1} g_1 dx + \int_{\mathcal{E}_2} g_2 dx = 0$

and a given function σ strictly positive in Ω, find $(u, \alpha_1, \alpha_2, \alpha_3, \alpha_4) \in H^1(\Omega) \times \mathbb{R}^4$ solution of

$$\begin{cases} \nabla \cdot (\sigma \nabla u) = 0, \quad \text{in } \Omega, \\ \sigma \partial_{n_{\mathcal{E}_1}} u_{|\mathcal{E}_1} = g_1, \qquad \sigma \partial_{n_{\mathcal{E}_2}} u_{|\mathcal{E}_2} = g_2, \\ u_{|E_j} = \alpha_j, \quad j = 1, 2, 3, 4, \\ \displaystyle\int_{E_j} \sigma \partial_{n_{E_j}} u \, ds = 0, \quad j = 1, 2, 3, 4, \\ u_{|L_1} = u_{|L_2}, \\ \sigma \partial_n u = 0 \quad \text{otherwise.} \end{cases}$$

To ensure uniqueness of the solution, a Gauge condition has to be imposed. For the sake of simplicity we choose $\int_{E_1} u dx = 0$, which is equivalent to set $\alpha_1 = 0$. In addition, in the experimental set-up, the electrodes $\mathcal{E}_1$ and $\mathcal{E}_2$ are identical and the current imposed on $\mathcal{E}_1$ is the opposite of the current imposed on $\mathcal{E}_2$. Thus by abuse of notation we set $g := g_1 = -g_2$ and the problem reads

$$\begin{cases} \nabla \cdot (\sigma \nabla u) = 0, \quad \text{in } \Omega, \\ \sigma \partial_{n_{\mathcal{E}_1}} u_{|\mathcal{E}_1} = g, \qquad \sigma \partial_{n_{\mathcal{E}_2}} u_{|\mathcal{E}_2} = -g, \\ u_{|E_j} = \alpha_j, \quad j = 2, 3, 4, \qquad u_{|E_1} = 0, \\ \displaystyle\int_{E_j} \sigma \partial_{n_{E_j}} u \, ds = 0, \quad j = 2, 3, 4, \\ u_{|L_1} = u_{|L_2}, \\ \sigma \partial_n u = 0 \quad \text{otherwise.} \end{cases} \tag{3.1}$$

In order to prove the existence and uniqueness of System (3.1), $\forall i \in \{2, 3, 4\}$, we consider the following Dirichlet-to-Neumann operators

$$\Lambda_0^{(i)} : H^{-\frac{1}{2}}(\mathcal{E}_1) \cap H^{-\frac{1}{2}}(\mathcal{E}_2) \longrightarrow H^{-\frac{1}{2}}(E_i),$$
$$\gamma \overset{\Lambda_0^{(i)}}{\longmapsto} \sigma \partial_n w_{|E_i} \quad \text{s. t.}$$

$$\begin{cases} \nabla \cdot (\sigma \nabla w) = 0, \quad \text{in } \Omega, \\ \sigma \partial_{n_{\mathcal{E}_1}} w_{|\mathcal{E}_1} = \gamma, \qquad \sigma \partial_{n_{\mathcal{E}_2}} w_{|\mathcal{E}_2} = -\gamma, \qquad w_{|E_1} = 0, \\ w_{|E_j} = 0, \quad j = 2, 3, 4, \\ w_{|L_1} = w_{|L_2}, \\ \sigma \partial_n w = 0 \quad \text{otherwise,} \end{cases} \tag{3.2}$$

and for any $j \in \{2, 3, 4\}$

$$\Lambda_j^{(i)} : H^{\frac{1}{2}}(E_j) \longrightarrow H^{-\frac{1}{2}}(E_i),$$
$$\delta \overset{\Lambda_j^{(i)}}{\longmapsto} \sigma \partial_{n_{E_i}} v_{j|_{E_i}} \quad \text{s. t.}$$

$$\begin{cases} \nabla \cdot (\sigma \nabla v_j) = 0, \quad \text{in } \Omega, \\ \sigma \partial_{n_{\mathcal{E}_1}} v_{j|_{\mathcal{E}_1}} = 0, \qquad \sigma \partial_{n_{\mathcal{E}_2}} v_{j|_{\mathcal{E}_2}} = 0, \qquad v_{j|_{E_1}} = 0 \\ v_{j|_{E_j}} = \delta, \qquad v_{j|_{E_k}} = 0 \quad k \neq j \in \{2, 3, 4\}, \\ v_{j|_{L_1}} = v_{j|_{L_2}}, \\ \sigma \partial_n v_j = 0 \quad \text{otherwise,} \end{cases} \tag{3.3}$$

Considering u solution of System (3.1), it is easy to get

$$\sigma \partial_n u_{|_{E_i}} = \Lambda_0^{(i)}(g) + \sum_{j=2}^{4} \alpha_j \Lambda_j^{(i)}(1), \quad \forall i \in \{2,3,4\}.$$

Then, the floating boundary conditions of System (3.1)

$$\begin{aligned} u_{|_{E_j}} &= \alpha_j, \quad j = 2,3,4, \\ \int_{E_j} \sigma\, \partial_{n_{E_j}} u \, ds &= 0 \quad \forall j \in \{2,3,4\}, \end{aligned}$$

read as

$$A\,\overline{\alpha} = \overline{b}, \tag{3.4}$$

where the vectors $\overline{\alpha}$ and $\overline{b}$ are

$$\overline{\alpha} = \begin{pmatrix} \alpha_2 \\ \alpha_3 \\ \alpha_4 \end{pmatrix}, \qquad b = \left(- \int_{E_i} \Lambda_0^{(i)}(g) \right)_{i=2,\dots,4},$$

and the matrix $A = (A_{ij})$ is

$$A_{ij} = \int_{E_i} \Lambda_j^{(i)}(1)\, ds \quad \forall i,j \in \{2,3,4\}.$$

Proposition 7. *Let σ be a positive constant, the matrix A can be rewritten as a Gram matrix*

$$A_{ij} = \int_\Omega \sigma \nabla v_i \cdot \nabla v_j \, d\mathbf{x}, \quad \forall i,j \in \{2,3,4\}, \tag{3.5}$$

where v_k, $k \in \{2,3,4\}$, solution of

$$\begin{cases} \nabla \cdot (\sigma \nabla v_k) = 0, \quad \text{in } \Omega, \\ \sigma \partial_{n_{\varepsilon_1}} v_{k|_{\varepsilon_1}} = 0, \qquad \sigma \partial_{n_{\varepsilon_2}} v_{k|_{\varepsilon_2}} = 0, \qquad v_{k|_{E_1}} = 0 \\ v_{k|_{E_k}} = 1, \qquad v_{k|_{E_l}} = 0 \quad l \neq k, \\ v_{k|_{L_1}} = v_{k|_{L_2}}, \\ \sigma \partial_n v_k = 0 \quad \text{otherwise.} \end{cases} \tag{3.6}$$

Therefore, A is symmetric definite positive.

Proof. By Definition (3.6) of the function v_k, one has:

$$A_{ij} = \int_{E_i} \Lambda_j^{(i)}(1)\, ds = \int_{E_i} \sigma \partial_{n_{E_i}} v_j \, v_i \, ds = \int_\Omega \sigma \nabla v_j \cdot \nabla v_i \, d\mathbf{x}.$$

This directly implies that A is a symmetric Gram matrix. Therefore, to show that A is positive definite one has to show that the functions $(\nabla v_j)_{j=2,3,4}$ are linearly independent. Let $(\lambda_i)_{i=2,3,4} \in \mathcal{R}^3 \setminus \{0\}$ be such that

$$\sum_{i=2}^{4} \lambda_i \nabla v_i = 0.$$

Then the function $w = \sum_{i=2}^{4} \lambda_i v_i$ satisfies

$$\begin{cases} \nabla \cdot (\sigma \nabla w) = 0, \quad \text{in } \Omega, \\ \sigma \partial_{n\varepsilon_1} w_{|\varepsilon_1} = 0, \qquad \sigma \partial_{n\varepsilon_2} w_{|\varepsilon_2} = 0, \qquad w_{|E_1} = 0 \\ w_{|E_k} = 1, \ \forall k = 2, 3, 4, \\ w_{|L_1} = w_{|L_2}, \\ \sigma \partial_n w = 0 \quad \text{otherwise.} \end{cases}$$

Then $w \neq 0$, and thus ∇w since $w_{|E_1} = 0 \neq w_{|E_k}$ for $k = 2, 3, 4$, which is a contradiction. Therefore $\lambda_i = 0$ for all $i = 2, 3, 4$, which ends the proof of the proposition. □

Using Equation (3.4), we can compute the constants α_i, $i = 2, 3, 4$ using appropriate Dirichlet-to-Neumann maps. Once imposed or computed the α_i, $i = 1, 2, 3, 4$, System (3.1) is an elliptic problem which admits a unique solution in $u \in H^1(\Omega)$.

3.3 Numerical results

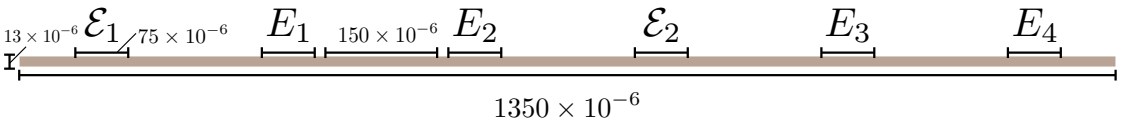

Figure 3.3 – The domain Ω consists in a rectangle with base of 1350×10^{-6}m and height of 13×10^{-6}m. On top there are the boundaries representing the buffer-electrode interface of size 75×10^{-6}m and spaced 150×10^{-6}m.

In this section, simulations of the model presented in Section 3.2 have been presented. Our final objective is to compare the impedances numerically measured from the solutions of System (3.1) with the data of impedances presented in Chapter 1.

The proof of the existence and uniqueness of a solution of System (3.1) also provides a resolution strategy. First, we solve System (3.2) and the third systems in the form of System (3.3) in order to obtain the values of the α_i, $i = 2, 3, 4$. Finally, we can solve System (3.1) with the FP conditions are translated in terms of Dirichlet conditions.

A C++ Finite Difference Method (FDM) library (around 3500 code lines) has been implemented to numerically solve the strategy presented above on a 2D Cartesian grid. All the equations are discretized with usual second-order methods. According to the experiments, the simulations are computed in a domain $\Omega = [1350e^{-6}, 13e^{-6}]\,(m)$, on a 2D grid (of 2701×261 nodes).

The conductivity σ is assumed real, positive and constant in all the domain Ω. Table 3.1 lists the buffer conductivities that we have estimated, see Chapter 1 for more details, and that we have used in the simulations.

[KCl] (mM)	0	25	50	75	100
σ ($S{\cdot}m^{-1}$)	0.098*	0.265	0.57	0.965	1.432

Table 3.1 – Conductivities of the Free-Cell solutions computed thanks to Equation (1.27) and Equation (1.28), with $k = 59.13$ and $K = -42.14$. (*) Value already available.

Remark 12. *The permittivity of the buffer without cells is neglected. Indeed instead of considering*

$$\sigma + i\omega\epsilon,$$

where σ is the conductivity, ϵ the permittivity and ω the angular frequency, we consider only the conductivity σ. This choice can be justified by recalling that in the free-cells case $\epsilon = \epsilon_0 \times \epsilon_r = 8.8541 \times 10^{-12} \times 78.57 \approx 6.956 \times 10^{-10} F.m^{-1}$ (see Section 1.5 in Chapter 1 for more details). This implies that the potential, and in particular the impedances computed in the next section, does not depend on the angular frequency ω.

According to García-Sánchez et al. [20], the current imposed by the active electrodes and denoted by C_a equals to 500μA. This implies that

$$g = \frac{C_a}{|\mathcal{E}_1|} = \frac{C_a}{|\mathcal{E}_2|} = \frac{500}{|\mathcal{E}_2|}$$

in $\mathcal{E}_1 \cup \mathcal{E}_2$. Using the estimation of the length of the electrodes given in Section 1.4 in Chapter 1, we have

$$|\mathcal{E}_1| = |\mathcal{E}_2| = \text{elec. width} \times \text{elec. length} = 75 \times 10^{-6} \times 0.1 = 7.5 \times 10^{-6} \text{ m}.$$

Remark 13. *To model the 4-electrode experiment, we have assumed that the potential is homogeneous along the third dimension of the electrodes. That leads us to say that the micro-electrode in spiral shape, used for the experiments, has the same efficacy but a more compact size of a device with straight electrodes of the same length.*

Figure 3.4 shows the spatial evolution of u in Ω for several buffer conductivities. The potential evolution on a line placed on the upper boundary is showed in

σ ($S{\cdot}m^{-1}$)	α_1	α_2	α_3	α_4
0.098	0	0.314	0.314	-2.2×10^{-6}
0.265	0	0.116	0.116	-9.4×10^{-7}
0.57	0	0.054	0.054	-4.3×10^{-7}
0.965	0	0.032	0.032	-2.6×10^{-7}
1.432	0	0.021	0.021	-1.7×10^{-7}

Table 3.2 – The computed values of the potential on the passive electrodes for several buffer conductivities.

Figure 3.5 for several buffer conductivities. The potential reaches the peak at the centers of $\mathcal{E}_1$ and $\mathcal{E}_2$ and has constant values α_i in E_i, $i \in \{1, 2, 3, 4\}$. Table 3.2 lists the computed α_i, $i \in \{2, 3, 4\}$ in relation to the buffer conductivities. One can remark that, the passive electrodes E_2 and E_3 (respectively E_1 and E_4) have the same potential. This means that the electric potentials at two points located at the same distance with respect to the active electrodes are identical.

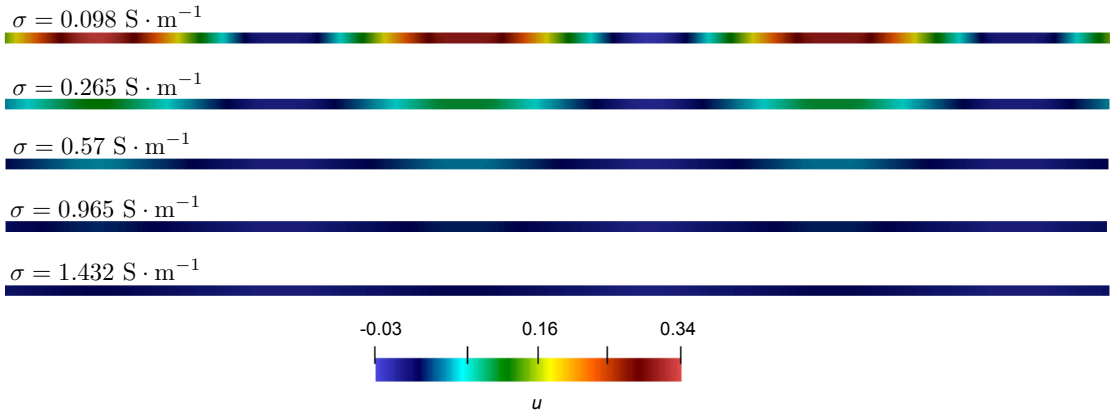

Figure 3.4 – Spatial evolution of the potential inside the buffer, in presence of the arranged 4-electrode measurement system for several buffer conductivities.

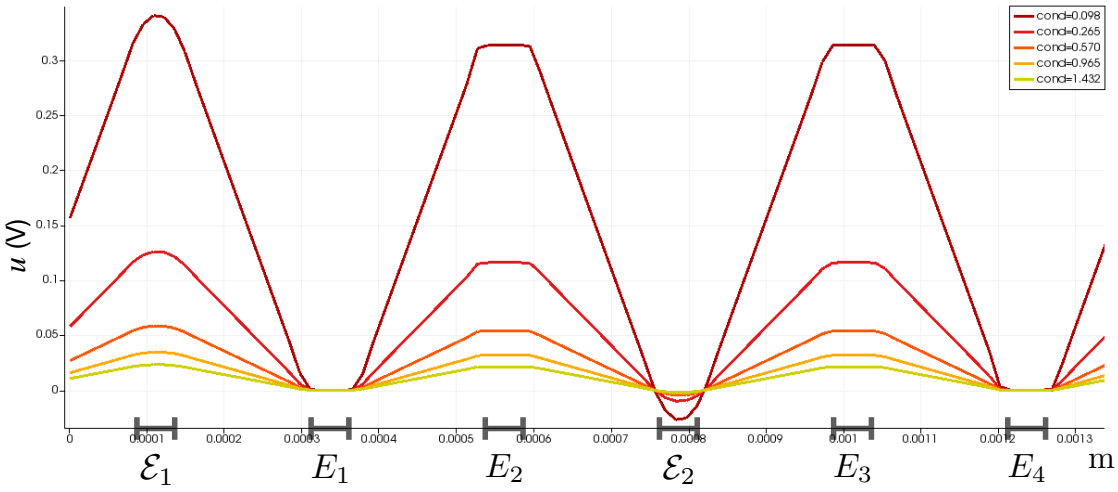

Figure 3.5 – Spatial evolution of the potential at the electrode level for several buffer conductivities. When σ increases, the potential intensity decreases.

3.4 Impedance computation

To validate the model and in particular the floating potential boundary conditions, we have compared the data of impedances obtained from the experiments in the case of the absence of cells with the impedances obtained from the numerical solutions. Using our numerical results, we can compute the sample impedance

denoted Z_s in Chapter 1 (see Section 1.4 for the full definition in the context of the 4-electrode experiment) by:

$$Z_s^{num} = \frac{\frac{1}{|S_2|}\int_{S_2} udS - \frac{1}{|S_1|}\int_{S_1} udS}{\int_{S_1} \sigma \partial_n u dS}, \tag{3.7}$$

where the surfaces S_1 and S_2 are the surfaces which are parallel to the vertical sides of Ω, placed between E_1 and E_2 and at a distance of 75μm respectively from E_1 and E_2 (see Figure 3.6). But we can also compute an approximation of the effective measured impedance of the 4-electrode experiment denoted by Z_m in Chapter 1 (see Section 1.4 for more details) corresponding to the ratio between the measured potential and the imposed current

$$Z_m^{num} = \frac{\alpha_2 - \alpha_1}{C_a},$$

considering the part of the domain placed between $\mathcal{E}_1$ and $\mathcal{E}_2$ and containing E_1 and E_2. We recall that in Remark 12, we have explained why the impedances obtained with the numerical solutions of System 3.1 do not depend on the angular frequency ω. It is not the case of the impedance measured with the 4-electrode experiment. To compare both, we consider $|Z_{FC,m}(\omega_1)|$, representing the averaged impedance module of the data before the calibration and measured at the lowest frequency. We start by the comparison between Z_m^{num} and $|Z_{FC,m}(\omega_1)|$. The results are given in Table 3.3. The relative error between the two impedances Err$=\frac{|Z_m^{num}-|Z_{FC,m}(\omega_1)||}{|Z_m^{num}|}$ ranges between a maximum of 22%, for the lowest conductivity, to a minimum of 1.2%, for the highest conductivity. We recall that the data noise factors (measurement system effects, electrode polarization, etc.) increase for low conductivities. This can explain the high values obtained for $\sigma = 0.098$ S·m^{-1} and $\sigma = 0.265$ S·m^{-1}. On the other hand, the small errors for the highest conductivities validate the simulations: the FP conditions reproduce with a satisfactory result the interactions between the active electrodes and passive electrodes. Although the numerical resolution of n passive electrodes requires the numerical resolution of $n+2$ systems, the FP model is still preferable to the penalization approach, as already discussed in Chapter 2. Using a penalization approach, the instability of the method and

σ (S·m^{-1})	Z_m^{num} (Ohm)	$\lvert Z_{FC,m}(\omega_1)\rvert$ (Ohm)	Err (%)
0.098	620	482	22
0.265	232	187	19
0.57	108	110	1.85
0.965	64	62	3
1.432	42	41	1.2

Table 3.3 – Comparison between the impedances Z_m^{num} obtained with the simulations and the impedances measured with the 4-electrode experiment $|Z_{FC,m}(\omega_1)|$ for several conductivities.

σ (S·m^{-1})	Z_s^{num} (Ohm)	$\lvert Z_{FC,cal}(\omega_1)\rvert$ (Ohm)	Err (%)
0.098	610	593	2.8
0.265	204	219	7.3
0.57	114	102	10.5
0.965	62	60	3.2
1.432	40	41	2.5

Table 3.4 – Comparison between the impedances Z_s^{num} obtained with the simulations and the impedances calibrated $|Z_{FC,cal}(\omega_1)|$ for several conductivities.

the relatively small size of the domain make the resolution of the system time consuming and not robust. On the contrary, the FP approach requires the resolution of classical Dirichlet-Neumann problems having all the same matrix of resolution. Thus, it is possible to set a method of resolution in which the matrix is factorized only one time (if linear solver is used) for all the problems (that can also be solved in parallel). Such a method is robust and has a low computational cost. One can remark that this also validates the estimation of the buffer conductivities and the computation of the length of the electrodes.

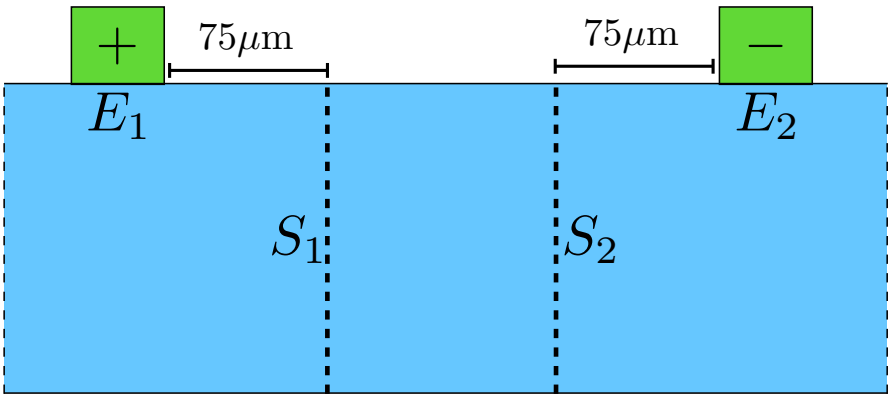

Figure 3.6 – The part of domain having the same impedance than the calibrated data corresponds to the portion of Ω delimited by the surfaces S_1 and S_2.

Now we will compare Z_s^{num} (defined in Equation 3.7) with the calibrated impedance denoted $|Z_{FC,cal}(\omega_1)|$ obtained from $|Z_{FC,m}(\omega_1)|$ by using the calibration strategy proposed in Section 1.5 of Chapter 1. The results are given in Table 3.4. The relative error between the two impedances Err$=\frac{|Z_s^{num}-|Z_{FC,cal}(\omega_1)||}{|Z_s^{num}|}$ ranges between a maximum of 10.5% to a minimum of 2.5%. The excellent results allows us to validate our modeling strategy but also the calibration strategy proposed in Section 1.5 of Chapter 1.

3.5 System with cells

We have obtained very interesting results with the free-cell buffer. Further confirmation of these results could derive directly from the observations of the 4-

electrode experiment with cells. In this experiment, we consider two domains Ω_{int} and Ω_{ext} where Ω_{int} correspond to the domain at the cell cytoplasm compartment at the bottom of the buffer and Ω_{ext} is the buffer above the cells. The interface between Ω_{int} and Ω_{ext} is denoted by $\Gamma^{(m)}$. It corresponds to the cell membranes. The electrical properties of the membrane are the capacitance C_m and the conductance S_m. Note that the impedance measurements are performed before and after the electroporating pulse (and not during the pulse), thus the membrane capacitance and conductance take very different values before and after the electroporating pulse, but no nonlinearly are accounted for. To model this more complex experiment, we complete System (3.1) with transmissions conditions at the interface $\Gamma^{(m)}$. The new system to solve reads: find $(u, \alpha_1, \alpha_2, \alpha_3, \alpha_4) \in H^1(\Omega_{int} \cup \Omega_{ext}) \times \mathbb{R}^4$ solution of

$$\begin{cases} -\nabla \cdot (\sigma \nabla u) = 0, \quad \text{in } \Omega_{int} \cup \Omega_{ext}, \\ \sigma_{ext} \partial_{n_\Gamma} u_{|_{\Gamma^{(m)},+}} = \sigma_{int} \partial_{n_\Gamma} u_{|_{\Gamma^{(m)},-}} = (i\omega C_m + S_m)(u_{|_{\Gamma^{(m)},+}} - u_{|_{\Gamma^{(m)},-}}), \\ \sigma \partial_{n_{\mathcal{E}_1}} u_{|_{\mathcal{E}_1}} = g_1, \qquad \sigma \partial_{n_{\mathcal{E}_2}} u_{|_{\mathcal{E}_2}} = g_2, \\ u_{|_{E_i}} = \alpha_i, \quad i = 2, 3, 4, \ u_{|_{E_1}} = 0 \\ \displaystyle\int_{E_i} \sigma \partial_{n_{E_i}} u \, ds = 0, \quad i = 2, 3, 4, \\ u_{|_{L_1}} = u_{|_{L_2}}, \\ \sigma \partial_n u = 0 \quad \text{otherwise.} \end{cases} \tag{3.8}$$

with n_Γ the normal to the surface $\Gamma^{(m)}$ directed towards the domain Ω_{ext},

$$\sigma(\mathbf{x}) = \begin{cases} \sigma_{int}(\mathbf{x}) > 0 \text{ if } \mathbf{x} \in \Omega_{int}, \\ \sigma_{ext}(\mathbf{x}) > 0 \text{ if } \mathbf{x} \in \Omega_{ext}, \end{cases}$$

and $(g_1, g_2) \in H^{-\frac{1}{2}}(\mathcal{E}_1) \times H^{-\frac{1}{2}}(\mathcal{E}_2)$ such that $\int_{\mathcal{E}_1} g_1 ds + \int_{\mathcal{E}_2} g_2 ds = 0$. Under these hypotheses it is possible to prove that there exists and it is unique the solution of System (3.8) following the same strategy used for System (3.1).

Remark 14. *In System 3.8, the permittivities of the buffer ε_{ext} and of the cells ε_{int} are of order of $10^{-9} F.m^{-1}$, see Remark 12. Then we assume that the terms $i\,\omega\,\varepsilon_{ext/int}$ are negligible compared to the values $\sigma_{ext/int}$. This implies that the potential u depends on the angular frequency only through the complex parameter $i\omega C_m + S_m$ appearing in the transmission conditions.*

Numerical simulations of System 3.8 and the calibration of the membrane electrical properties with the data are the forthcoming works, which are not included in this thesis due to a lack of time.

3.6 Conclusion and perspectives

Following the set-up of the experiments treated in Chapter 1, we have formalized a problem in which the passive electrode-buffer interfaces are modeled by the FP conditions. Transmission conditions between the buffer domain and the cell

monolayer domain have been written. This problem is well-posed, and its numerical solution reproduces the evolution of the potential inside the plate satisfactorily. For the case without cells, it has been validated by the comparison of (measured and calibrated) impedances obtained from the numerical simulations with (measured and calibrated) impedances obtained with the 4-electrode experiment. This great result confirms that the FP is a robust method to model a system presenting one or more conductors inside. The result also confirms the conductivity estimation, widely used in the calibration strategy in Chapter 1. Finally, we used the calibrated observations to confirm our statement that, in the arranged 4-electrode system used is [20], the sample corresponds to a part of the plate between the passive electrodes. The obtained results are very encouraging. The first perspective of this work concerns the numerical simulations of the system will cells given in (3.8) in order to validate the full strategy with all the available impedance data. The second perspective consists in studying the use of the bioimpedances Z_s^{num} to calibrate (by estimating the parameters A_1, A_2 and A_3) instead of using the theoretical impedance given in Equation (1.25) of Section 1.5 of Chapter 1.

Conclusion and Perspectives

Let us conclude this thesis by a summary of the contributions and the prospectives deriving from the studies applied to the equivalent circuit (EC) model and the floating potential (FP) model in the context of electroporation experiments.

Synthesis

Chapter 1 - Synthesis: This chapter focus on the reproduction and the interpretation of the dataset deriving from an electroporation experiment. The observations are the measures of the impedance of a cell monolayer performed with an arranged 4-electrode setup. The purpose is the analysis of the electrical behavior of cell before and after an electroporating pulse. This work has represented a challenging task from the beginning, *i.e.* the data organization, until the end, *i.e.* the model formalization and the estimation and interpretation of its parameters.

To have a complete overview of the work, it has been fundamental to understand the process of data extraction and the context of the experiments. For this reason, the chapter starts with the introduction of the Electro-quasistatic approximation and the definition of equivalent circuit illustrated on a simple electrical system. The idea is to provide all the notions necessary to understand the topic discussed. It has been necessary to understand deeply the 4-electrode measurement system and the three-reference calibration method, used respectively to measure the cell impedance and to remove the measurement system distortion. Thanks to the acquired knowledge, we have determined the weaknesses of the employed calibration strategy and we have formalized a new more robust strategy, based on more reference measures. This strategy results in a more robust calibration for the considered dataset. The efficacy of the new strategy is proven by the comparison with the theoretical behaviour expected for the observations, given by:

$$Z^{(c)}_{FC,\,t}(\omega) = \frac{k}{\sigma_{(c)} + i\omega\epsilon_{(c)}} \tag{C-1}$$

The new calibrated dataset has been elaborated through an EC model. The EC choice derives from the comprehension of the experiment system. Once the two elements composing the sample (the cells and the buffer) have been identified, their physical analysis has led to the construction of the EC model, represented in Figure C-1 and given by Equations (C-2) and (C-3). A further difficulty has been represented by the non-identifiability of the electrical circuit modeling the set-up. We have addressed this issues by assuming that the cell membrane electrical behavior is not impacted by the conductivity of the buffer. Thus, a reliable definition

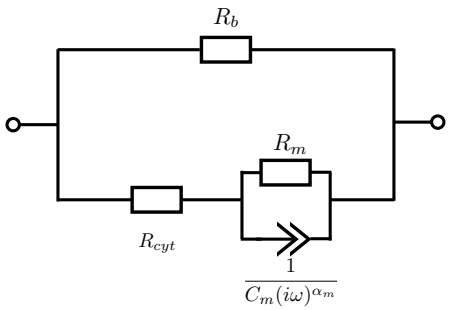

$$Z_{eq}(\omega,\theta) = \frac{R_b\, Z_{cells}(\omega,\theta)}{R_b + Z_{cells}(\omega,\theta)}, \qquad \text{(C-2)}$$

$$Z_{cells}(\omega,\theta) = R_{cyt} + \frac{R_m}{1 + R_m C_m (i\omega)^{\alpha_m}}. \qquad \text{(C-3)}$$

Figure C-1 – EC (cells-buffer system)

of the ranges of the parameters have allowed their estimation. An important role has been played by the distinction of data before and after the pulse, in and with absence of cells. We have also taken into account the different setups (voltage and buffer conductivity) and the time evolutions (for the after pulse data). No less important has been the creation of Matlab code to the resolution of the estimation problem.

The parameter estimation before and after the electroporation pulse give very interesting results as they allow us to understand the impact of the electroporation phenomenon. In particular, the parameters representing the buffer resistance R_b and the membrane resistance R_m decrease in the minutes after the pulse. These evolutions suggest an unusual increase of the buffer-cell exchanges. This observation claims that the applied pulse produces the electroporation of the cell monolayer.

Chapter 1 - Perspectives: As said, the new calibration strategy provides very interesting results but there is room for improvement. We have observed that the employed three-reference calibration strategy is not suitable to the experiment al set-up: the variation of the whole content of the plate does not leave unchanged the measurement system as demanded by the procedure. Then, it would be interesting to define a calibration strategy ideal to this experiment structure and to compare the analysis of the resulting data with the work done.
Moreover, a further data set resulting from a electroporation procedure with a sequence of pulses on the cell monolayer is available. It would be very interesting to apply the same strategy developed in this chapter, in order to validate or improve what has been achieved.
The quantification of this electroporation phenomenon can be done using the values of the parameters: a discussion with biologists is now possible.

Chapter 2 - Synthesis: This chapter concerns the definition of a model to represent the presence of the thin passive electrodes in the experiment presented in Chapter 1. Considering a simpler domain representing the contact zone between electrode and buffer, we have modelled this system thanks to a FP problem. The idea is to consider the electrode as an equipotential surface and its potential as an unknown of the problem. We have proved the existence and uniqueness of the solution of the floating potential problem. This method has been compared with

a classical penalization approach, which has been shown to generate instabilities.

Penalisation Problem	**Floating Potential**	**Convergence**
$\begin{cases} -\nabla \cdot (\sigma^{\varepsilon} \nabla u_{\varepsilon}) = f \quad \text{in} \quad \Omega_i \cup \Omega_e, \\ u_{\varepsilon\vert\Gamma_0{}^I} = u_{\varepsilon\vert\Gamma_0{}^e}, \\ \sigma_i \, \partial_n u_{\varepsilon\vert\Gamma_0{}^I} = \varepsilon^{-k} \sigma_e \, \partial_n u_{\varepsilon\vert\Gamma_0{}^e}, \\ \partial_n u_{\varepsilon\vert\Gamma_{ext}} = 0, \\ u_{\varepsilon\vert\Gamma_{int}} = \gamma, \end{cases}$	$\begin{cases} -\nabla \cdot (\sigma_i \nabla u_0) = f \quad \text{in } \Omega_i, \\ u_{0\vert\Gamma_0} = \alpha_0, \\ \int_{\Gamma_0} \sigma_i \partial_n u_0 \, ds = 0, \\ u_{0\vert\Gamma_{int}} = \gamma. \end{cases}$	$\|u_{\varepsilon} - u_0\|_{H^1(\Omega_i)} \leq c\,\varepsilon$

Thanks to an asymptotic analysis, we have proven the convergence of the two methods:

$$\|u_{\varepsilon} - u_0\|_{H^1(\Omega_i)} \leq c\,\varepsilon,$$

i.e. the solution of the penalization approach u_{ε} converges to the solution u_0 of the FP model. Furthermore, we also have proven the convergence considering the second term approximation u_1, see Section 2.3 for more details.

We have observed that the penalization approach requires an excessively refined mesh and this leads to a high computational cost. Moreover, the use of a very small spatial step causes instability during the resolution. Concerning the FP approach, the main weakness is the fact that its resolution request the resolution of higher number of problems (at maximum $n+2$ if $n+1$ passive electrodes are considered). Nevertheless, all theses problems are Dirichlet problems presenting the same resolution matrix, then it is possible to factorize – if linear solver is used – only once and to solve the systems in parallel. Furthermore, the FP problem does not contain a thin domain then it can be applied to a coarser mesh. As a result, the FP is not time consuming and more robust. Figure C-2 compares the robustness of the these two approaches. Both approaches (penalization and FP) have been numerically solved thanks to the implementation of a C++ Finite Difference Method (FDM) library on 2D cartesian grid.

Chapter 2 - Perspectives: The work done represents a good theoretical basis to model a realistic 4-electrode system as we will see in Chapter 3. An improvement of the accuracy of the solution could be obtained considering a non linear dependence of the conductivities with respect to the electric field.

Chapter 3 - Synthesis: The last chapter connects Chapter 1 and Chapter 2. The FP approach developed on Chapter 2 has been applied to obtain a 2D representation of the arranged four-electrode system in absence of cells and presented in Chapter 1. The formalization of the FP problem with six electrodes has been a challenge. A Gauge condition has to be imposed in order to have the uniqueness of the solution. We assume that $\int_{E_1} u \, dx = 0$ (which means that: $u_{\vert_{E_1}} = \alpha_1 = 0$).

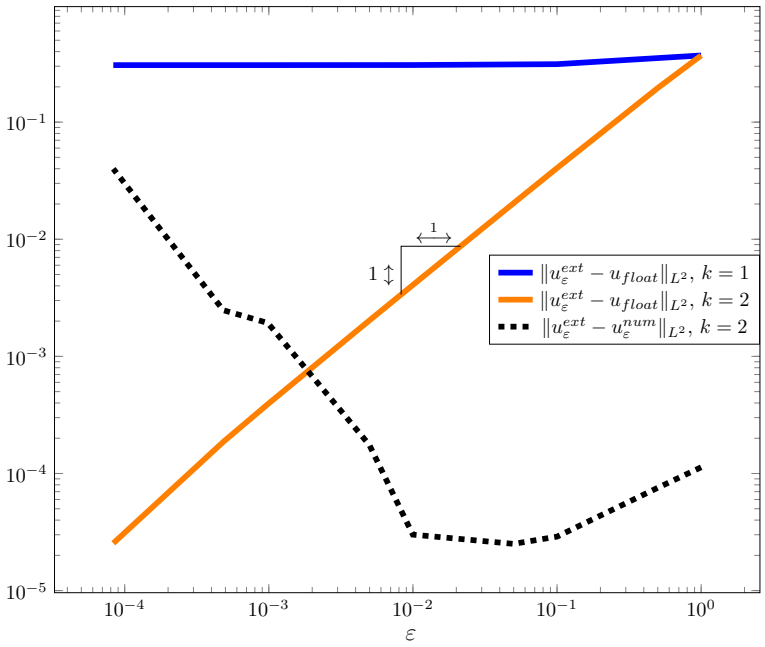

Figure C-2 – $k = 1$: when ε tends to zero, the exact solution does not converge to the *floating potential approach* solution. $k = 2$: the exact solution converges to the *floating potential approach* approximation when ε tends to zero. Due a high *condition number* of the matrix, a direct resolution gives a worse approximation for smaller ε.

Then the model reads: find $(u, \alpha_2, \alpha_3, \alpha_4) \in H^1(\Omega) \times \mathbb{R}^3$ such that,

$$\begin{cases} \nabla \cdot (\sigma \nabla u) = 0, \quad \text{in } \Omega, \\ \sigma \partial_{n_{\mathcal{E}_1}} u_{|\mathcal{E}_1} = g, \qquad \sigma \partial_{n_{\mathcal{E}_2}} u_{|\mathcal{E}_2} = -g, \qquad u_{|E_1} = 0, \\ u_{|E_j} = \alpha_j, \quad j = 2, 3, 4, \\ \displaystyle\int_{E_j} \sigma \partial_{n_{E_j}} u \, ds = 0, \quad j = 2, 3, 4, \\ u_{|L_1} = u_{|L_2}, \\ \sigma \partial_n u = 0 \quad \text{ailleurs.} \end{cases} \tag{C-4}$$

The existence and uniqueness of the solution of the problem have been proved. The resolution – presenting all the advantages of the FP approach – gives a realistic numerical solution of the potential in the buffer. As in Chapter 2, the problem has been numerically solved thanks to a C++ FDM library on a 2D Cartesian grid. Using the numerical solution, we have computed the numerical measured impedance Z_m^{num} as the ratio between the current imposed by the active electrodes and the voltage measured by the passive electrodes, given by

$$Z_m^{num} = \frac{\alpha_2 - \alpha_1}{C_a},$$

σ (S·m^{-1})	Z_s^{num} (Ohm)	$\lvert Z_{FC,cal}(\omega_1)\rvert$ (Ohm)	Err (%)
0.098	610	593	2.8
0.265	204	219	7.3
0.57	114	102	10.5
0.965	62	60	3.2
1.432	40	41	2.5

Table C-1 – Comparison between the impedances Z_s^{num} obtained with the simulations and the impedances calibrated $|Z_{FC,cal}(\omega_1)|$ for various conductivities.

and the numerical sample impedance Z_s^{num} as

$$Z_s^{num} = \frac{\frac{1}{|S_2|}\int_{S_2} u dS - \frac{1}{|S_1|}\int_{S_1} u dS}{\int_{S_1} \sigma \partial_n u dS},$$

where the surfaces S_1 and S_2 are parallel to the vertical sides of Ω and placed between the passive electrodes. The comparison with the impedance data coming from the 4 electrode experiment – see for example Table C-1 for the calibrated ones – allows us to validate:

- the FP model for the arranged 4-electrode measurement system without cells,
- the estimation of the conductivities and of the length of the electrodes,
- the calibration strategy of the measured impedances obtained by the arranged 4-electrode measurement system.

Chapter 3 - Perspectives: The results validate the new calibration strategy developed in this work. Furthermore, this last simulation confirms the assumption done in Chapter 1 which claims that the three-reference method is not suitable to the considered experiment setup. These assumption were based on the fact that the measurement sample is placed between the passive electrode, as confirmed by the surfaces S_1 and S_2. In the same context, a second perspective could be to study the use of the bioimpedances Z_s^{num} to calibrate instead of using the theoretical impedance given in Equation (C-1).

A further support to this result could be derived from the simulation of System 3.8 corresponding to the system with FP conditions coupled with transmissions conditions for the interaction between the buffer and the cells. The resulting simulations could be compared with the observations with cell of this dataset or with the observations present in the "multi-pulse" dataset.

Appendix A

Towards the limit problems

A.1 Limit problem for $k = 1$

Using the same methodology given in Appendix A.2, the limit problem for $k = 1$ is

$$\boxed{\begin{aligned} -\Delta u_0^i &= \tfrac{f}{\sigma_i} \quad \text{in } \Omega_i, \\ \partial_n u_0^i|_{\Gamma_0} &= \bar{\sigma}\Delta_{\Gamma_0} u_0^i, \\ u_0^i|_{\Gamma_{int}} &= \gamma. \end{aligned}} \tag{A-1}$$

This problem does not give a realistic behaviour: when ε tends to zero, in the part of boundary occupied by the electrode, the value of the voltage does not converge to a constant value, as expected from the electromagnetism theory.

A.2 Detailed calculations of the elementary problems for k=2

1st Order Limit Problem

Goal of this section is to show the problem satisfied by u_0^i. For this reason we have to see which properties are valid for u_0^i starting from the p-th order problem (2.13).
The 0 order problem is

$$\boxed{-\nabla \cdot (\sigma_i \nabla u_0^i) = f \quad \text{in } \Omega_i}, \tag{A-2}$$

$$\partial_\eta^2 u_0^e = 0 \quad \text{in } \Gamma_0 \times (0,1), \tag{A-3}$$

$$u_0^i|_{\Gamma_0} = u_0^e|_{\eta=0}, \tag{A-4}$$

$$\partial_\eta u_0^e|_{\eta=0} = 0, \tag{A-5}$$

$$\partial_\eta u_0^e|_{\eta=1} = 0, \tag{A-6}$$

$$\boxed{u_0^i|_{\Gamma_{int}} = \gamma}. \tag{A-7}$$

From (A-3)

$$u_0^e(x_T, \eta) = \alpha_0^e(x_T) + \beta_0^e(x_T)\eta,$$

and, with (A-5), gives $\beta_0^e(x_T) = 0$. Hence

$$u_0^e(x_T, \eta) = \alpha_0^e(x_T).$$

u_0^e is not a function of η and depends only on x_T.
The 1-st order problem is

$$-\nabla \cdot (\sigma_i \nabla u_1^i) = 0 \quad \text{in } \Omega_i, \tag{A-8}$$
$$\partial_\eta^2 u_1^e = -a_{33}^0 \partial_\eta u_0^e \quad \text{in } \Gamma_0 \times (0,1), \tag{A-9}$$
$$u_1^i|_{\Gamma_0} = u_1^e|_{\eta=0}, \tag{A-10}$$
$$\partial_\eta u_1^e|_{\eta=0} = 0, \tag{A-11}$$
$$\partial_\eta u_1^e|_{\eta=1} = 0, \tag{A-12}$$
$$u_1^i|_{\Gamma_{int}} = 0. \tag{A-13}$$

As seen in the previous case, u_0^e is not a function of η: (A-9) becomes

$$\partial_\eta^2 u_1^e = 0 \quad \text{in } \Gamma_0 \times (0,1),$$

and making the same reasoning made before about u_0^e using also (A-11) it easy to get

$$u_1^e(x_T, \eta) = \alpha_1^e(x_T),$$

u_1^e is only a function of x_T and not of η.
The 2-nd order problem is

$$-\nabla \cdot (\sigma_i \nabla u_2^i) = 0 \quad \text{in } \Omega_i, \tag{A-14}$$
$$\partial_\eta^2 u_2^e = -a_{33}^0 \partial_\eta u_1^e - \eta a_{33}^1 \partial_\eta u_0^e - S_{\Gamma_0}^0 u_0^e \quad \text{in } \Gamma_0 \times (0,1), \tag{A-15}$$
$$u_2^i|_{\Gamma_0} = u_2^e|_{\eta=0}, \tag{A-16}$$
$$\partial_\eta u_2^e|_{\eta=0} = 0, \tag{A-17}$$
$$\partial_\eta u_2^e|_{\eta=1} = 0, \tag{A-18}$$
$$u_i^2|_{\Gamma_{int}} = 0. \tag{A-19}$$

As seen in the previous cases, u_0^e and u_1^e depend only on x_T: (A-15) becomes

$$\partial_\eta^2 u_2^e = -S_{\Gamma_0}^0 u_0^e(x_T).$$

Remark 9 brings to

$$\partial_\eta^2 u_2^e = -\Delta_{\Gamma_0} u_0^e(x_T).$$

Since $-\Delta_{\Gamma_0} u_0^e(x_T)$ does not depend on η, it is easy to get the result

$$u_2^e(x_T, \eta) = \alpha_2^e(x_T) + \beta_2^e(x_T)\eta - \frac{\eta^2}{2}\Delta_{\Gamma_0} u_0^e(x_T).$$

Passing to considering the first derivative respect to η

$$\partial_\eta u_2^e(x_T, \eta) = \beta_2^e(x_T) - \eta \Delta_{\Gamma_0}^0 u_0^e,$$

(A-17) leads to

$$\beta_2^e(x_T) = 0;$$

and so using (A-18) it is possible to deduce

$$\Delta_{\Gamma_0} u_0^e = \beta_2^e(x_T) = 0.$$

Last two results bring to say that

— u_2^e is a function only of x_T

$$u_2^e(x_T, \eta) = \alpha_2^e(x_T);$$

— applying the Laplace operator on the surface Γ_0, Δ_{Γ_0}, to u_0^e gives 0. This meas that u_0^e is constant along the local coordinates x_T of the surface Γ_0, easy to show integrating by parts $\Delta_{\Gamma_0} u_0^e$ in Γ_0:

$$u_0^e(x_T, \eta) = \bar{\alpha}_0^e \in \mathbb{R}.$$

To simplify, will note $\bar{\alpha}_0^e = \alpha_0$.

(A-4) leads to

$$\boxed{u_0^i|_{\Gamma_0} = \alpha_0 \in \mathbb{R}}. \tag{A-20}$$

The 3-rd order problem is

$$\begin{aligned}
-\nabla \cdot (\sigma_i \nabla u_3^i) &= 0 \quad \text{in } \Omega_i, && \text{(A-21)}\\
\partial_\eta^2 u_3^e &= -a_{33}^0 \partial_\eta u_2^e - \left(\eta a_{33}^1 \partial_\eta u_1^e + S_{\Gamma_0}^0 u_1^e\right) \\
&\quad -\eta \left(\frac{\eta}{2} a_{33}^2 \partial_\eta u_0^e + S_{\Gamma_0}^1 u_0^e\right) \quad \text{in } \Gamma_0 \times (0,1), && \text{(A-22)}\\
u_3^i|_{\Gamma_0} &= u_3^e|_{\eta=0}, && \text{(A-23)}\\
\sigma_i \partial_n u_0^i|_{\Gamma_0} &= \sigma_e \partial_\eta u_3^e|_{\eta=0}, && \text{(A-24)}\\
\partial_\eta u_3^e|_{\eta=1} &= 0, && \text{(A-25)}\\
u_i^3|_{\Gamma_{int}} &= 0. && \text{(A-26)}
\end{aligned}$$

Taking into account what already saw in the previous cases, u_0^e is a constant and u_1^e and u_2^e are function only of local coordinates of Γ_0. So (A-22) becomes

$$\partial_\eta^2 u_3^e = -S_{\Gamma_0}^0 u_1^e \quad \text{in } \Gamma_0 \times (0,1).$$

Integrating respect to η and using Remark 9

$$\partial_\eta u_3^e = -\eta \Delta_{\Gamma_0} u_1^e + \beta_3^e(x_T).$$

From (A-25)

$$\beta_3^e(x_T) = \Delta_{\Gamma_0} u_1^e,$$

and so

$$\partial_\eta u_3^e = (1-\eta)\Delta_{\Gamma_0} u_1^e. \tag{A-27}$$

Using this result, (A-24) becomes

$$\sigma_i \partial_n u_{0|_{\Gamma_0}}^i = \sigma_e \Delta_{\Gamma_0} u_1^e.$$

Remark 15. *The integration on closed surface* Γ *of Laplace surface operator* Δ_Γ *gives 0. This is easy to proof by integrating by parts.*

From **Remark 15**, we get

$$\boxed{\int_{\Gamma_0} \sigma_i \partial_n u_0^i \, ds = 0} \tag{A-28}$$

In conclusion the limit problem determining u_0^i is given by (A-2), (A-7), (A-20) and (A-28), so

$$\boxed{\begin{aligned} &-\nabla \cdot (\sigma_i \nabla u_0^i) = f \quad \text{in } \Omega_i, \\ &u_0^i|_{\Gamma_0} = \alpha_0, \\ &\int_{\Gamma_0} \sigma_i \partial_n u_0^i \, ds = 0, \\ &u_0^i|_{\Gamma_{int}} = \gamma. \end{aligned}} \tag{A-29}$$

2nd Order Limit Problem

Goal of this section is to show the problem satisfied by u_1^i. For this reason we have to see which properties are valid for u_0^i starting from the p-th order problem (2.13).
For $p = 1$, System (A-8)-(A-13) gives the equations:

$$\boxed{-\nabla \cdot \left(\sigma_i \nabla u_1^i\right) = 0 \quad \text{in} \quad \Omega_i}, \tag{A-30}$$

$$\boxed{u_{1|\Gamma_{int}}^i = 0}. \tag{A-31}$$

Moreover, as already shown, from (A-9) it is possible to get that u_1^e is only a function of x_T and not of η:

$$u_1^e(x_T, \eta) = \alpha_1^e(x_T).$$

So from (A-10)

$$u_1^i|_{\Gamma_0} = \alpha_1^e(x_T).$$

From System (A-21)-(A-24) we obtain

$$\sigma_e \Delta_{\Gamma_0} u_1^e = \sigma_i \partial_n u_0^i|_{\Gamma_0},$$

and since it possible to compute u_0^i from (A-29), u_1^e is define, up to an additive constant, then

$$u_1^e = \bar{u}_1^e + \alpha_1,$$

and so from (A-10)

$$\boxed{u_{1|\Gamma_0}^i = \bar{u}_1^e + \alpha_1}, \tag{A-32}$$

where $\bar{u}_1^e$ is solution of

$$\sigma_e \Delta_{\Gamma_0} \bar{u}_1^e = \sigma_i \partial_n u_0^i|_{\Gamma_0},$$
$$\int_{\Gamma_0} \bar{u}_1^e = 0.$$

The 4-th order problem is

$$\begin{aligned}
-\nabla \cdot \left(\sigma_i \nabla u_4^i\right) &= 0 \quad \text{in } \Omega_i, && \text{(A-33)}\\
\partial_\eta^2 u_4^e &= -a_{33}^0 \partial_\eta u_3^e - \left(\eta a_{33}^1 \partial_\eta u_2^e + S_{\Gamma_0}^0 u_2^e\right) \\
&\quad -\eta \left(\frac{\eta}{2} a_{33}^2 \partial_\eta u_1^e + S_{\Gamma_0}^1 u_1^e\right) \\
&\quad -\frac{\eta^2}{2}\left(\frac{\eta}{3} a_{33}^3 \partial_\eta u_0^e + S_{\Gamma_0}^2 u_0^e\right) \quad \text{in } \Gamma_0 \times (0,1), && \text{(A-34)}\\
u_4^i|_{\Gamma_0} &= u_4^e|_{\eta=0}, && \text{(A-35)}\\
\sigma_i \partial_n u_1^i|_{\Gamma_0} &= \sigma_e \partial_\eta u_4^e|_{\eta=0}, && \text{(A-36)}\\
\partial_\eta u_4^e|_{\eta=1} &= 0, && \text{(A-37)}\\
u_4^i|_{\Gamma_{int}} &= 0. && \text{(A-38)}
\end{aligned}$$

Considering only the no-zero elements, (A-34) becomes

$$\partial_\eta^2 u_4^e = -a_{33}^0 \partial_\eta u_3^e - S_{\Gamma_0}^0 u_2^e - \eta S_{\Gamma_0}^1 u_1^e \quad \text{in } \Gamma_0 \times (0,1).$$

Then integrating along η direction in $[0,1]$

$$\int_0^1 \partial_\eta^2 u_4^e \, d\eta = -a_{33}^0 \left(u_3^e(x_T,1) - u_3^e(x_T,0)\right) - \Delta_{\Gamma_0} u_2^e(x_T) - \frac{1}{2} S_{\Gamma_0}^1 u_1^e(x_T) \quad \text{in } \Gamma_0.$$

Remembering that

$$\int_0^1 \partial_\eta^2 u_4^e = \partial_\eta u_{4|\eta=1}^e - \partial_\eta u_{4|\eta=0}^e,$$

using also (A-37), it is easy to get

$$\partial_\eta u_{4|\eta=0}^e = a_{33}^0 \left(u_3^e(x_T,1) - u_3^e(x_T,0)\right) + \Delta_{\Gamma_0} u_2^e(x_T) + \frac{1}{2} S_{\Gamma_0}^1 u_1^e(x_T) \quad \text{in } \Gamma_0.$$

From (A-36) follows

$$\sigma_i \partial_n u_{1|\Gamma_0}^i = \sigma_e \, a_{33}^0 \left(u_3^e(x_T,1) - u_3^e(x_T,0)\right) + \sigma_e \Delta_{\Gamma_0} u_2^e(x_T) + \frac{1}{2} \sigma_e S_{\Gamma_0}^1 u_1^e(x_T).$$

Observing that, from (A-27), we have

$$\int_{\Gamma_0} \left(u_3^e(x_T,1) - u_3^e(x_T,0)\right) = \frac{1}{2} \int_{\Gamma_0} \Delta_{\Gamma_0} u_1^e(x_T) = 0,$$

and observing that

$$\int_{\Gamma_0} S_{\Gamma_0}^1 u_1^e(x_T) = 0,$$

recalling **Remark 15**, the integration on Γ_0 of every element of right-hand term in previously equality is equal to zero. Then

$$\boxed{\int_{\Gamma_0} \sigma_i \partial_n u^i_{1|_{\Gamma_0}} = 0}. \tag{A-39}$$

Finally (A-30), (A-32), (A-39) and (A-31) give the problem satisfied by u^i_1:

$$\boxed{\begin{aligned} &-\nabla \cdot \left(\sigma_i \nabla u^i_1\right) = 0 \quad \text{in} \quad \Omega_i, \\ &u^i_{1|\Gamma_0} = \bar{u}^e_1 + \alpha_1, \\ &\int_{\Gamma_0} \sigma_i \, \partial_n u^i_{1|_{\Gamma_0}} = 0, \\ &u^i_{1|_{\Gamma_{int}}} = 0, \end{aligned}} \tag{A-40}$$

with $\bar{u}^e_1$ solution of

$$\boxed{\begin{aligned} &\sigma_e \Delta_{\Gamma_0} \bar{u}^e_1 = \sigma_i \partial_n u^i_0|_{\Gamma_0}, \\ &\int_{\Gamma_0} \bar{u}^e_1 = 0. \end{aligned}} \tag{A-41}$$

Appendix B

Floating potential in volume electrode

B.1 Floating potential

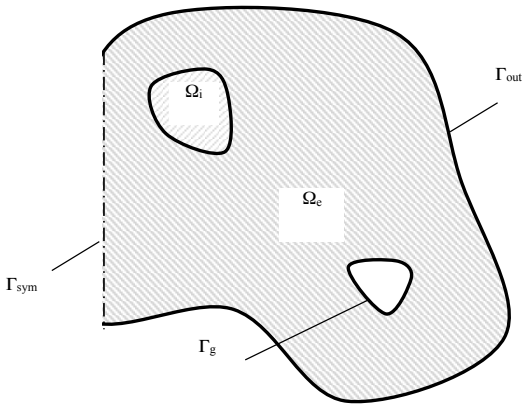

Figure B-3 – Representations of two different 4-electrode systems in a tissue that gives rise two *floating potential* problem.

In this section we present the model, treated in [51], of a 4-electrode system dedicated to measure the impedance of a biological tissue. In this device, a current is injected through both external electrodes inside the biological tissue. In the same time, both internal electrodes are connected to a high impedance in the external circuit; as a consequence, no current is supposed to flow through them. The impedance of the biological tissue is then calculated measuring the potential difference induced between the internal electrodes. The general model of a symmetric 4-electrode system with two pairs of active and passive electrodes is shown in Figure B-3. In this system the size is not negletible respect to the total domain size. An asymptotic expansion of the solution is considered. The small parameter of the expansion here is the ratio of conductivities.

The initial problem to solve reads:

$$\begin{cases} -\nabla\cdot(\sigma_{\mathrm{e}}\nabla\varphi_{\mathrm{e}}) = 0, \quad \text{in} \quad \Omega_{\mathrm{e}}, \\ \varphi_{\mathrm{e}|_{\Gamma_{\mathrm{g}}}} = V, \quad \varphi_{\mathrm{e}|_{\Gamma_{\mathrm{sym}}}} = 0, \quad \sigma_{\mathrm{e}}\partial_n\varphi_{\mathrm{e}|_{\Gamma_{\mathrm{out}}}} = 0, \\ -\nabla\cdot(\sigma_{\mathrm{i}}\nabla\varphi_{\mathrm{i}}) = 0, \quad \text{in} \quad \Omega_{\mathrm{i}}, \\ \varphi_{\mathrm{e}|_{\partial\Omega_{\mathrm{i}}}} = \varphi_{\mathrm{i}|_{\partial\Omega_{\mathrm{i}}}}, \quad \sigma_{\mathrm{e}}\partial_n\varphi_{\mathrm{e}|_{\partial\Omega_{\mathrm{i}}}} = \sigma_{\mathrm{i}}\partial_n\varphi_{\mathrm{i}|_{\partial\Omega_{\mathrm{i}}}}. \end{cases} \tag{B-1}$$

where Γ_g is the border for the active electrode, Γ_{out} the external border of the biological tissue and Γ_{sym} the symmetry plane. σ_e is the conductivity of the biological tissue defined inside the domain Ω_e and σ_i the conductivity of the passive electrodes defined inside the domains Ω_i.
The solution for φ_e and φ_i can be expanded using formal series with respect to the parameter $\varepsilon = \dfrac{\sigma_e}{\sigma_i} \ll 1$:

$$\begin{cases} \varphi_{\mathrm{e}} = \varphi_{\mathrm{e}}^0 + \varepsilon\varphi_{\mathrm{e}}^1 + \cdots \\ \varphi_{\mathrm{i}} = \alpha_0 + \varepsilon(\varphi_{\mathrm{i}}^1 + \alpha_1) + \cdots \end{cases}$$

where the terms α_k are constant and $\{{\varphi_i}^k, {\varphi_e}^k\}$ solve a differential problem set respectively in Ω_i and Ω_e. Identifying the terms with the same power in ε, we infer the cascade of problems. The first problem to solve appears to be perfect conductor case. The couple $({\varphi_e}^0, \alpha_0)$ is the solution to

$$\begin{cases} -\nabla\cdot(\sigma_{\mathrm{e}}\nabla\varphi_{\mathrm{e}}^0) = 0, \quad \text{in} \quad \Omega_{\mathrm{e}}, \\ \varphi^0_{\mathrm{e}|_{\Gamma_{\mathrm{g}}}} = V, \quad \varphi^0_{\mathrm{e}|_{\Gamma_{\mathrm{sym}}}} = 0, \quad \sigma_{\mathrm{e}}\partial_n\varphi^0_{\mathrm{e}|_{\Gamma_{\mathrm{out}}}} = 0, \\ \varphi_{\mathrm{e}|_{\partial\Omega_{\mathrm{i}}}} = \alpha_0, \quad \text{with } \alpha_0 \text{ such that} \quad \displaystyle\int_{\partial\Omega_{\mathrm{i}}} \sigma_{\mathrm{e}}\partial_n\varphi_{\mathrm{e}}^0 = 0. \end{cases} \tag{B-2}$$

The solution $({\varphi_e}^0, \alpha_0)$ is computed by superposing two solutions of problems where the homogeneous Dirichlet condition is set respectively on the boundary $\partial\Omega_i$ of the passive electrode and on the boundary Γ_g of the active electrode. More precisely, consider the two following problems

$$\begin{cases} -\nabla\cdot(\sigma_{\mathrm{e}}\nabla\lambda) = 0, \quad \text{in} \quad \Omega_{\mathrm{e}}, \\ \lambda_{|_{\Gamma_{\mathrm{g}}}} = V, \quad \lambda_{|_{\Gamma_{\mathrm{sym}}}} = 0, \quad \sigma_{\mathrm{e}}\partial_n\lambda_{|_{\Gamma_{\mathrm{out}}}} = 0, \\ \lambda_{|_{\partial\Omega_{\mathrm{i}}}} = 0 \end{cases}$$

$$\begin{cases} -\nabla\cdot(\sigma_{\mathrm{e}}\nabla\mu) = 0, \quad \text{in} \quad \Omega_{\mathrm{e}}, \\ \mu_{|_{\Gamma_{\mathrm{g}}\cup\Gamma_{\mathrm{out}}}} = 0, \quad \sigma_{\mathrm{e}}\partial_n\mu_{|_{\Gamma_{\mathrm{out}}}} = 0, \\ \mu_{|_{\partial\Omega_{\mathrm{i}}}} = 1. \end{cases}$$

Then the solution ${\varphi_e}^0 = \lambda + \alpha_0\,\mu$, in Ω_e and ${\varphi_i}^0 = \alpha_0$ in Ω_i, with

$$\alpha_0 = -\frac{\displaystyle\int_{\partial\Omega_{\mathrm{i}}} \sigma_{\mathrm{e}}\nabla\lambda\cdot\nabla\mu\,dx}{\displaystyle\int_{\partial\Omega_{\mathrm{i}}} \sigma_{\mathrm{e}}|\nabla\mu|^2\,dx}. \tag{B-3}$$

To improve the zero order solution it is possible to compute the terms $\{{\varphi_i}^1, {\varphi_e}^1, \alpha_1\}$ by solving:

$$\begin{cases} -\nabla \cdot (\sigma_{\mathrm{i}} \nabla \varphi_{\mathrm{i}}^1) = 0, \quad \text{in} \quad \Omega_{\mathrm{i}}, \\ \sigma_{\mathrm{i}} \partial_n \varphi^1_{\mathrm{i}|_{\partial\Omega_{\mathrm{i}}}} = \sigma_{\mathrm{e}} \partial_n \varphi^0_{\mathrm{e}|_{\partial\Omega_{\mathrm{i}}}}, \quad \displaystyle\int_{\partial\Omega_{\mathrm{i}}} \varphi_{\mathrm{i}}^1 \, ds = 0, \end{cases} \tag{B-4}$$

$$\begin{cases} -\nabla \cdot (\sigma_{\mathrm{e}} \nabla \varphi_{\mathrm{e}}^1) = 0, \quad \text{in} \quad \Omega_{\mathrm{e}}, \\ \varphi^1_{\mathrm{e}|_{\Gamma_{\mathrm{g}}}} = 0, \quad \varphi^1_{\mathrm{e}|_{\Gamma_{\mathrm{sym}}}} = 0, \quad \sigma_{\mathrm{e}} \partial_n \varphi^0_{\mathrm{e}|_{\Gamma_{\mathrm{out}}}} = 0, \\ \varphi^1_{\mathrm{e}|_{\partial\Omega_{\mathrm{i}}}} = \varphi^1_{\mathrm{i}|_{\partial\Omega_{\mathrm{i}}}}, \quad \text{with } \alpha_1 \text{ such that } \displaystyle\int_{\partial\Omega_{\mathrm{i}}} \sigma_{\mathrm{e}} \partial_n \varphi_{\mathrm{e}}^1 = 0. \end{cases} \tag{B-5}$$

The terms $\{{\varphi_i}^1, {\varphi_e}^1, \alpha_1\}$ satisfy problems similar as System (B-2). The numerical problem (B-4) is solved using a Lagrange multiplier to ensure the Gauge condition. Instead of solving (B-5), one solves

$$\begin{cases} -\nabla \cdot (\sigma_{\mathrm{e}} \nabla \chi) = 0, \quad \text{in} \quad \Omega_{\mathrm{e}}, \\ \chi_{|_{\Gamma_{\mathrm{g}} \cup \Gamma_{\mathrm{out}}}} = 0, \quad \sigma_{\mathrm{e}} \partial_n \chi_{|_{\Gamma_{\mathrm{out}}}} = 0, \\ \chi_{|_{\partial\Omega_{\mathrm{i}}}} = 1. \end{cases}$$

The constant α_1 is given by substituting λ by χ in (B-3). The first order correction is then given by ${\varphi_e}^1 = \chi + \alpha_1 \, \mu$ in Ω_e.

B.2 Numerical results

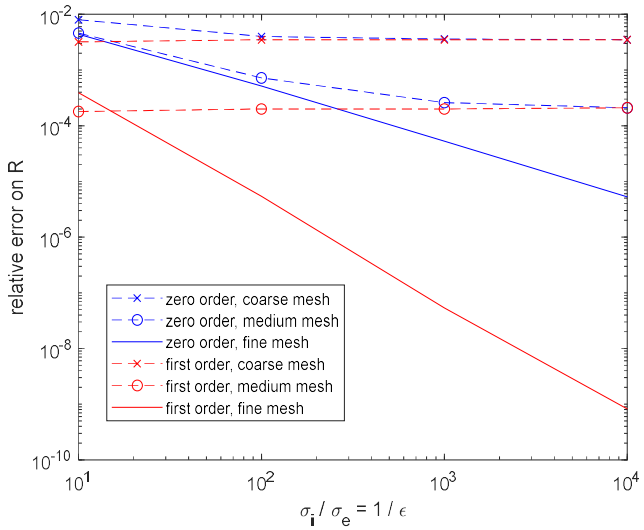

Figure B-4 – Convergence of the asymptotic approach at the zero and first orders for three different meshes with the 2D model.

A 2D model of a symmetric 4-electrode system is first introduced in order to perform the convergence study. The problem is solved using the Finite Element

Method (FEM) method with a coarse, medium and fine meshes. A 4-electrode device is designed to measure the resistance R defined as the ratio of the potential difference U between the passive electrode and the current I flowing through the active electrodes. Then the resistance R can be computed using an explicit formula based on the potentials φ_e and φ_i:

$$R = \frac{U}{I} = \frac{2}{|\partial\Omega_{\mathrm{i}}|} \frac{\int_{\partial\Omega_{\mathrm{i}}} \varphi_{\mathrm{i}}\, ds}{\int_{\Gamma_g} \sigma_{\mathrm{e}} \varphi_{\mathrm{e}}\, ds}.$$

To perform the convergence study, the numerical solution of the direct computation of (B-1) and the numerical solution obtained with the asymptotic method are compared. See Figure B-4. One observes that when the asymptotic method is performed with the fine mesh, the approximation of R for the zero order computation, that depends only on the couple $({\varphi_e}^0, \alpha_0)$, has accuracy order of the rate ε. Adding the first order correction, depending also on $({\varphi_e}^1, \alpha_1)$, the accuracy increases at order ε^2. Those observations are in agreement with the theoretical result. In fact using the asymptotic expansion, R is approached by

$$R = \frac{2V}{|\partial\Omega_{\mathrm{i}}| \int_{\Omega_{\mathrm{e}}} |\nabla\varphi_{\mathrm{e}}^0|^2\, dx} \left\{ \alpha_0 + \varepsilon \left(\alpha_1 - 2\alpha_0 \frac{\int_{\Omega_{\mathrm{e}}} \sigma_{\mathrm{e}} \nabla\varphi_{\mathrm{e}}^0 \cdot \nabla\varphi_{\mathrm{e}}^1}{\int_{\Omega_{\mathrm{e}}} \sigma_{\mathrm{e}} |\nabla\varphi_{\mathrm{e}}^0|^2\, dx} \right) \right\} + O(\varepsilon^2).$$

However, when the mesh is too coarse, the accuracy of the FEM solution is not sufficient enough and the error due to the mesh is greater than the error due to the truncation of the asymptotic expansion. A 3D model of the symmetric 4-electrode system has been simulated in order to get closer to the real device. The comparison cannot be performed further because of the limitation of the numerical resources. Moreover, the matrix of the entire problem becomes numerically singular due to the high contrast of conductivities and the numerical inversion is not accurate.
In conclusion an asymptotic approach has been proposed to solve the problem of floating potentials that present a high conductivity compared to the ambient medium but a not negligible domain size, unlike then the *thin film problem*. The convergence study shows that this approach enables to improve the accuracy of the solution where perfect conductors are assumed. Compared to the direct solution, the advantage of the asymptotic approach is that less numerical resources are required since the floating conductors are meshed in a distinct problem. Another advantage of the asymptotic approach is that it avoids numerical artifacts that appear with the direct solution when the contrast of conductivity is too large. Nonlinear problems can also be solved numerically using the asymptotic method.

Bibliography

[1] I. Abidor, V. Arakelyan, L. Chernomordik, Y. A. Chizmadzhev, V. Pastushenko, and M. Tarasevich. Electric breakdown of bilayer lipid membranes: I. the main experimental facts and their qualitative discussion. *Journal of electroanalytical chemistry and interfacial electrochemistry*, 104:37–52, 1979.

[2] B. Alberts, A. Johnson, J. Lewis, M. Raff, K. Roberts, and P. Walter. Ion channels and the electrical properties of membranes. In *Molecular Biology of the Cell. 4th edition*. Garland Science, 2002.

[3] B. Alberts, A. Johnson, J. Lewis, M. Raff, K. Roberts, and P. Walter. The molecular biology of the cell. garland publ. *Inc., London*, 2002.

[4] D. Amann, A. Blaszczyk, G. Of, and O. Steinbach. Simulation of floating potentials in industrial applications by boundary element methods. *Journal of Mathematics in Industry*, 4(1):13, 2014.

[5] J.-Z. Bao, C. C. Davis, and R. E. Schmukler. Impedance spectroscopy of human erythrocytes: system calibration, and nonlinear modeling. *IEEE Transactions on biomedical engineering*, 40(4):364–378, 1993.

[6] A. J. Bard, L. R. Faulkner, et al. Fundamentals and applications. *Electrochemical Methods*, 2(482):580–632, 2001.

[7] A. J. Bard, L. R. Faulkner, J. Leddy, and C. G. Zoski. *Electrochemical methods: fundamentals and applications*, volume 2. wiley New York, 1980.

[8] R. Benz, F. Beckers, and U. Zimmermann. Reversible electrical breakdown of lipid bilayer membranes: a charge-pulse relaxation study. *The Journal of membrane biology*, 48(2):181–204, 1979.

[9] R. A. Capaldi. The structure of erythrocyte membranes: a partial separation of intrinsic and extrinsic membrane proteins. *European Journal of Biochemistry*, 29(1):74–79, 1972.

[10] G. Cevc. Membrane electrostatics. *Biochimica et Biophysica Acta (BBA)-Reviews on Biomembranes*, 1031(3):311–382, 1990.

[11] C. Chen, S. Smye, M. Robinson, and J. Evans. Membrane electroporation theories: a review. *Medical and Biological Engineering and Computing*, 44(1-2):5–14, 2006.

[12] J. Claudel. *Spectroscopie d'impédance électrique par biocapteur à microélectrodes: application à la cytométrie de flux de cellules sanguines*. PhD thesis, Université de Lorraine, 2013.

[13] A. R. Conn, N. I. Gould, and P. L. Toint. *Trust region methods*. SIAM, 2000.

[14] F.-X. Contreras, L. Sánchez-Magraner, A. Alonso, and F. M. Goñi. Transbilayer (flip-flop) lipid motion and lipid scrambling in membranes. *FEBS letters*, 584(9):1779–1786, 2010.

[15] J. M. Crowley. Electrical breakdown of bimolecular lipid membranes as an electromechanical instability. *Biophysical journal*, 13(7):711, 1973.

[16] R. V. Davalos, L. Mir, and B. Rubinsky. Tissue ablation with irreversible electroporation. *Annals of biomedical engineering*, 33(2):223, 2005.

[17] F. Drake, G. Pierce, and M. Dow. Measurement of the dielectric constant and index of refraction of water and aqueous solutions of kcl at high frequencies. *Physical Review*, 35(6):613, 1930.

[18] R. P. Feynman. Feynman lectures on physics. volume 2: Mainly electromagnetism and matter. *Reading, Ma.: Addison-Wesley, 1964, edited by Feynman, Richard P.; Leighton, Robert B.; Sands, Matthew*, 1964.

[19] O. Gallinato, B. D. de Senneville, O. Seror, and C. Poignard. Numerical workflow of irreversible electroporation for deep-seated tumor. *Physics in Medicine & Biology*, 64(5):055016, 2019.

[20] T. García-Sánchez, A. Azan, I. Leray, J. Rosell-Ferrer, R. Bragos, and L. M. Mir. Interpulse multifrequency electrical impedance measurements during electroporation of adherent differentiated myotubes. *Bioelectrochemistry*, 105:123–135, 2015.

[21] T. Garcia-Sanchez, D. Voyer, C. Poignard, and L. MIRr. Physiological changes may dominate the electrical properties of liver during electroporation. Submitted.

[22] A. Golberg, J. Fischer, and B. Rubinsky. The use of irreversible electroporation in food preservation. In *irreversible electroporation*, pages 273–312. Springer, 2010.

[23] T. Harayama and H. Riezman. Understanding the diversity of membrane lipid composition. *Nature Ecology & Evolution*, pages 1–18, 2018.

[24] S. Ho and G. S. Mittal. Electroporation of cell membranes: a review. *Critical reviews in biotechnology*, 16(4):349–362, 1996.

[25] P. B. Ishai, M. S. Talary, A. Caduff, E. Levy, and Y. Feldman. Electrode polarization in dielectric measurements: a review. *Measurement Science and Technology*, 24(10):102001, 2013.

[26] A. Ivorra, B. Al-Sakere, B. Rubinsky, and L. M. Mir. In vivo electrical conductivity measurements during and after tumor electroporation: conductivity changes reflect the treatment outcome. *Physics in Medicine & Biology*, 54(19):5949, 2009.

[27] J. D. Jackson. From lorenz to coulomb and other explicit gauge transformations. *American Journal of Physics*, 70(9):917–928, 2002.

[28] A. Konrad and M. Graovac. The finite element modeling of conductors and floating potentials. *IEEE Transactions on magnetics*, 32(5):4329–4331, 1996.

[29] M. Leguebe, A. Silve, L. M. Mir, and C. Poignard. Conducting and permeable states of cell membrane submitted to high voltage pulses: mathematical and

numerical studies validated by the experiments. *Journal of theoretical biology*, 360:83–94, 2014.

[30] V. Lvovich. Impedance spectroscopy: Applications to electrochemical and dielectric phenomena. 2012.

[31] P. Malmivuo, J. Malmivuo, and R. Plonsey. *Bioelectromagnetism: principles and applications of bioelectric and biomagnetic fields*. Oxford University Press, USA, 1995.

[32] E. McAdams and J. Jossinet. Tissue impedance: a historical overview. *Physiological measurement*, 16(3A):A1, 1995.

[33] L. Miller, J. Leor, and B. Rubinsky. Cancer cells ablation with irreversible electroporation. *Technology in cancer research & treatment*, 4(6):699–705, 2005.

[34] L. M. Mir, S. Orlowski, J. Belehradek, and C. Paoletti. Electrochemotherapy potentiation of antitumour effect of bleomycin by local electric pulses. *European Journal of Cancer and Clinical Oncology*, 27(1):68 – 72, 1991.

[35] T. Murphy and E. Cohen. Corrections to the fuoss–onsager theory of electrolytes. *The Journal of Chemical Physics*, 53(6):2173–2186, 1970.

[36] E. Neumann and K. Rosenheck. Permeability changes induced by electric impulses in vesicular membranes. *The Journal of membrane biology*, 10(1):279–290, 1972.

[37] E. Neumann, M. Schaefer-Ridder, Y. Wang, and P. Hofschneider. Gene transfer into mouse lyoma cells by electroporation in high electric fields. *The EMBO journal*, 1(7):841–845, 1982.

[38] R. Perrussel and C. Poignard. Asymptotic expansion of steady-state potential in a high contrast medium with a thin resistive layer. *Applied Mathematics and Computation*, 221:48–65, 2013.

[39] A. Ramahi and R. Ruff. Membrane potential. 2014.

[40] F. Sachse. *Computational Cardiology: Modeling of Anatomy, Electrophysiology and Mechanics*. Springer-Verlag, 2004.

[41] S. Salsa. *Partial differential equations in action: from modelling to theory*, volume 99. Springer, 2016.

[42] H. Schwan. Alternating current electrode polarization. *Biophysik*, 3(2):181–201, 1966.

[43] H. P. Schwan and C. D. Ferris. Four-electrode null techniques for impedance measurement with high resolution. *Review of scientific instruments*, 39(4):481–485, 1968.

[44] J. Shi, Y. Ma, J. Zhu, Y. Chen, Y. Sun, Y. Yao, Z. Yang, and J. Xie. A review on electroporation-based intracellular delivery. *Molecules*, 23(11):3044, 2018.

[45] B. H. Shilton. Active transporters as enzymes: an energetic framework applied to major facilitator superfamily and abc importer systems. *Biochemical Journal*, 467(2):193–199, 2015.

[46] S. J. Singer and G. L. Nicolson. The fluid mosaic model of the structure of cell membranes. *Science*, 175(4023):720–731, 1972.

[47] R. Stampfli. Reversible electrical breakdown of the excitable membrane of a ranvier node. *An Acad Brasil Ciens*, 30(1):57–61, 1958.

[48] M. Tarek. Membrane electroporation: a molecular dynamics simulation. *Biophysical journal*, 88(6):4045–4053, 2005.

[49] S. Toepfl, V. Heinz, and D. Knorr. High intensity pulsed electric fields applied for food preservation. *Chemical engineering and processing: Process intensification*, 46(6):537–546, 2007.

[50] M. Vassalle. Contribution of the na+/k+-pump to the membrane potential. *Experientia*, 43(11-12):1135–1140, 1987.

[51] D. Voyer, S. Corridore, A. Collin, R. Scorretti, and C. Poignard. Numerical modeling of floating potentials in electrokinetic problems using an asymptotic method. *IEEE Transactions on Magnetics*, 56(4):1–4, 2020.

[52] Y. Zheng, E. Shojaei-Baghini, C. Wang, and Y. Sun. Microfluidic characterization of specific membrane capacitance and cytoplasm conductivity of singlecells. *Biosensors and Bioelectronics*, 42:496–502, 2013.